



universität
wien

DIPLOMARBEIT

Titel der Diplomarbeit

Exploring AMS for the measurement of the (n,γ)
cross-section on ^{209}Bi at energies relevant for nuclear
astrophysics and nuclear technology

angestrebter akademischer Grad

Magister der Naturwissenschaften (Mag. rer. nat.)

Verfasser:	Peter Kueß
Matrikel-Nummer:	0304978
Studienrichtung:	411 Physik
Betreuer:	Ao. Univ.-Prof. Dipl.-Ing. Dr. Robin Golser

Wien, am 10. Juni 2009

Abstract

Accurate neutron-capture cross-sections of ^{209}Bi became of importance since new nuclear technologies have triggered interests on the use of bismuth: as a coolant for fast neutron reactors and as spallation target in accelerator driven systems (ADS). In nuclear astrophysics, neutron capture of ^{209}Bi terminates nucleosynthesis of heavier elements in the s-process. The reaction product ^{210}Bi may exist in its ground state ($^{210\text{g}}\text{Bi}$, $t_{1/2} = 5.013$ days), and as long-lived isomer $^{210\text{m}}\text{Bi}$ ($t_{1/2} = 3 \cdot 10^6$ years). The reaction $^{209}\text{Bi}(n, \gamma)^{210(\text{g+m})}\text{Bi}$ is studied with accelerator mass spectrometry (AMS) at VERA (Vienna Environmental Research Accelerator) for thermal neutron energies (0.025 eV) and for the resonance region (keV). To explore the detection limit at VERA for measurements of the long-lived $^{210\text{m}}\text{Bi}$, a series of bismuth samples was irradiated with thermal neutrons from the TRIGA reactor of the Atominstitut in Vienna. The aim of this thesis is to use AMS, for the first time, to study the neutron-capture of ^{209}Bi in the keV neutron-energy-range. The challenge of measuring ^{210}Bi with AMS is the interfering background, produced by $^{209}\text{BiH}^-$ injection, and the isobar ^{210}Po , the decay product of $^{210\text{g}}\text{Bi}$.

Zusammenfassung

Für neue Nukleartechniken existiert ein gesteigertes Interesse an Wismut: Als Spallationstarget in Accelerator Driven Systems (ADS), als auch als Kühlmittel in "Schnellen Neutronenreaktoren". In der nuklearen Astrophysik beendet der Neutroneneinfang von ^{209}Bi die Nukleosynthese von schwereren Elementen im sogenannten s-Prozess. Unter diesen Aspekten wächst der Bedarf nach einem genau bekannten Wert des Wirkungsquerschnittes für den Neutroneneinfang von ^{209}Bi . Das Reaktionsprodukt ^{210}Bi kommt sowohl im Grundzustand ($^{210\text{g}}\text{Bi}$, $t_{1/2} = 5.013$ Tage), als auch als langlebiges Isomer $^{210\text{m}}\text{Bi}$ ($t_{1/2} = 3 \cdot 10^6$ Jahre) vor. An VERA (Vienna Environmental Research Accelerator) ist die Reaktion $^{209}\text{Bi}(n, \gamma)^{210(\text{g+m})}\text{Bi}$ sowohl im thermischen Bereich (0.025 eV), als auch im Resonanzbereich (keV) analysiert worden. Um die Nachweisgrenze für $^{210\text{m}}\text{Bi}$ Messungen an VERA zu bestimmen, wurden eine Reihe von Wismutproben am TRIGA Reaktor am Atominstitut in Wien mit thermischen Neutronen bestrahlt. Ziel dieser Diplomarbeit ist es, erstmalig den Neutroneneinfang von ^{209}Bi im Resonanzbereich, mit AMS, zu untersuchen. Die Herausforderung von ^{210}Bi Messungen mittels AMS ist die Unterdrückung des Hintergrundes, der sowohl durch $^{209}\text{BiH}^-$ als auch durch ^{210}Po entsteht.

Contents

1	Introduction	1
1.1	Existing data	2
2	Nuclear astrophysics and the production of ^{210}Bi	7
2.1	Stellar nucleosynthesis	8
2.1.1	Hydrogen burning	9
2.1.2	Helium burning	10
2.1.3	Advanced burning processes	10
2.1.4	s-process	11
	The recycling of the s-process	12
3	Nuclear technologies	15
3.1	Fast Neutron Reactors (FNR's)	16
3.2	Accelerator-Driven Systems (ADS)	17
3.2.1	Components of ADS	18
3.2.2	ADS tests	20
	MEGAPIE	20
	MYRRHA	21
4	Determination of the neutron capture cross-section of $^{209}\text{Bi}(n,\gamma)^{210(g+m)}\text{Bi}$	23
4.1	Cross-section measurement of $^{209}\text{Bi}(n,\gamma)^{210g}\text{Bi}$	24
4.2	Cross-section measurement of $^{209}\text{Bi}(n,\gamma)^{210m}\text{Bi}$	24

5	Neutron Irradiations	27
5.1	Irradiation at the Atominstitut in Vienna with thermal neutrons	27
5.1.1	Determination of the neutron fluence	30
	Example: fluence determination - Bi19	36
5.2	Neutron irradiation at Forschungszentrum Karlsruhe with "25 keV" neutrons . . .	37
6	Accelerator Mass Spectrometry (AMS)	39
6.1	The principle of AMS	39
6.2	VERA - an overview	39
6.2.1	Ion source	42
6.2.2	Magnetic deflection systems	42
	The MBS system at VERA	42
6.2.3	Electrostatic deflection systems	43
6.2.4	The tandem accelerator	43
6.2.5	Wien Filter	44
6.2.6	The heavy ion detector	44
6.2.7	Beam analysing elements	44
7	Measuring $^{210\text{m}}\text{Bi}$ at VERA	45
7.1	Tuning procedure	46
7.2	Evaluation of a TOF-energy spectrum	49
7.3	Bismuth blanks	49
7.4	Efficiency determination	53
7.4.1	Negative ion formation probability	53
7.4.2	"High-energy-transmission"	54
7.5	Polonium separation	55
7.5.1	Polonium correction	55
7.5.2	Chemical pretreatment	56
7.6	Reference samples	56
8	Results	59
8.1	Cross-section of $^{209}\text{Bi}(n,\gamma)^{210\text{g}}\text{Bi}$ at thermal energies	59

8.2	Efficiency	59
8.2.1	Negative ion formation probability	59
8.2.2	Beam losses at the high-energy-side	62
8.2.3	Polonium scale factor	69
8.3	Blanks	72
8.3.1	Linear blank correction	72
8.3.2	Gaussian blank correction	76
8.4	Polonium-free AMS samples	79
8.5	Reference samples	82
8.6	AMS measurements for $kT=25$ keV-samples	84
9	Summary and outlook	87
	Bibliography	89
	Acknowledgements	94
	Curriculum vitae	96
	Lebenslauf	98

1 Introduction

^{209}Bi is the only quasi-stable isotope of bismuth. According to [1] ^{209}Bi is an alpha emitter with a half-life of $(1.9 \pm 0.2) \cdot 10^{19}$ years. When irradiating bismuth with neutrons, $^{209}\text{Bi}(n, \gamma)^{210}\text{Bi}$ is a possible reaction. ^{210}Bi may exist in the ground state (^{210g}Bi) and in an isomeric state (^{210m}Bi). The half-life of ^{210g}Bi is 5.013 days and the half-life of the isomer ^{210m}Bi is $3.04 \cdot 10^6$ years [2]. ^{210}Po is formed via β -decay of ^{210g}Bi . ^{210}Po itself decays by α -emission to the stable lead isotope ^{206}Pb with a half-life of 138.38 days [2]. The isomeric state ^{210m}Bi is also an alpha emitter but decays to ^{206}Tl , which further decays via beta decay to ^{206}Pb with an half-life of 4.20 minutes [3].

The decay scheme of ^{210}Bi is shown in figure 1.1.

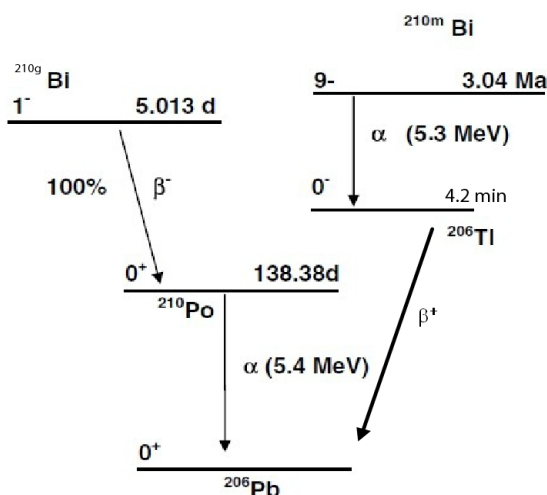


Figure 1.1: Decay scheme of ^{210}Bi [4]

In nuclear astrophysics neutron capture of ^{209}Bi terminates the s-process (see chapter 2). New nuclear technologies have triggered interests on the use of bismuth in combination with lead as a coolant for fast neutron reactors, and as spallation target in accelerator driven systems (ADS) (see chapter 3).

The neutron capture cross-section is a function of the neutron energy. A rather accurate value of the cross-section of the reaction $^{209}\text{Bi}(n, \gamma)^{210(\text{m}+\text{g})}\text{Bi}$ was identified by previous experiments for thermal energies ($kT \approx 25$ meV). However, the ratio between $^{209}\text{Bi}(n, \gamma)^{210\text{m}}\text{Bi}$ and $^{209}\text{Bi}(n, \gamma)^{210\text{g}}\text{Bi}$ varies among different experiments (see chapter 1.1).

Furthermore, there is a significant difference between evaluated values and values obtained by measurements for both cross-sections of $^{209}\text{Bi}(n, \gamma)^{210\text{m}}\text{Bi}$ and $^{209}\text{Bi}(n, \gamma)^{210\text{g}}\text{Bi}$.

The determination of the cross-section value $^{209}\text{Bi}(n, \gamma)^{210\text{m}}\text{Bi}$ with accelerator mass spectrometry (AMS) was performed just once by C. Stan-Sion et al. [4] for thermal energies. For epithermal energies no values have been published on bismuth measurements using AMS. The aim of this thesis is to explore the detection limit for bismuth measurements at the AMS facility VERA (Vienna Environmental Research Accelerator). In this study, samples, made out of metallic bismuth powder, were irradiated both with neutrons of thermal and epithermal energies.

Nine bismuth powder samples were irradiated with thermal neutrons in three run series as preliminary work of this thesis at the Atominstitut in Vienna. Two bismuth samples were also irradiated at Forschungszentrum Karlsruhe with neutrons with a quasi-Maxwellian energy distribution of $kT = 25 \pm 0.5$ keV. Moreover, some bismuth samples were measured at VERA to obtain a basic setup of the facility before the work for this thesis started.

1.1 Existing data

Figure 1.2 shows the dependence of cross-section for the reaction $^{209}\text{Bi}(n, \gamma)^{210(\text{g}+\text{m})}\text{Bi}$ on neutron energy according to ENDF/B-VII [5]. The published values for the $^{209}\text{Bi}(n, \gamma)^{210(\text{g}+\text{m})}\text{Bi}$ cross-section at thermal energies agree for different measuring methods, and also with evaluated values, as shown in table 1.1. The first experiments to measure the $^{209}\text{Bi}(n, \gamma)^{210(\text{g}+\text{m})}\text{Bi}$ cross-section were carried out in the 1950ies. The pile oscillator method was used to achieve results. In this technique, the sample is moved back and forth in a field of thermal neutrons. As the sample absorbs neutrons, the neutron flux decreases in the vicinity of the sample. This depression of neutrons causes an oscillating signal in a nearby ion chamber. The amplitude of this signal is proportional to the neutron absorption cross-section. For more information about the pile oscillator method see [6].

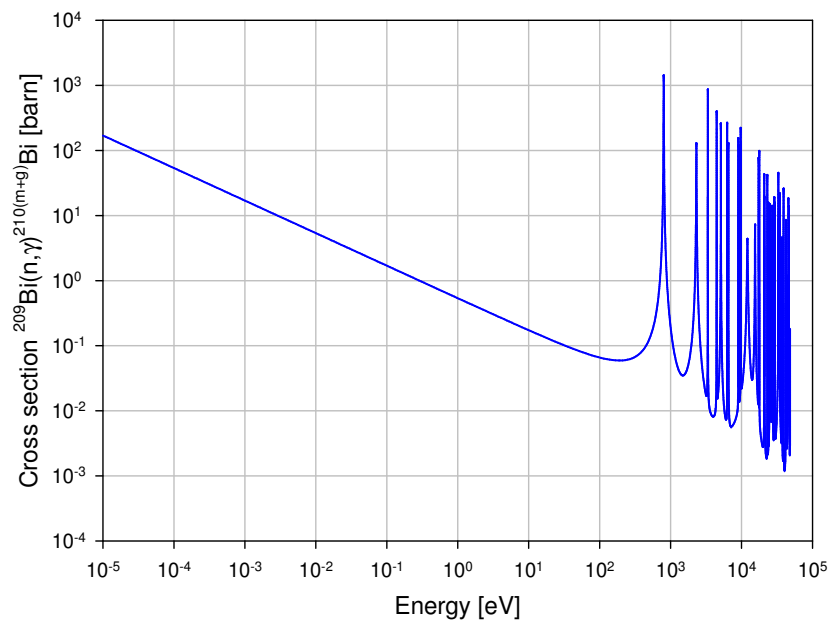


Figure 1.2: Cross-section of $^{209}\text{Bi}(n, \gamma)^{210(g+m)}\text{Bi}$ as a function of the neutron energy [5]

Later, the prompt gamma activation analysis (PGAA) was also used to determine the $^{209}\text{Bi}(n, \gamma)^{210(g+m)}\text{Bi}$ cross-section at thermal energies. PGAA is denoted as prompt γ in the following tables. In this technique, the sample is irradiated with a neutron beam of constant energy. This can result in a neutron capture by the sample. Due to the binding energy caused by the captured neutron, the compound nucleus forms an excited state. Via emitting so-called prompt γ -rays the compound nucleus decays to a more stable state. These γ -rays are measured with a high resolution γ -ray spectrometer, an instrument that measures the intensity distribution of γ -rays versus the energy. The neutron capturing elements are identified via the energy of the γ -rays¹.

Measuring the $^{209}\text{Bi}(n, \gamma)^{210g}\text{Bi}$ cross-section α spectroscopy is used. The alpha particles are coming from the ^{210}Po decay to ^{206}Pb . The energy of the alpha particles is measured with a surface barrier detector.

Experimental data for the $^{209}\text{Bi}(n, \gamma)^{210m}\text{Bi}$ cross-section are sparse. Remarkable is the difference between evaluation and measurement. Due to the long half-life of ^{210m}Bi alpha

¹<http://www.ncnr.nist.gov/instruments/pgaa/>

$\sigma_{g+m}[mbarn]$	Author	Year	Measuring Method
33.8 (0.7)	ENDF/B-VII [5]	2006	Evaluation
33.8	JENDL-3.3 [7]	2002	Evaluation
38	S.P. Harris [8]	1950	Pile Oscillator
30.8 (2.2)	D.J. Littler [9]	1953	Pile Oscillator
38-39	G.W. Horsley [10]	1956	Pile Oscillator
36 (4.0)	R.B. Tattersall [11]	1960	Pile Oscillator
35 (1.8)	A. Letourneau [12]	2002	Prompt γ
34.2 (0.4)	A. Borella [13]	2005	Prompt γ

Table 1.1: Experimental and evaluated values of $^{209}\text{Bi}(n, \gamma)^{210(g+m)}\text{Bi}$ at thermal energies. The uncertainty is given in parenthesis.

spectroscopy is no feasible method to measure the $^{209}\text{Bi}(n, \gamma)^{210m}\text{Bi}$ cross-section. One experiment was carried out using prompt gammas [13] and another using accelerator mass spectrometry (AMS) [4].

$\sigma_g[mbarn]$	Author	Year	Measuring Method
24.2	ENDF/B-VII [5]	2006	Evaluation
30	JENDL-3.3 [7]	2002	Evaluation
15.0 (3.0)	L. Seren [14]	1947	direct β counting
20.5 (1.5)	F.C.W. Colmer [15]	1950	direct β counting
24.2 (0.4)	M. Takiue and H. Isikawa [16]	1978	activation with LSC
16.1 (1.8)	A. Letourneau [17]	2006	α spectroscopy
18.4 (0.9)	A. Letourneau [17]	2006	γ spectroscopy
19.3 (0.8)	A. Borella [13]	2005	prompt γ

Table 1.2: Experimental and evaluated values of $^{209}\text{Bi}(n, \gamma)^{210g}\text{Bi}$ at thermal energies. The uncertainty is given in parenthesis.

$\sigma_m[mbarn]$	Author	Year	Measuring Method
9.6	ENDF/B-VII [5]	2006	Evaluation
3.8	JENDL-3.3 [7]	2002	Evaluation
17.7 (0.7)	A. Borella [13]	2005	prompt γ
21.3 (0.9)	C. Stan-Sion [4]	2007	AMS

Table 1.3: Experimental and evaluated values of $^{209}\text{Bi}(n, \gamma)^{210m}\text{Bi}$ at thermal energies. The uncertainty is given in parenthesis.

For measuring the $^{209}\text{Bi}(n, \gamma)^{210}\text{Bi}$ cross-section at epithermal energies neutron time-of-flight methods were mostly used. In these methods neutrons of all energies, up to the energy of the

proton beam², were produced via a pulsed proton beam bombarding a spallation target. The neutron time-of-flight between spallation target and sample is measured and thus the neutron energy can be determined. The start signal is determined by the pulsed proton beam, which is synchronised with the data acquisition. The stop signal is caused by prompt γ -rays due to a possible neutron capture. Knowing the neutron fluence and the neutron energy distribution, the neutron capture cross-section can be determined for energies up to the energy of the proton beam.

n_TOF is a neutron time of flight facility in CERN. Other neutron time of flight facilities are denoted as "Time-of-Flight" in the following tables.

The energy given in table 1.4, 1.5 and 1.6 is the Maxwellian energy distribution of the neutrons.

²The n_TOF facility utilise a 20 GeV proton beam.
webpage: <http://cdsweb.cern.ch/record/554721/files/sl-2002-011.pdf>

σ_{g+m} [mbarn]	Author	Year	Measuring Method
2.4	ENDF/B-VII [5]	2006	Evaluation
2.58 (0.41)	C. Domingo-Pardo [18]	2006	n_Tof (Cern) 30 keV
2.54 (0.48)	P. Mutti [19]	1998	30 keV
3.12 (0.6)	H. Beer [20]	1992	30 keV
2.7 (0.13)	K. Saito [21]	2003	Time of Flight 30 keV
2.89 (0.5)	C. Domingo-Pardo [18]	2006	n_Tof (Cern) 25 keV

Table 1.4: Experimental and evaluated values of $^{209}\text{Bi}(n, \gamma)^{210g+m}\text{Bi}$ in the resonance region. The uncertainty is given in parenthesis.

σ_g [mbarn]	Author	Year	Measuring Method
2.16 (0.07)	S. Bisterzo [22]	2007	prompt γ 30 keV
2.23 (0.07)	S. Bisterzo [22]	2007	25 keV
2.45 (0.1)	U. Ratzel [23]	2004	Activation 30 keV

Table 1.5: Experimental values of $^{209}\text{Bi}(n, \gamma)^{210g}\text{Bi}$ in the resonance region. The uncertainty is given in parenthesis.

σ_m [mbarn]	Author	Year	Measuring Method
0.65 (0.40)	K. Saito [21]	2002	Time of Fight 30 keV
0.76 (0.09)	K. Saito [21]	2002	Time of Fight 534 keV

Table 1.6: Experimental values of $^{209}\text{Bi}(n, \gamma)^{210m}\text{Bi}$ in the resonance region - uncertainty is given in parenthesis.

2 Nuclear astrophysics and the production of



Nucleosynthesis describes the origin of the elements in the universe. It consists of two parts: the primordial and stellar nucleosynthesis. The first compilation about this subject is a paper called B²FH by E.M. Burbidge, G.R. Burbidge, W.A. Fowler and F. Hoyle in 1957 [24]. The aim of the authors was to explain why elements occur with their specific abundance in the universe. Forty years later a review was published by Wallerstein et al. and it summarises the progress in this field between 1957 and 1997 [25].

There exist several methods to find out the elemental abundance distribution. One method is to take samples from the Earth's crust or from meteoroids. Another method is using spectral analysis of stars.

Each method has advantages and disadvantages. Samples from the Earth's crust for example contain much more oxygen and silicon than hydrogen and helium¹. Geological and chemical processes in the earth change the abundance. On the other hand the distribution of the isotopes can be measured very precisely with samples taken from the Earth's crust.

Combining the measurement results of each method leads to a solar abundance distribution of elements which is shown in figure 2.1. In this figure the abundance is plotted against the atomic number (Z) and normalised to the abundance of silicon with 10⁶ atoms. It is apparent that hydrogen and helium are the most common elements with 71.1% and 27.4% mass fraction, respectively.

Further it can be seen that the abundance decreases with increasing atomic number. Beside the peaks of hydrogen and helium there are also maxima for carbon (Z=6), oxygen (Z=8) and

¹The reason for this lack of hydrogen and helium is the loss of the primordial atmosphere with predominantly consisted of hydrogen and helium.

iron ($Z=26$). On the other side remarkable minima can be found for lithium ($Z=3$), beryllium ($Z=4$) and boron ($Z=5$). The abundance distribution spans a range of twelve orders of magnitude and suggests that there are several different processes necessary to explain this distribution pattern. These processes will be explained in the following sections.

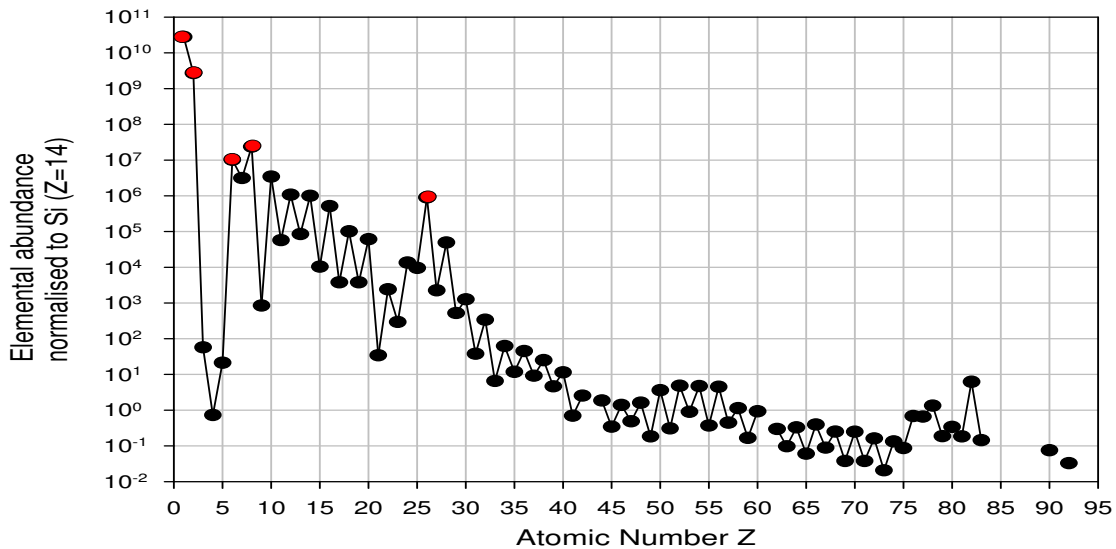


Figure 2.1: Solar elemental abundance distribution normalised to Si ($Z=14$): remarkable maxima are plotted in red. Data taken from [Anders and Grevesse,[26]]

2.1 Stellar nucleosynthesis

During the Big Bang protons and neutrons formed the first elements: ^2H , ^3H , ^3He , ^4He and ^7Li . This is called primordial nucleosynthesis. This process stopped already three minutes after the Big Bang when the temperature and density in the universe were too low for further nuclear fusion.

When stars were created (about 10^9 years after the big bang) the stellar nucleosynthesis could take place. Several nuclear fusion processes are responsible for producing elements from helium up to iron, starting with hydrogen burning followed by helium burning up to silicon burning. Depending on the mass of the star, different nuclear fusion processes take place. Elements heavier than iron are generated mainly by neutron-capture processes, either by the slow-neutron-capture-process (s-process) or the rapid-neutron-capture-process (r-process). In

addition a small amount of nuclei, heavier than iron, is produced by the proton capture process (p-process). The purpose of this thesis is related to the termination of the s-process. Therefore in this chapter mostly the s-process is summarised. For further information on r- and p-process see for example [25], [27] and [28].

2.1.1 Hydrogen burning

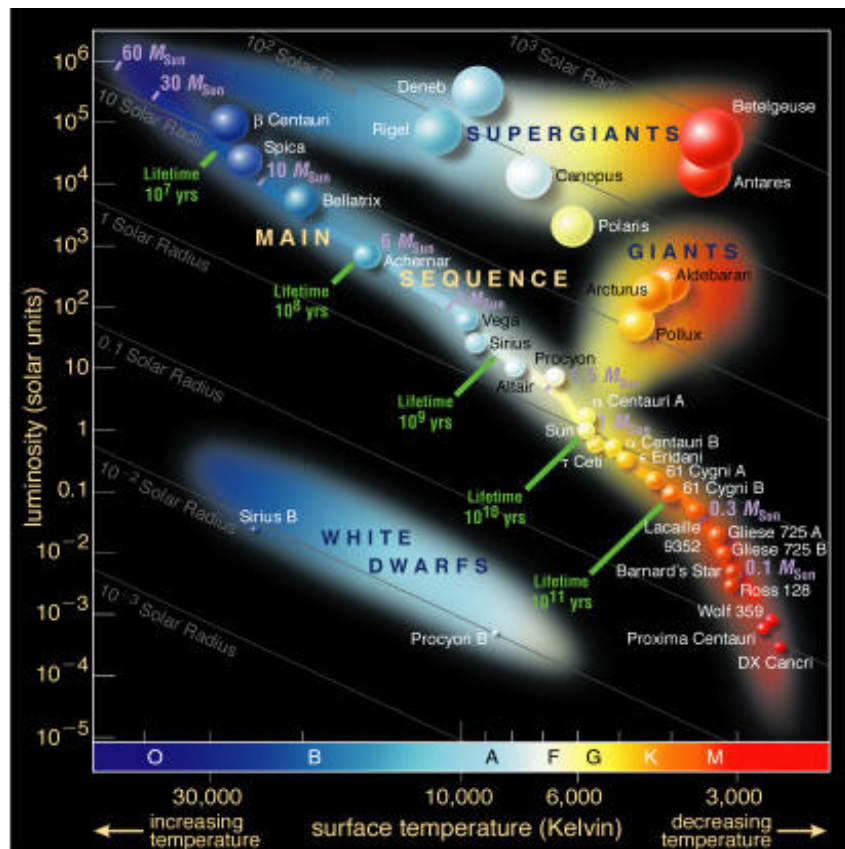


Figure 2.2: An example for a Hertzsprung-Russel diagram

Due to gravitational contracting the increasing temperature and density in a star initiates hydrogen burning after a short period. It is the longest and main phase in a star's life. In the Hertzsprung-Russel diagram such stars occupy the region along a line called main sequence. A Hertzsprung-Russel diagram (H-R diagram), see figure 2.2², shows the relationship between luminosity and effective surface temperature of stars. Depending on the temperature in the center of a star, two burning scenarios exist to convert hydrogen into helium: the so-called

²<http://www.daviddarling.info/encyclopedia/H/HRdiag.html>

proton-proton chain (p-p chain) on one hand, and the CNO cycle, which needs a catalyst (^{12}C) to operate, on the other. For low temperatures the p-p chain is the dominating process while the CNO cycle dominates for higher temperatures.

2.1.2 Helium burning

After hydrogen has been burned to helium in the center of a star, the centre contracts and consequently temperature and density are further increased. To compensate the rising temperature the shell of the star expands which causes cooling of the surface temperature. A star in this stage of its life is therefore called a red giant. In the surrounding of the helium core hydrogen burning continues. Under these conditions helium burning starts as well, presuming that the mass of the star is at least 0.5 times the mass of the sun. The most important feature of helium burning is the production of ^{12}C by the triple alpha process. As all nuclei with a mass number of 5 and 8 have very short half-life³, the production of ^{12}C needs not only two but three α particles that join the reaction. More precisely the reaction proceeds in two steps. First two α particles fuse to ^8Be . The half-life of ^8Be is only 10^{-16} s. However, this reaction shows a distinct resonance at energies typical for helium burning and, therefore, a high cross-section for an additional α capture. It is therefore possible that ^8Be adds another α particle to produce ^{12}C prior its decay.

2.1.3 Advanced burning processes

In stars more than eight times heavier than our sun, fusion reactions continue. Helium burning is followed by carbon burning, neon burning, oxygen burning and silicon burning. After the fuel of a nuclear burning phase is consumed, the thermal pressure decreases and the star contracts, causing a temperature increase in the centre. Due to the higher Coulomb barrier, higher temperatures are needed in the centre to initiate the next burning phase. In the outer layers of the star the previous burning phases continue in a shell which can be seen in figure 2.3. These processes lead to the formation of the elements between $Z=20$ and $Z=50$. Beyond iron there is no possibility to gain energy by fusion because the binding energy per nucleon is at its maximum in this region. Therefore, nucleosynthesis needs other processes to create

³For all nuclei with $A=5$ the half-life is about 10^{-24} s. The half-lives for the nuclei with $A=8$ are below 1 s.

elements heavier than iron.

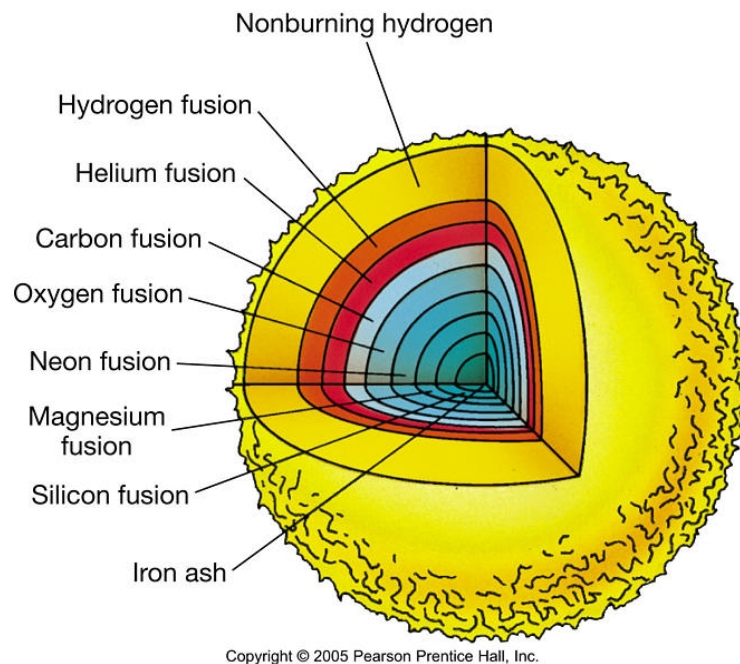


Figure 2.3: Schematic view of the burning stages of a well evolved massive star, assumed to be at least 10 solar masses, showing its burning layers in the usual onion skin form, just before it undergoes its final stage of core collapse.
<http://physics.uoregon.edu>

2.1.4 s-process

Neutron capture processes are the main reactions to produce elements heavier than iron, because neutrons do not have to conquer the Coulomb barrier. Often a (n, γ) reaction is followed by a beta decay.

A neutron-capture process is called slow (s-process) when the beta decay has time to take place before another neutron is captured. So the s-process tracks a path through the chart of nuclides along the valley of stability up to ^{209}Bi (see figure 2.4). In contrast, during the r-process (rapid neutron-capture process) a series of subsequent neutron captures occur before the beta-decay happens. The path of the r-process leads far beyond the valley of stability to the neutron-rich side of the chart of nuclides and so elements heavier than bismuth can be produced. The difference between the s- and r-process is the neutron density. While the neutron density during the s-process is about 10^8 n cm^{-3} , it is $10^{21} \text{ n cm}^{-3}$ during the r-process.

The s-process is thought to happen during helium burning. Therefore it occurs off the main sequence of the Hertzsprung-Russel diagram in the so called AGB stars ⁴. In the final stage of their lives AGB stars abandon their outer shell and enrich the interstellar medium with heavy elements. The s-process is divided into three components depending on the neutron density, the temperature and the mass of the star: the weak, the main and the strong component.

The weak component dominates element production from iron up to zirconium and needs stars heavier than eight solar masses. The neutron density is only about 10^6 n cm^{-3} at temperatures of about $3 \cdot 10^8 \text{ K}$ (=25.8 keV). The neutron source of this component is the reaction $^{22}\text{Ne}(\alpha, n)^{25}\text{Mg}$. This reaction takes place during the helium burning phase assuming that preexisting ^{14}N is rapidly converted into ^{22}Ne by a number of α particle captures.

The main component is responsible for the production of the elements between $A=90$ and $A=204$ and occurs in stars with a mass up to three solar masses. The neutron density is about 10^7 n cm^{-3} and the temperature needed is $0.9 \cdot 10^8 \text{ K}$ (=7.7 keV). The neutron sources are in 5% the reaction $^{22}\text{Ne}(\alpha, n)^{25}\text{Mg}$ and in 95% the reaction $^{13}\text{C}(\alpha, n)^{16}\text{O}$. The latter also occurs during helium burning.

The third part of the s-process is the strong component. It was postulated to explain the abundance maxima at ^{208}Pb and ^{209}Bi .

For more information about the s-process see [27] and [28].

The recycling of the s-process

At the very end of the s-process path a recycling process takes place, as illustrated in figure 2.4. Starting from ^{206}Pb , the neutron capture process continues to produce lead isotopes up to $A=209$. ^{209}Bi is formed via beta decay from ^{209}Pb with a half-life of 3.25 hours. As mentioned in chapter 1, ^{209}Bi is a quasi-stable isotope with a half-life of $(1.9 \pm 0.2) \cdot 10^{19} \text{ y}$. ^{210g}Bi and ^{210m}Bi are produced by a neutron capture of ^{209}Bi . The ground state decays via beta decay to ^{210}Po with a half-life of 5.013. ^{210}Po itself decays via alpha particle emission to stable ^{206}Pb , where the recycling loop starts again.

If a ^{210m}Bi nuclide is produced it may either decay via alpha particle emission to ^{206}Tl , which decays within minutes to ^{206}Pb via beta decay, or ^{211}Bi is produced via neutron capture. ^{211}Bi itself is an alpha-emitter, producing ^{207}Th . ^{207}Tl itself produces ^{207}Pb via beta decay with a

⁴AGB = asymptotic giant branch

half-life of 4.77 minutes. This closes the cycle again.

The bottleneck of this cycle is the double magic lead isotope ^{208}Pb , which has the smallest neutron capture cross-section and thus ^{208}Pb is accumulated.

A goal of this thesis is to identify the production ratio between $^{210\text{m}}\text{Bi}$ and $^{210\text{g}}\text{Bi}$ via neutron capture at energies typically for stellar nucleosynthesis and the ratio of the particular recycling loops.

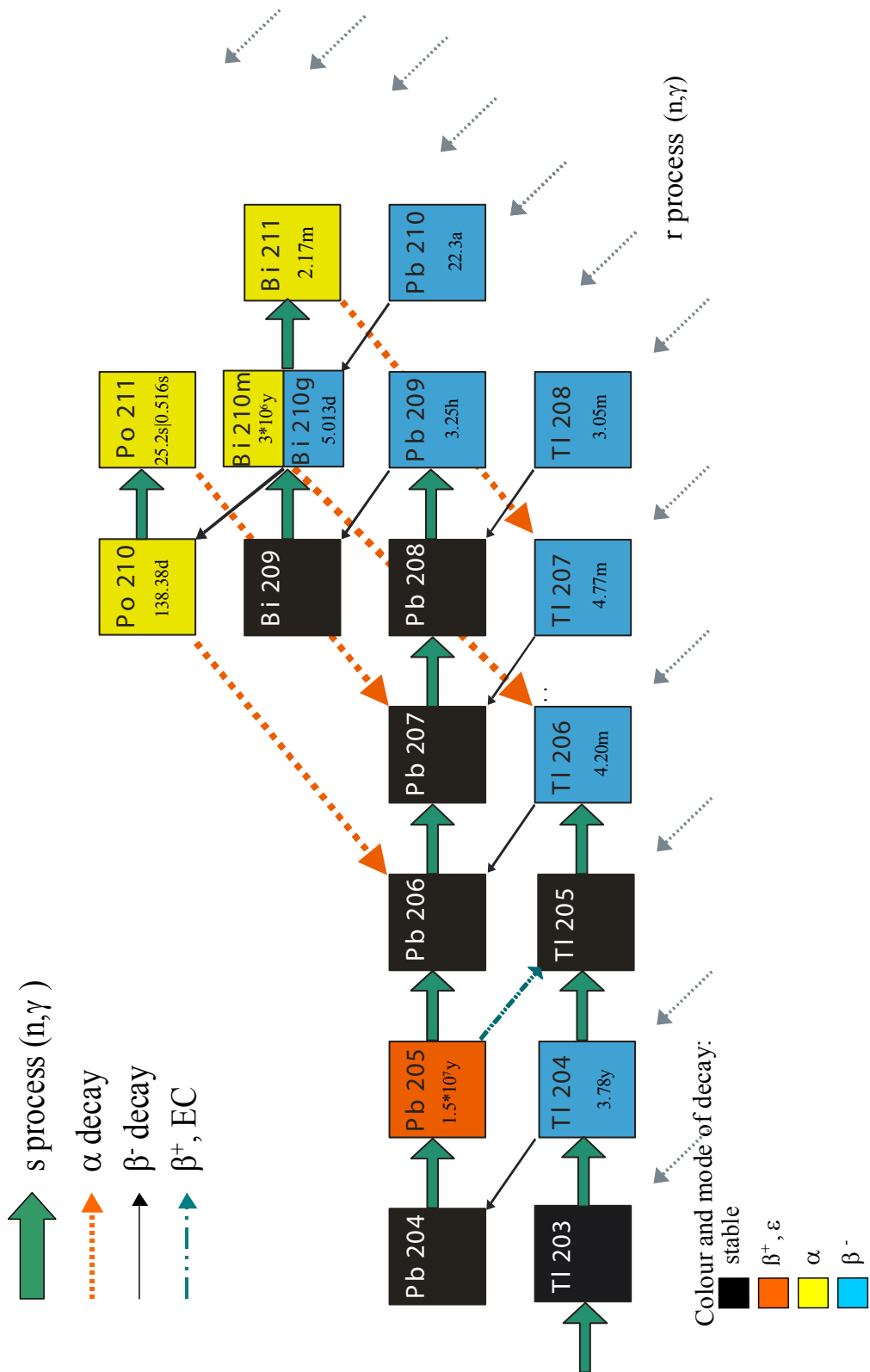


Figure 2.4: The end of the s-process and the recycling loop

3 Nuclear technologies

Bismuth and lead are candidates for spallation targets in ADS (Accelerator-Driven-Systems) and as coolants in fast reactors. The heavy elements are used in their liquid form in order to avoid structural damage. The advantages of lead and bismuth for an ADS facility are their high neutron yield per proton¹, their small scattering cross-section [30] and their small neutron capture cross-section. The cross-section of the $^{209}\text{Bi}(n, \gamma)^{210}\text{Bi}$ reaction will be explained later in this thesis. The advantages of the materials increase when using a lead-bismuth-eutectic (LBE)².

As a coolant LBE (similarly to lead) has the following properties: high heat capacity, inert behaviour with respect to reaction with water, high boiling temperature and low melting temperature. The temperatures in a fast reactor are around 500 °C and the pressure is near atmospheric pressure. In table 3.1 some basic characteristics of reactor coolants are listed. The table shows that LBE would be the best choice for a coolant. But because bismuth is rare and more expensive than lead, research for lead-only-coolants also exists.

Due to the high neutron flux in an ADS facility and in fast reactors the neutron capture cross-sections of $^{209}\text{Bi}(n, \gamma)^{210g}\text{Bi}$ and $^{209}\text{Bi}(n, \gamma)^{210m}\text{Bi}$ are of interest. The knowledge of these cross-sections is very limited, therefore research on this topic is needed.

Coolant	Atomic mass [amu]	Melting Point [°C]	Boiling Point [°C]	Chemical reactivity (with air and water)
Pb	207	327	1737	Inert
LBE	208	125	1670	Inert
Na	23	95	883	Highly reactive

Table 3.1: Basic characteristics of reactor coolants, showing that LBE has the highest temperature region in the liquid state. [31]

¹A proton with E=1GeV produces about 28 neutrons [29]

²An eutectic is a mixture at such proportions that the melting point is as low as possible. Furthermore all components undergo the phase change from liquid to solid simultaneously, which is known as eutectic reaction.

3.1 Fast Neutron Reactors (FNR's)

In 2003 the Generation IV International Forum (GIF) announced the selection of six reactor technologies believed to be important for the future of nuclear energy. The selection was based on safety, cost-efficiency, environment-friendliness and the impossibility to convert the fuel material into nuclear weapons (proliferation). Two systems are based on slow neutron reaction while the other concepts are based on the fast reactor principle. The Pb/LBE coolant concept was also chosen as one of these six concepts [29].

The FNR concept is not new, but earlier FNR's were only used to breed the fissile material ^{235}U . Therefore these facilities were called fast breeder reactors (FBR). Nowadays this technology is thought to help eliminating the unwanted surplus of plutonium which can be used as fuel instead of ^{235}U .

As the name implies, fast reactors do not use a moderator to slow down the neutrons to thermal energies ($E \approx 0.025$ eV). The energy of the neutrons remains high (keV to MeV region). The fission cross-section decreases with increasing neutron energy. Therefore plutonium or highly-enriched uranium (typically 20% ^{235}U) must be used as fuel to sustain the chain-reaction in a fast reactor while in a reactor concept that uses a moderator the part of ^{235}U is about 3%. The thermal fission cross-section of neutrons (σ_f) with $E=0.025$ eV, of some uranium and plutonium isotopes are listed in table 3.2.

Isotope	σ_f [barn]
^{235}U	586
^{238}U	$3 \cdot 10^{-6}$
^{239}Pu	752
^{240}Pu	0.059
^{241}Pu	1010

Table 3.2: Fission cross-sections ($E_{neutron}=0.025$ eV) of possible fuel material in fast reactors

3.2 Accelerator-Driven Systems (ADS)

Accelerator-Driven Systems (ADS), Accelerator-Driven Transmutation of Waste (ATW) or just Hybrid Reactors are all describing the same nuclear system: A powerful particle accelerator combined with a subcritical reactor. In this subcritical reactor the chain-reaction is only sustained if neutrons are produced at the spallation target. This is only happening when the particle accelerator is in operation.

The search for a repository to store the huge amount of nuclear waste is the greatest challenge of nuclear technology. In Europe 35% of all electricity is produced by nuclear power plants [32]. These plants produce about 2500 tons burned-out fuel per year. This amount includes 25 tons plutonium, 3.5 tons of the minor actinides (Np, Am, Cm) and 3 tons long-lived fission products (LLFP) [32].

Table 3.3 shows the half-life of some isotopes evolving from the reactor handling.

Isotope	Half-life [y]
⁹⁰ Sr	28.8
⁹⁹ Tc	$2.11 \cdot 10^5$
¹²⁹ I	$1.57 \cdot 10^7$
¹³⁷ Cs	30.1
²³⁹ Pu	$2.41 \cdot 10^4$
²⁴¹ Am	432.2
²⁴² Pu	$3.73 \cdot 10^5$
²³⁷ Np	$2.14 \cdot 10^6$

Table 3.3: Half-lives of some isotopes occurring during reactor handling

The basic goal of ADS is therefore to reduce radioactive waste through transmutation. Transmutation can be induced by any particle (charged or uncharged) or quantum. A charged particle, however, must pass through the Coulomb barrier which needs energy. γ -quanta have small cross-sections for reactions (e.g. (γ, n)) and neither is there a monoenergetic γ -source. Therefore these reactions are not of interest for the transmutation of nuclear waste. It follows that neutrons are the best choice for transmutation reactions in ADS facilities. Because of this, it is especially important to know the neutron capture cross-sections of the utilised materials.

ADS should be able to transmute minor actinides and long-lived fission products which occur during the reactor handling. Both, short- and long-lived fission products are part of

nuclear waste. Short-lived isotopes like ^{90}Sr and ^{137}Cs cannot be transmuted effectively. But with a half-life of 28.6 and 30.2 years, respectively, a geological storage is possible. This is no suitable solution for the long-lived isotopes like ^{239}Pu , ^{242}Pu , ^{237}Np and other transuranic elements, and also not for ^{99}Tc and ^{129}I (see table 3.3 for the half-lives of these isotopes).

Every transuranic element (Np, Pu, Am, Cm) can be fissioned by one or a small number of successive neutron absorptions and transmuted to short-lived or even stable isotopes [30].

^{99}Tc and ^{129}I can be transmuted through neutron absorption to stable ruthenium and xenon isotopes, respectively.

The heat generated by the transmutation can, in principle, be used to produce electrical energy. Only 4-15% of the generated heat is needed to operate the accelerator [30].

However, transmutation of fission products needs plenty of neutrons. This surplus of neutrons required in an ADS facility can be produced via a proton beam, bombarding a spallation target. This spallation target consists of, for example bismuth, lead or an alloy of both.

3.2.1 Components of ADS

ADS consists of three main components: a proton accelerator, a spallation target and a subcritical reactor (also called Spallator or Blanket).

Both, linear and cyclotron accelerators have been proposed for ADS. For a proper handling, the accelerator has to produce protons with an energy of about 1-1.5 GeV. As shown in figure 3.1, there is no significant gain for higher energies. Figure 3.1 shows the neutron yield per proton versus the proton energy on a logarithmic scale. For reasons of costs, accelerators with proton energies below 1 GeV may also be of interest for the first test systems like the MYRRHA facility in Belgium, which works with a 350 MeV proton beam [33].

Not only neutrons are generated at the spallation target. The spallation products cover all elements up to the target nuclei. Due to the Coulomb interaction the generated charged particles are slowed down or stopped in the target and its vicinity. In contrast neutrons penetrate the target and the surrounding core. Those neutrons generated at the spallation target are called external neutrons. Generally, a proton beam generates more neutrons at heavy targets because elements with a high atomic number are neutron rich. Therefore elements like lead and bismuth are preferred materials for spallation targets. For most cases liquid lead-bismuth eutectic has been proposed [35] [30]. The same liquid material can be

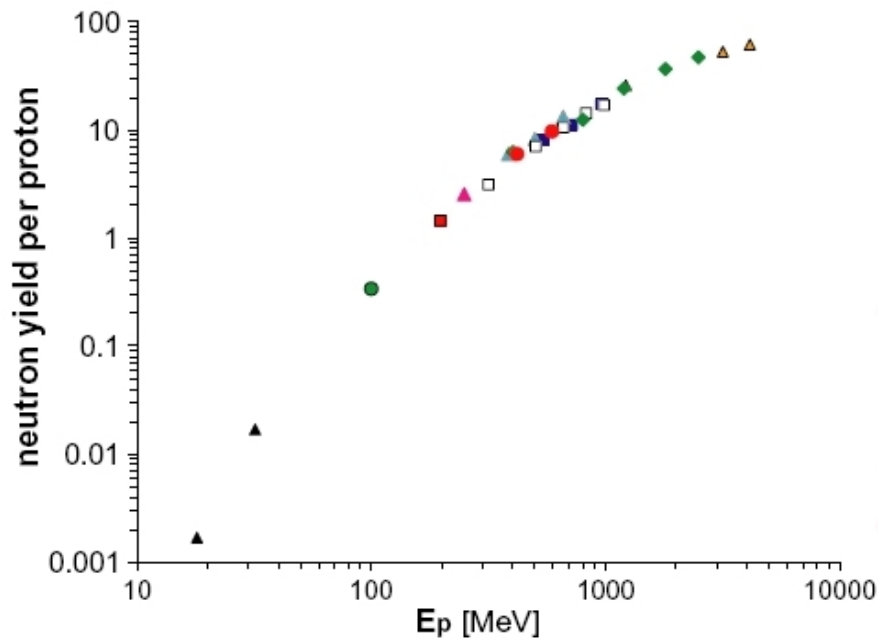


Figure 3.1: Compilation of neutron yield per proton for p+Pb and Pb/Bi measured at different energies and plotted in logarithmic scale. Different colours are different experiments, for more details see [34].

used as coolant material in the primary cooling loop. In this way the spallation target can be integrated into the core cooling system, which simplifies the construction.

If the spallation target is placed in the centre of the blanket, the blanket can act as a neutron multiplier, though it would not be self-sustaining. The neutrons obtained in the blanket are called internal neutrons. These neutrons cause fission in the fuel [30].

In a critical reactor system the self-sustaining chain reaction is caused by delayed neutrons. In an ADS facility they are replaced by external neutrons. Because spallation is an endothermal process, the protons are required to drive the process. No more external neutrons are produced in case of shutting down the proton beam. Since the reactor core is subcritical (the neutron multiplication factor k is below one) no self-sustained chain reaction can be established and fission of the actinides stops.

Transmutation efficiency and system performance depend on the choice of coolants and fuel types. The energy of the neutrons released from the target ranges from thermal energy up to the energy of the proton beam (GeV region). This is shown in figure 3.2 for a 1 GeV proton

beam.

Since the neutron flux is significantly higher in a fast neutron system, as well as the ratio between fission cross-section to neutron capture cross-section, a fast neutron system is the preferred choice to transmute actinides, even though the cross-section for neutron capture is higher for thermal neutrons. For more information about the ADS concept see for example [30].

Some neutron capture cross-section values of materials used in ADS facilities were hardly measured and the experimental results vary. An example is the cross-section for the $^{209}\text{Bi}(n, \gamma)^{210\text{g}}\text{Bi}$ and for the $^{209}\text{Bi}(n, \gamma)^{210\text{m}}\text{Bi}$ reaction. Therefore research programs in this topic have to be intensified.

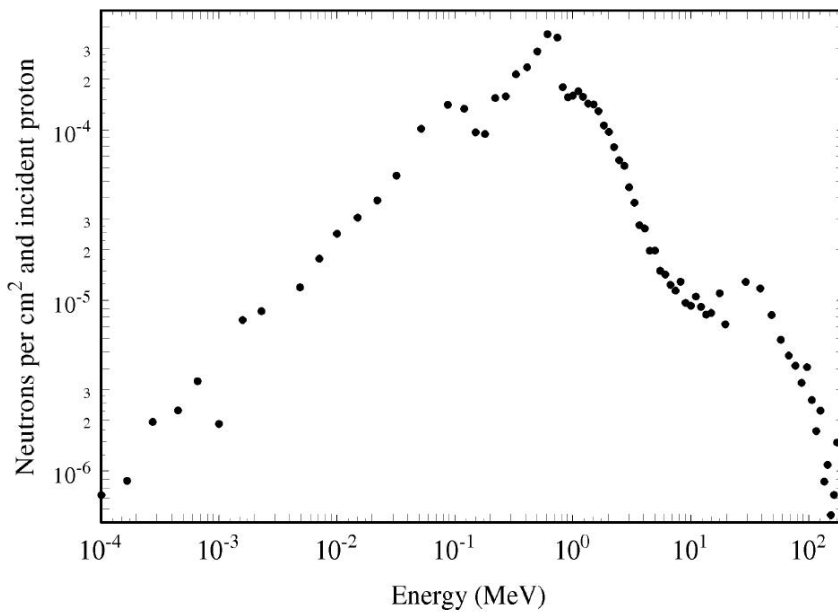


Figure 3.2: Energy spectrum of spallation neutrons produced by a 1 GeV proton beam impinging on a LBE target [30]

3.2.2 ADS tests

MEGAPIE

The MEGAPIE (Megawatt Pilot Experiment) is a feasibility study for liquid LBE spallation targets in possible future ADS facilities. 920 kg of liquid lead and bismuth were used for the spallation target which was planned and built in an international collaboration between Italy, France,

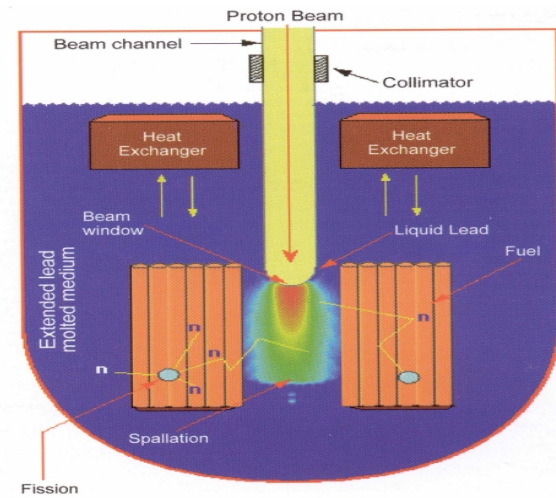


Figure 3.3: Schematic view of an ADS [29]

Latvia and Switzerland. The material was irradiated with neutrons at the SINQ (spallation neutron source) facility at the Paul Scherrer Institut (PSI) in Switzerland. This facility utilises a cyclotron delivering a proton beam with an energy of 575 MeV. This proton beam produced about 10^{17} fast neutrons per second at the LBE target. The target was irradiated from 21.8.2006 to 21.12.2006 and has been stored after the test run. More information can be found on <http://megapie.web.psi.ch> and [36].

MYRRHA

The MYRRHA facility in Belgium at SCK•CEN is an ADS under construction. It consists of a proton accelerator (cyclotron, 350 MeV·5 mA) and a windowless liquid Pb-Bi spallation target which in turns couples to a Pb-Bi cooled, subcritical fast core. The neutron yield at the spallation target is close to $2 \cdot 10^{17} \text{ n s}^{-1}$, resulting in a neutron flux of about $1 \cdot 10^{15} \text{ n s}^{-1}$ at the irradiation position of the minor actinides in the core. For more information see [33].

4 Determination of the neutron capture

cross-section of $^{209}\text{Bi}(n,\gamma)^{210(g+m)}\text{Bi}$

In this work bismuth samples were studied, which were irradiated with thermal neutrons ($kT \approx 0.025$ eV) and with neutrons of energies corresponding to a quasi-Maxwellian energy distribution of $kT = 25 \pm 0.5$ keV. The number of ^{210}Bi atoms produced in a sample can be calculated from equation 4.1, where φ denotes the neutron flux [$\text{n cm}^{-2} \text{s}^{-1}$] (assumed to be constant). $\sigma(E_n)$ is the energy-dependent neutron capture cross-section and T_{irr} the irradiation duration. This is true for monoenergetic neutrons. In case of a broad neutron-energy distribution, the cross-section has to be folded with the neutron distribution. N is the number of ^{210}Bi and ^{209}Bi atoms, respectively. Equation 4.1 can be simplified to equation 4.2, if decay during the irradiation can be neglected (i.e. of ^{210g}Bi). In equation 4.2 Φ denotes the neutron fluence [n cm^{-2}]. The cross-section in equation 4.2 is meant to be the sum of the cross-sections of the reactions $^{209}\text{Bi}(n,\gamma)^{210g}\text{Bi}$ and $^{209}\text{Bi}(n,\gamma)^{210m}\text{Bi}$. Therefore, $N_{210\text{Bi}}$ represents both reaction products, the ground state and the isomeric state.

$$N_{210\text{Bi}} = N_{209\text{Bi}} \cdot \varphi \cdot \sigma(E_n) \cdot \frac{1 - e^{-\lambda_{210g\text{Bi}} \cdot T_{irr}}}{\lambda_{210g\text{Bi}}} \quad (4.1)$$

$$N_{210\text{Bi}} = N_{209\text{Bi}} \cdot \Phi \cdot \sigma(E_n) \quad (4.2)$$

The aim of this thesis is to determine the neutron-capture cross-section for both, the capture to the ground state and to the isomeric state, separately, with two different techniques.

As can be seen from equation 4.2 under those simplified conditions, the cross-section can be calculated from the number of ^{210}Bi atoms, the number of irradiated ^{209}Bi atoms and

the measured neutron fluence (see chapter 5).

4.1 Cross-section measurement of $^{209}\text{Bi}(n,\gamma)^{210\text{g}}\text{Bi}$

The $^{209}\text{Bi}(n,\gamma)^{210\text{g}}\text{Bi}$ cross-section at thermal energies was determined via activity measurement of $^{210\text{g}}\text{Bi}$. This measurement was carried out with a liquid scintillation counter (LSC) at the Institute of Inorganic Chemistry at the University of Vienna by Gabriele Wallner. LSC registers the alpha particles emitted in the decay of ^{210}Po to ^{206}Pb (see fig. 1.1). ^{210}Po itself is formed by $^{210\text{g}}\text{Bi}$ via β -decay. If all $^{210\text{g}}\text{Bi}$ nuclei have already decayed to ^{210}Po , the number of $^{210\text{g}}\text{Bi}$ atoms can be calculated from equation 4.3, if prior decay of ^{210}Po is neglected. This is a good approximation as the half-life of ^{210}Po is long (138.38 days [2]) compared to that of $^{210\text{g}}\text{Bi}$ (5.013 days [2]). In equation 4.3 A is the specific activity (Bq/g) and t_w considers the time between end of neutron irradiation and LSC measurement.

$$N_{210\text{gBi}} = \frac{A}{\lambda_{210\text{Po}}} \cdot e^{t_w \cdot \lambda_{210\text{Po}}} \quad (4.3)$$

Knowing the number of $N_{210\text{gBi}}$ the neutron capture cross-section ($\sigma(E_n)$) for $^{209}\text{Bi}(n,\gamma)^{210\text{g}}\text{Bi}$ can be calculated by rearranging equation 4.2, assuming that the neutron fluence (Φ) is known (see chapter 5). The number of ^{209}Bi nuclei ($N_{209\text{Bi}}$) is given by:

$$N_{209\text{Bi}} = \frac{N_A}{209} \cdot m \quad (4.4)$$

In equation 4.4, m is the sample mass (gram) and N_A the Avogadro constant ($=6.022 \cdot 10^{23}$ atoms mol^{-1}). A bismuth sample with a mass of 1 gram contains $2.88 \cdot 10^{21}$ atoms.

4.2 Cross-section measurement of $^{209}\text{Bi}(n,\gamma)^{210\text{m}}\text{Bi}$

The long half-life of $^{210\text{m}}\text{Bi}$ ($3.04 \cdot 10^6$ years [2]) results in a very low activity for present-day neutron irradiations. Therefore, activity measurements are not practicable to determine the $^{209}\text{Bi}(n,\gamma)^{210\text{m}}\text{Bi}$ cross-section value. Instead, AMS was applied in this work. Other methods, that were used in previous experiments are listed in chapter 1.1.

In AMS the isotopic ratio of $^{210\text{m}}\text{Bi}$ to ^{209}Bi is measured and equation 4.2 can be rearranged to

determine the neutron capture cross-section.

In chapter 5 the neutron irradiations of bismuth samples are discussed. Among other, bismuth samples were irradiated with a quasi-Maxwellian energy distribution of $kT=25\pm 0.5$ keV at Forschungszentrum Karlsruhe. The irradiation of these samples resulted in a neutron fluence of about $1 \cdot 10^{15}$ neutrons cm^{-2} . Based on this neutron fluence and previous experimental results of neutron capture cross-section measurements for $^{209}\text{Bi}(n,\gamma)^{210\text{m}}\text{Bi}$ in the resonance energy region (see fig. 1.2), rough isotopic ratio can be calculated. For this estimation a mean cross-section value for $^{209}\text{Bi}(n,\gamma)^{210\text{m}}\text{Bi}$ ($\sigma_{m,r}$) of 1 mbarn ($=10^{-27}$ cm^2) was assumed for the resonance energy region (see chapter 1.1).

$$\frac{N_{210\text{m}}\text{Bi}}{N_{209}\text{Bi}} = \Phi \cdot \sigma_{m,r} \approx 10^{15} \frac{1}{\text{cm}^2} \cdot 1 \cdot 10^{-27} \text{cm}^2 \approx 10^{-12} \quad (4.5)$$

Equation 4.5 shows that an isotopic ratio ($^{210\text{m}}\text{Bi}/^{209}\text{Bi}$) of about 10^{-12} is expected for the bismuth samples irradiated at Forschungszentrum Karlsruhe.

First measurements were performed at VERA to investigate the detection limit of this facility for $^{210\text{m}}\text{Bi}$ detection, using samples irradiated with thermal neutrons. The neutron capture cross-section for $^{209}\text{Bi}(n,\gamma)^{210\text{m}}\text{Bi}$ ($\sigma_{m,th}$) at thermal ($kT=1/40$ eV) energies is expected to be about 20 times higher (20 mbarn) than for energies in the resonance region (e.g. for 25 keV). Bismuth samples were exposed to a neutron flux of about $4 \cdot 10^{11}$ n cm^{-2} s^{-1} (thermal) at the Atominstitut in Vienna. They were irradiated with different durations to achieve different $^{210\text{m}}\text{Bi}/^{209}\text{Bi}$ isotope ratios.

In equation 4.6 the isotopic ratio for bismuth samples irradiated for one hour (i.e. with a neutron fluence of $1.5 \cdot 10^{15}$ n cm^{-2} , thermal) is calculated. This estimation shows that such bismuth samples should result in an isotopic ratio of $^{210\text{m}}\text{Bi}/^{209}\text{Bi}$ of about $3 \cdot 10^{-11}$.

$$\frac{N_{210\text{m}}\text{Bi}}{N_{209}\text{Bi}} = \Phi \cdot \sigma_{m,th} \approx 1.5 \cdot 10^{15} \frac{1}{\text{cm}^2} \cdot 20 \cdot 10^{-27} \text{cm}^2 \approx 3 \cdot 10^{-11} \quad (4.6)$$

According to equation 4.6 bismuth samples that were irradiated for about five minutes ($=300$ s) with thermal neutrons at the Atominstitut should have a similar isotopic ratio of $^{210\text{m}}\text{Bi}/^{209}\text{Bi}$ as samples irradiated at Forschungszentrum Karlsruhe.

4 Determination of the neutron capture cross-section of $^{209}\text{Bi}(n,\gamma)^{210(\text{g+m})}\text{Bi}$

5 Neutron Irradiations

The number of nuclei (N_B) that capture a neutron is calculated by 5.1, where N_0 is the number of nuclei in the sample. If the half-life of the produced isotope is short compared to the time of irradiation, its decay during irradiation must be considered. Equation 5.1 assumes further that N_B is zero at the beginning of the irradiation:

$$\frac{dN_B}{dt} = \sigma N_0 \Phi - \lambda N_B(t) \quad (5.1)$$

The neutron fluence Φ [n cm^{-2}] is the time integrated neutron flux φ [$\text{n cm}^{-2} \text{ s}^{-1}$]. Integrating equation 5.1 gives the number of produced nuclei after an irradiation period T (irrespective of the decay):

$$N_B(T) = \frac{\sigma N_0 \Phi}{\lambda_B} \cdot (1 - e^{-\lambda_B T}) \quad (5.2)$$

Equation 5.3 specifies the number of produced nuclei at any time t after the end of irradiation. The exponential decay of the produced nuclei according to its half-life is considered in this equation. T_{irr} is the time period during which the sample was irradiated. t_I^E is the time when the irradiation was stopped. In equation 5.3 the neutron flux is assumed to be constant during irradiation.

$$N_B(t) = \sigma N_0 \Phi \cdot \frac{(1 - e^{-\lambda_B T_{irr}})}{\lambda_B} \cdot e^{-\lambda_B(t-t_I^E)} \quad (5.3)$$

5.1 Irradiation at the Atominstitut in Vienna with thermal neutrons

The irradiation with thermal neutrons ($kT \approx 25 \text{ meV}$) was carried out at the Atominstitut in Vienna. A TRIGA Mark-II reactor¹ was used for neutron activation. This reactor is a research reactor of the swimming-pool type. It is in use since 1962 and its maximum continuous power output is

¹TRIGA=Training, Research, Isotope Production, General Atomic

250 kW (thermal).

For this experiment bismuth samples were irradiated in a tube next to the core at a typical neutron flux of about $4 \cdot 10^{11} \text{ n cm}^{-2} \text{ s}^{-1}$. At this position a fairly acceptable thermal spectrum is available. The epithermal fraction of the neutron spectrum at this position is only about 1-2% [37].

As the reactor operates with a constant power output the neutron flux was assumed to be constant in time.

Up to now eight irradiation series were performed and in total 24 different bismuth samples were produced. The first samples were irradiated in February 2006 and the last irradiation considered in this thesis took place in April 2009. However, not all of these 24 samples were measured with AMS till May 2009.

Table 5.1 shows an overview of the 24 bismuth samples irradiated with thermal neutrons. It includes date and time of the neutron irradiation at the Atominstitut and also the sample masses². All samples were irradiated as metallic powder filled in a plastic vial. Only for sample *Bi_TabA*, *Bi_TabB* and *Bi_TabC* metallic bismuth powder was pressed to a pellet. The bismuth powder is from Alfa Aesar GmbH & Co KG (purity of 99.999%).

²The masses of Bi_8 and Bi_9 are an estimation

Sample name	Mass [g]	Date of Irradiation	Start time	Duration [min]
Bi_1	0.94	23.02.2006	12:58	60
Bi_2	1.09	24.02.2006 27.02.2006	08:49 08:45	$\left. \begin{matrix} 416 \\ 90 \end{matrix} \right\} = 476$
Bi_3	0.23	31.05.2006	09:07	390
Bi_4	0.10	31.05.2006	08:57	73
Bi_5	0.12	31.05.2006	10:19	5
Bi_8	≈ 1	13.03.2007	11:02	5.5
Bi_9	≈ 1	13.03.2007	11:18	60
Bi_10	1.39	07.02.2008	09:42	72
Bi_11	1.76	07.02.2008	10:04	10
Bi_12	1.51	07.02.2008 08.02.2008	10:53 08:56	$\left. \begin{matrix} 292 \\ 417 \end{matrix} \right\} = 709$
Bi_13	1.09	07.02.2008 08.02.2008	10:53 08:56	$\left. \begin{matrix} 292 \\ 417 \end{matrix} \right\} = 709$
Bi_14	2.33	26.03.2008	10:35	310
Bi_15	2.95	26.03.2008	09:09	74
Bi_16	2.54	26.03.2008	10:35	310
Bi_17	2.48	26.03.2008	09:08	10
Bi_18	1.06	19.06.2008	09:03	61
Bi_19	0.78	19.06.2008	09:03	61
Bi_20	0.63	03.09.2008	09:36	152
Bi_21	0.60	03.09.2008	09:36	152
Bi_22	0.69	19.11.2008	10:45	73
Bi_TabA	0.74	19.11.2008	10:45	73
Bi_23	0.19	19.11.2008	11:58	10
Bi_TabB	0.34	22.04.2009	14:14	93
Bi_TabC	0.29	22.04.2009	14:14	93

Table 5.1: Overview of bismuth samples irradiated with thermal neutrons ($kT \approx 25$ meV) at the Atominstitut in Vienna. Only irradiations after October 2007 were performed during this thesis.

5.1.1 Determination of the neutron fluence

For the determination of the neutron fluence Φ at the sample position, neutron monitor foils were used. As neutron monitors thin foils of zirconium (0.1 mm thickness), with a mass of about 20 mg, or thin gold foils (0.02 mm thickness) with a mass of about 2 mg, were utilised. These foils were placed on the vial next to the bismuth powder with adhesive tape. The neutron capture cross-section values at $E_n=25$ meV (σ_{therm}) for both materials are listed in table 5.2.

	σ_{therm} [barn]
^{94}Zr	0.0494 ± 0.0017 [38]
^{98}Au	98.65 ± 0.09 [39]

Table 5.2: Thermal neutron capture cross-sections for zirconium and gold.

The cross-section of $^{197}\text{Au}(n,\gamma)^{198}\text{Au}$ is used as a standard for irradiations with thermal neutrons. Due to the rather high capture cross-section for thermal neutrons and the short half-life of ^{198}Au ($t_{1/2}=2.69$ days [40]), the activity of the gold foils after neutron irradiation is much higher than the activity of the bismuth sample and the zirconium monitor foils (see table 5.2). A zirconium fluence monitor foil with a mass of 20 mg has just 1 ‰ of the activity of a gold monitor of 1 mg. This is exemplified in equation 5.4 and 5.5 for a neutron irradiation of one hour and a flux of $4 \cdot 10^{11}$ n cm⁻² s⁻¹ (i.e. a neutron fluence (Φ) of $1.5 \cdot 10^{14}$ n cm⁻²). The total activity of zirconium results primarily from the decay of ^{95}Zr and ^{97}Zr . The specific isotope abundance of zirconium is listed in table 5.3. The half-life of ^{95}Zr is 64.03 days [41] and the half-life of ^{97}Zr 16.8 hours [42]. The activity of ^{93}Zr can be neglected due to the long half-life of ^{93}Zr ($1.5 \cdot 10^5$ years [43]). Due to the high activity of the gold foils, their transport from the Atominstitut to VERA was not possible directly after the irradiation and the handling of the material was more complicated³. That was the reason why zirconium foils were used more often.

$$A(^{198}\text{Au}) = \lambda_{198\text{Au}} \cdot N(^{198}\text{Au}) \approx 1300\text{kBq} \quad (5.4)$$

³The Atominstitut and the VERA facility are in a distance of about 8 kilometres and public transport was used.

$$A(^{95}\text{Zr}) = \lambda_{95\text{Zr}} \cdot N(^{95}\text{Zr}) \approx 200\text{Bq}$$

$$A(^{97}\text{Zr}) = \lambda_{97\text{Zr}} \cdot N(^{97}\text{Zr}) \approx 1400\text{Bq}$$

$$A(^{95}\text{Zr}) + A(^{97}\text{Zr}) = 1600\text{Bq} \quad (5.5)$$

In contrast to gold monitors, with ^{197}Au as the only stable isotope, zirconium has five stable isotopes. The abundance of each stable zirconium isotope is shown in table 5.3.

Isotope	Abundance [%]
^{90}Zr	51.45
^{91}Zr	11.22
^{92}Zr	17.15
^{94}Zr	17.38
^{96}Zr	2.8

Table 5.3: List of stable zirconium isotopes

As mentioned above the reaction $^{94}\text{Zr}(n,\gamma)^{95}\text{Zr}$ is also used to determine the neutron fluence. The ratio of the neutron-capture cross-section at thermal energies to epithermal energies is much higher for ^{96}Zr than for ^{94}Zr (see [44]). Therefore the combination of ^{94}Zr and ^{96}Zr allows to quantify the epithermal fraction of the neutron spectrum (about 1-2% [37]).

To determine the neutron fluence Φ the activity of the monitor foils had to be measured. Therefore, a High-Purity Germanium Detector (HPGe) was used. The relevant gamma rays associated with the decay of ^{95}Zr and ^{198}Au are listed in table 5.4. The specific half-lives of ^{95}Zr and ^{198}Au are given in this table as well.

	Half-life [d]	Energy [keV]	Intensity [%]
^{95}Zr	64.03 [41]	724.2	44.3
		756.7	54.4
^{198}Au	2.69 [40]	411.8	95.6

Table 5.4: Gamma lines used for fluence measurements in this work (www.nndc.bnl.gov/nutdat2)

5 Neutron Irradiations

The following values have to be known for the determination of the neutron fluence via activity measurement (equation 5.7-5.9): the neutron capture cross-section, activity, decay constant, gamma ray intensity and times of neutron irradiation and activity measurement.

The following equations (5.6-5.9) [45] describe how the neutron fluence is calculated from the activity ($A(t)$) of a monitor foil. T_m is the measurement duration. First, the activity is corrected for those particles that have decayed during the activity measurement:

$$A(t)_{cor} = \frac{A(t)\lambda}{1 - e^{-\lambda T_m}} \quad (5.6)$$

The neutron fluence Φ can then be calculated by equation 5.7:

$$\Phi = \frac{A(t)_{cor}}{N_0 \cdot \sigma \cdot \lambda \cdot f} \quad (5.7)$$

In this equation N_0 is the number of atoms in the sample and f is a decay correction factor defined by equation 5.8. With f the activity is back-calculated to the time when the irradiation was stopped. Further, decay during the irradiation itself is considered (T_{irr} is the irradiation duration). t_M^A defines the time when the activity measurement started and t_I^E the time, when the irradiation stopped.

$$f = \frac{(1 - e^{-\lambda T_{irr}})}{T_{irr} \cdot \lambda} \cdot e^{-\lambda(t_M^A - t_I^E)} \quad (5.8)$$

The count rate (Z), measured with a HPGe, is correlated with the activity via the detector efficiency (ϵ_{Det}) and the gamma ray intensity (I_γ):

$$A = \frac{Z}{\epsilon_{Det} \cdot I_\gamma} \quad (5.9)$$

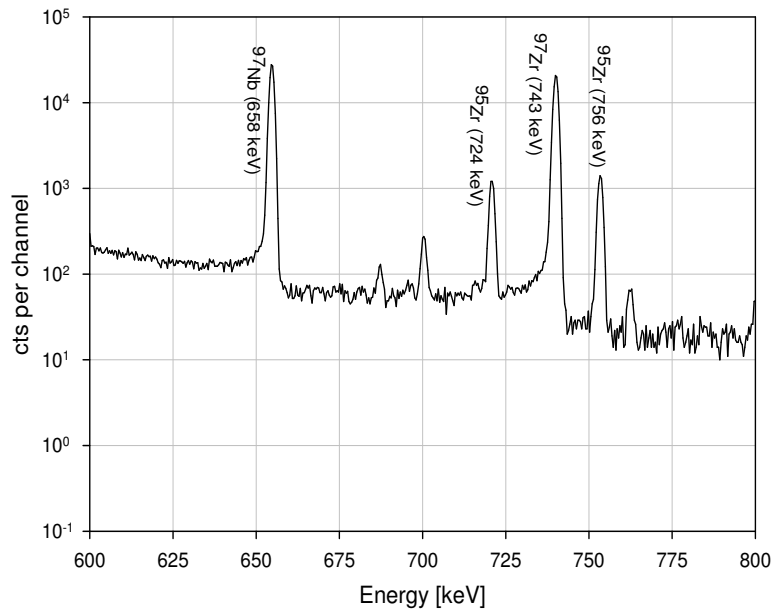
The count rate (Z) in equation 5.9 is corrected for dead-time losses.

^{198}Au decays to stable ^{198}Hg via β -decay. Only one γ -ray line at $E=411$ keV exists in a γ -ray spectrum of a gold monitor foil. On the other hand, several γ -ray lines can be seen in the γ -ray spectrum of a zirconium monitor foil. As mentioned above, there are two γ -ray lines of interest produced by the decay of ^{95}Zr (see table 5.4). Another γ -ray is produced by the decay of ^{97}Zr at $E=743$ keV. ^{97}Zr decays with a half-life of 16.8 hours to ^{97}Nb . ^{97}Nb itself decays to stable ^{97}Mo via β -decay producing another γ -ray peak at 658 keV. Later, another γ -ray peak occurs at

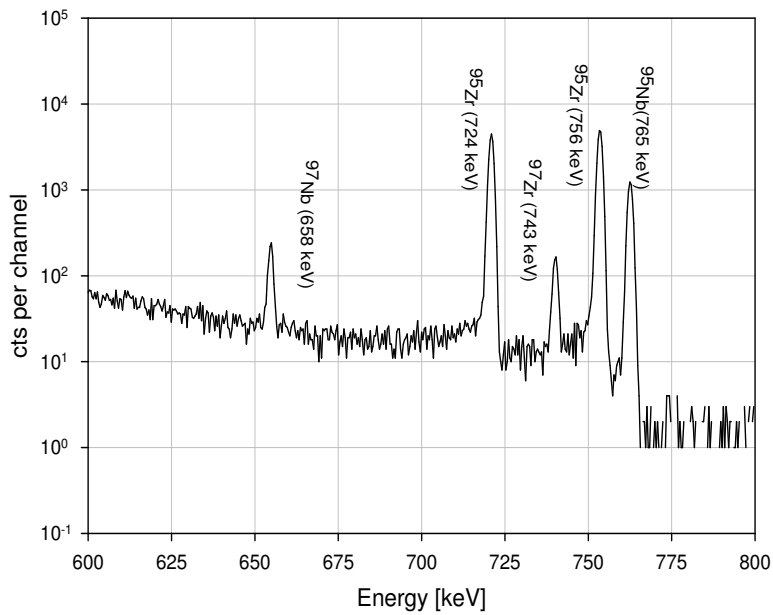
765 keV. It is produced by the β -decay of ^{95}Nb which is formed by the β -decay of ^{95}Zr with a half-life of 64 days. ^{95}Nb itself decays to ^{95}Mo with an half-life of 34.97 days. A γ -ray spectrum of a zirconium flux monitor, one and seven days after neutron irradiation, is presented in figure 5.1.

The first samples irradiated at the Atominstitut (sample Bi_1 to Bi_13) were equipped only with one flux monitor. Experiments showed that, depending on the position of the monitor foil on the vial, the measured neutron fluence can vary up to ten percent. Therefore, more monitors were placed around the sample in later experiments. The variation of the neutron fluence is shown by means of an example in the following chapter.

The uncertainty of the neutron fluence is dominated by the statistical uncertainty of the counts registered by the HPGe detector, the uncertainty of the detector efficiency and the uncertainty of the neutron capture cross-section of $^{94}\text{Zr}(n,\gamma)^{95}\text{Zr}$ or $^{197}\text{Au}(n,\gamma)^{198}\text{Au}$. The statistical uncertainty was typically below one percent. The uncertainty of detector efficiency was about two percent. The quoted uncertainty of the cross-sections of $^{94}\text{Zr}(n,\gamma)^{95}\text{Zr}$ and $^{197}\text{Au}(n,\gamma)^{198}\text{Au}$ is 3.5% [38] and 0.09% [39], respectively. Table 5.5 shows neutron flux and fluence of all bismuth samples irradiated at the Atominstitut. The irradiation of the samples marked with * took place at a reactor power of only 200 kW, while all other bismuth samples were irradiated with a reactor power of 250 kW. The constant reactor power ensured a constant time-independent neutron flux during the irradiation. The numbers of the fluence monitors in table 5.5 indicate different foils.



(a) 1 day after neutron irradiation



(b) 7 days after neutron irradiation

Figure 5.1: Zirconium spectra with different waiting times after the neutron irradiation

Sample	Monitors	Flux [·10 ¹¹ n cm ⁻² s ⁻¹]	Fluence [·10 ¹⁵ n cm ⁻²]	^{210m} Bi/ ²⁰⁹ Bi [·10 ⁻¹¹]
Bi1	Zr_30	4.5 ±0.2	1.6±0.1	3.2
Bi2	Zr_47	4.3 ±0.2	13±1	26
Bi3	Zr_12	4.2 ±0.2	10±1	20
Bi4	Zr_102	4.2 ±0.2	1.9±0.1	3.7
Bi5	Zr_23	4.7 ±0.2	0.15±0.01	0.3
Bi8	Zr_20	3.5 ±0.2	0.12±0.01	0.2
	Au_1	3.6 ±0.2	0.12±0.01	0.2
Bi9	Zr_84	4.7 ±0.2	1.7±0.1	3.4
Bi10	Zr_47	4.3 ±0.2	1.8±0.1	3.7
Bi11	Zr_14	4.7 ±0.2	0.28±0.01	0.6
Bi12	Zr_23	4.9 ±0.2	21±1	42
Bi13	Zr_64	4.2 ±0.2	18±1	36
Bi14	Zr_11/11; Zr_11/Z	4.4 ±0.2	8.2±0.4	16
Bi15	Zr_31; Zr_36; Zr_89; Zr_108	4.3 ±0.2	1.90±0.08	3.8
Bi16	Zr_42; Zr_43	4.1 ±0.2	7.6±0.3	15
Bi17	Zr_76; Zr_146; Zr_148	3.8 ±0.3	0.23±0.01	0.5
Bi18	Zr_F; Zr_40; Zr_H; Zr_20	4.0 ±0.2	1.47±0.06	2.9
Bi19	Zr_48; Zr_B; Zr_29; Zr_A	4.3 ±0.2	1.56±0.06	3.1
Bi20	Zr_53; Zr_Z/F Zr_Z/H; Zr_Z/Z	4.3 ±0.2	3.9±0.2	7.8
Bi21	Zr_88; Zr_103; Zr_37; Zr_Z/T	4.1 ±0.1	3.7±0.1	7.4
Bi22*	Au_77; Au_106	3.1 ±0.1	1.35±0.04	2.7
	Zr_1	3.4 ±0.5	1.5±0.2	3.0
BiTabA*	Au_174; Au_94	3.3 ±0.1	1.44±0.04	2.9
Bi23*	Zr_4; Zr_7	3.6 ±0.2	0.21±0.01	0.4
BiTabB	Au_134; Au_121	4.5 ±0.1	2.49±0.03	5.0
BiTabC	Au_132; Au_235	4.2 ±0.1	2.36±0.04	4.7

Table 5.5: Neutron flux and fluence of bismuth samples that were irradiated with thermal neutrons at the Atominstitut. The uncertainties are rounded. In the last column an estimation for the ^{210m}Bi/²⁰⁹Bi isotope ratio is shown, assuming a thermal neutron-capture cross-section of 20 mbarn.

Example: fluence determination - Bi19

The determination of the neutron fluence is presented as an example in the following chapter. The vial containing the bismuth sample Bi19 was equipped with four zirconium foils. All foils were put at the vial an with adhesive tape.

All zirconium foils were measured for several hours and every hour one spectrum was saved. Typical spectra are shown in figure 5.1. Two γ -lines were used for further calculations: at 724 and 756 keV. Both originate from the decay of ^{95}Zr . The spectra were evaluated with *WIRUK plus* software⁴. The neutron fluence of each foil was calculated as described in equations 5.6-5.9. As both γ -ray lines were evaluated, two values for each fluence monitor were calculated. This can be seen in table 5.6. The uncertainties in table 5.6 were calculated

Name	$\Phi (E_{\gamma}=724 \text{ keV})$ [$\cdot 10^{15} \text{ n cm}^{-2}$]	$\Phi (E_{\gamma}=754 \text{ keV})$ [$\cdot 10^{15} \text{ n cm}^{-2}$]
Zr_48	1.48 \pm 0.06	1.50 \pm 0.06
Zr_B	1.54 \pm 0.06	1.54 \pm 0.06
Zr_29	1.61 \pm 0.07	1.63 \pm 0.07
Zr_A	1.60 \pm 0.07	1.60 \pm 0.07

Table 5.6: Values for the neutron fluence of Bi_19. The uncertainties are explained in the text.

from the statistical uncertainty (<1%), the uncertainty of the detector efficiency (2%) and the uncertainty of the neutron cross-section of $^{94}\text{Zr}(n, \gamma)^{95}\text{Zr}$ (3.5%). The neutron fluence of Zr_29 is about 10% higher than the fluence obtained from the opposing Zr_48. Other bismuth samples equipped with four fluence monitors showed a similar behaviour. This shows that an uncertainty of $\pm 5\%$ has to be assumed for samples measured with one fluence monitor. The highest discrepancy was found for opposite positioned foils. The differences between the fluence calculated from the counts in the full energy peak at $E=724 \text{ keV}$ and $E=756 \text{ keV}$ are within the uncertainties (table 5.6).

In the example above the mean value of the neutron fluence of the bismuth powder results in $(1.56 \pm 0.06) \cdot 10^{15} \text{ n cm}^{-2}$.

Sample Bi_22 was equipped with two gold foils (Au_77, Au_106) at opposite sides of the vial. The results of the calculated fluence were: $\Phi(\text{Au}_77) = (1.41 \pm 0.07) \cdot 10^{15} \text{ n cm}^{-2}$ and

⁴copyright by Harry Friedmann, Version 0.1.0

$\Phi(\text{Au}_{106})=(1.29\pm 0.06)\cdot 10^{15}\text{ n cm}^{-2}$. This agrees with a neutron fluence difference of up to 10% between both positions.

The accuracy of neutron fluence determination increases by using bismuth powder pressed to a pellet. Sample Bi_TabA was produced by pressing 0.74 grams of metallic bismuth powder to a pellet with 9 mm in diameter. Gold foils were fixed at both sides of the pellet with adhesive tape. A neutron fluence of $1.44\cdot 10^{15}\text{ n cm}^{-2}$ was calculated for both monitors. The neutron fluence of the flux monitors of Bi_TabB also agrees within the uncertainty given by the count rate and detector efficiency.

Future neutron irradiation at the Atominstitut should be performed as pellets, if possible, because two monitor foils uniquely determine the mean neutron fluence of the pellet.

5.2 Neutron irradiation at Forschungszentrum Karlsruhe with "25 keV" neutrons

Two bismuth pellets (6 mm in diameter) were irradiated at Forschungszentrum Karlsruhe (FZK) before this thesis started. A 3.7 MV Van de Graaf accelerator called "Lolita" was used to produce neutrons via a (p,n) reaction bombarding a lithium target. The generated neutrons have a quasi-Maxwellian energy distribution of $kT=25\pm 0.5\text{ keV}$ [46]. The proton energy was 1912 keV, which is slightly above the threshold of the reaction ($E_{th}=1881\text{ keV}$). In this way a collimated neutron beam in a forward cone with an opening angle of 120° was obtained. A ${}^6\text{Li}$ glass detector to monitor the neutron flux in intervals of 1 minute (or 99 seconds) was placed 90 cm from the lithium target (figure 5.2) [22].

The samples irradiated at FZK are denoted as BiFZK_A and BiFZK_B. BiFZK_A was irradiated between the 22.12.2006, 14:51 and 17.1.2007, 2:09 in four irradiation periods. The total time of neutron irradiation for BiFZK_A was 20681 minutes. BiFZK_B was irradiated from 2.3.2007, 15:41 to 11.3.2007, 9:22 (duration=12581 minutes). The neutron fluences were determined by Sara Bisterzo [47] and are listed in the following table:

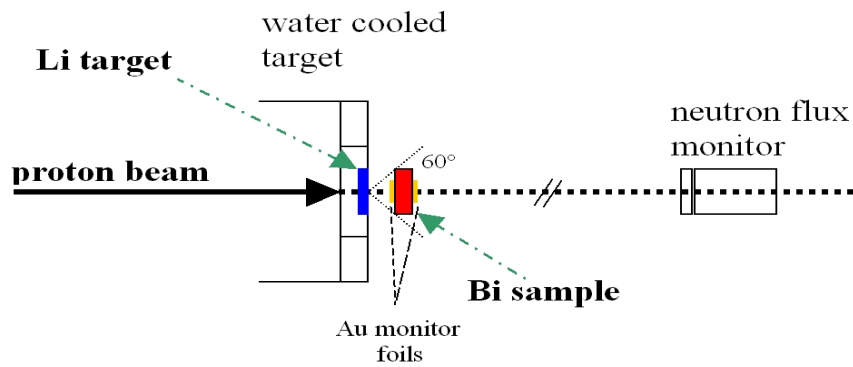


Figure 5.2: Schematic setup of the neutron irradiation at Forschungszentrum Karlsruhe

Sample	Fluence [$n \text{ cm}^{-2}$]
BiFZK_A	$(6.29 \pm 0.06) \cdot 10^{14}$
BiFZK_B	$(1.30 \pm 0.02) \cdot 10^{15}$

Table 5.7: Bismuth samples irradiated at Forschungszentrum Karlsruhe with $kT=25 \text{ keV}$ [47]

6 Accelerator Mass Spectrometry (AMS)

6.1 The principle of AMS

Accelerator mass spectrometry (AMS) is a sensitive technique to measure long-lived radioisotopes by counting individual atoms with nuclear detection techniques after acceleration to energies in the MeV range [48]. A certain radioisotope is selected by the use of magnetic and electric fields. The concentration of this isotope in a sample is determined by comparing the count rate with the ion current of a stable isotope in the sample. The measured isotope ratio is compared to the measured value of a standard material with known isotopic ratio to obtain absolute values. Blank material is measured to determine background effects or to monitor sample preparation effects.

AMS applications exist in various areas like nuclear physics, archaeology, atmospheric science, astrophysics, etc.

Almost all AMS-systems consist of two mass spectrometers: a low energy injector and a high energy analyser linked with a tandem accelerator (Fig. 6.1).

6.2 VERA - an overview

The Vienna Environmental Research Accelerator (VERA) has been in operation since 1996 [49]. All components are designed to allow the transport from light elements like beryllium to heavy elements like bismuth or uranium. VERA is also used for the search of super heavy elements (SHE). ^{10}Be , ^{14}C , ^{26}Al , ^{36}Cl , ^{41}Ca , ^{55}Fe , ^{129}I , ^{182}Hf , ^{210}Pb , ^{236}U , $^{239-244}\text{Pu}$ are radioisotopes that have been measured successfully at VERA [50] [51] [52]. A proton beam is also used to study art objects via PIXE [53].

The description of key elements of VERA is based on [54], [49] and [55]. Figure 6.1 shows an

actual sketch of the VERA facility with more elements as described in this chapter, for more detailed information on this elements see for example [54].

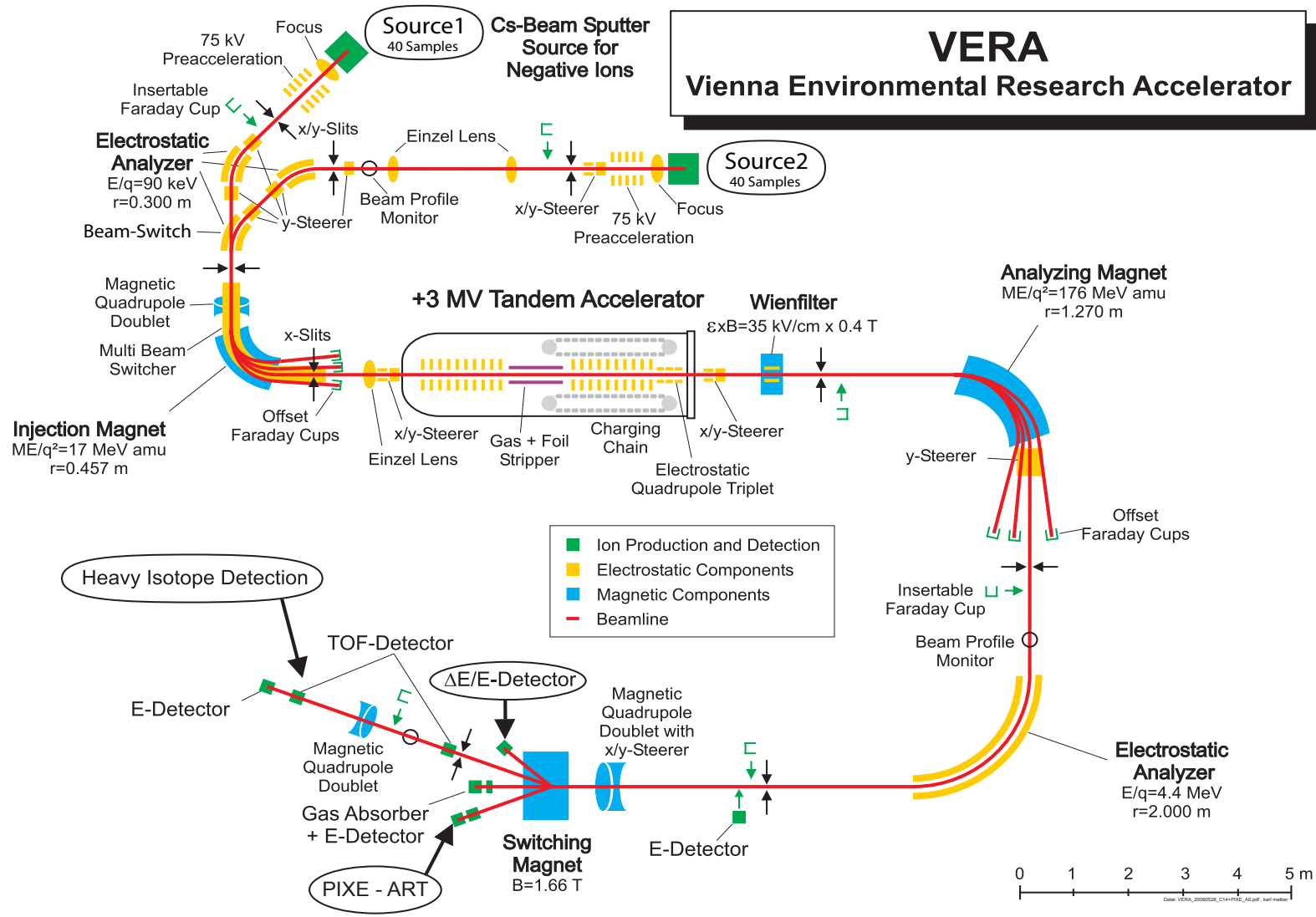


Figure 6.1: VERA scheme 2008

6.2.1 Ion source

VERA uses a MCSNICS¹ ion source with a sample wheel for 40 cathodes. Negative ions are leaving the source with an energy of about 70 keV. A positively charged caesium beam is accelerated towards the target and sputters the sample material of a target cathode.

Not all isotopes produce negative ions in the same amount. A problem when measuring ²¹⁰Bi is, that the isobar ²¹⁰Po forms more readily negative ions than ²¹⁰Bi.

6.2.2 Magnetic deflection systems

Charged particles crossing a magnetic field (\vec{B}) with velocity \vec{v} are deflected because of the Lorentz force (F_L) (equation 6.1).

$$F_L = q \cdot (\vec{v} \times \vec{B}) \quad (6.1)$$

The Lorentz force as the centripetal force ($F = mv^2/r$), results in the magnetic rigidity $B \cdot r$ (see equation 6.2) for a defined radius of the trajectory in the magnet (r) and a constant magnetic field perpendicular to the direction of the ions. In equation 6.2, E is the kinetic energy of the particle, m its mass and q the charge state of the ion.

$$B \cdot r = \frac{\sqrt{2mE}}{q} \quad (6.2)$$

According to the equation 6.2, ions with a certain magnetic rigidity are selected by magnetic bending elements (analysing magnets).

As seen in figure 6.1 also a switching magnet is mounted. This switching magnet is important at VERA for additional background suppression.

The MBS system at VERA

At VERA the Multi Beam Switcher (MBS) modulates the kinetic energy of the ions. It applies a supplement acceleration voltage (max. 13 keV) to the chamber of the injection magnet. In equation 6.2, it can be seen that particles with the same mE (and the same charge state) experience the same deflection in a constant magnetic field. With the MBS it is possible to inject isotopes with different mass into the accelerator without changing the magnetic field.

¹MCSNICS=Multi Cathode Source for Negative Ions by Caesium Sputtering

Three different values are used for measuring the ion current of the stable isotope on both, the low ($^{209}\text{Bi}^-$) and the high energy side ($^{209}\text{Bi}^{5+}$); one value is used to count the rare isotope in the detector ($^{210}\text{Bi}^{5+}$).

6.2.3 Electrostatic deflection systems

In an electrical field (ϵ) charged particles are deflected due to the electric force ($F_\epsilon = q \cdot \epsilon$). The electrical force as the centripetal force results in a certain energy over charge ratio for a defined radius r (equation 6.3). For a fixed charge state an electrostatic element (electrostatic analyser - ESA) is energy selective.

An electrostatic element in combination with an analysing magnet acts, therefore, as a filter for a certain m/q ratio.

$$\frac{E}{q} = \frac{\epsilon \cdot r}{2} \quad (6.3)$$

6.2.4 The tandem accelerator

At VERA, a +3-MV tandem accelerator of the Pelletron type (model 9SDH-2) is used. It is installed inside a tank filled with SF_6 at a pressure of about 6 bar. Two charging chains transport charge to the terminal. A constant terminal voltage, necessary for maintaining a constant beam energy at the high energy analyser side, is controlled with a generating voltmeter and adjusted via a corona probe. The acceleration of ions happens in two steps. First, the negative ions entering the tandem are accelerated towards the terminal, where they strip off electrons in the so called "stripper", a gas volume or a foil, and get a positive charge. This allows to use the terminal voltage a second time to accelerate the now positively charged ions. The energy of the ions after the acceleration is given by equation 6.4 where M_{inj} is the injected mass of the ion or molecule, M is the atomic mass of the isotope of interest and q the charge state. U_T is the terminal voltage and E_{inj} is the energy of the ion before entering the accelerator.

$$E = (E_{inj} + U_T) \frac{M}{M_{inj}} + qU_T \quad (6.4)$$

At VERA the stripper channel is filled with O_2 . There is also the possibility for foil stripping. Two turbo pumps at the terminal re-circulate the stripper gas. Molecules break up during the

stripping process when enough electrons are stripped off. The fragments of the molecules have to be separated from the desired mass number by the analysing magnet on the high energy side (based on [54]).

6.2.5 Wien Filter

A Wien filter is a combination of an electric field perpendicular to a magnetic field. Both are perpendicular to the velocity of the ions (\vec{v}), but act in opposite directions. A Wien Filter is velocity selective since for particles not deflected the electric force equals the Lorentz force. It results in equation 6.5.

$$qvB = qE \rightarrow v = \frac{E}{B} \quad (6.5)$$

6.2.6 The heavy ion detector

Following the +20° exit port of the switching magnet the heavy ion detector system is mounted. This detector measures time-of-flight and absolute energy of the particles. With the energy signal, mass/charge ambiguities are discriminated as particles gain different energies in the accelerator due to their different charge state. The time-of-flight (TOF) is determined by two timing detectors. The distance between them is 2.8 m. In a timing detector the ions induce secondary electrons at a thin carbon foil. Then, the electrons are reflected by an electrostatic mirror. A micro channel plate collects and multiplies the electrons. The outgoing pulse is a very short negative pulse. The start and stop signals are amplified and fed into a time-to-amplitude converter (TAC). For the energy measurement an ionisation chamber where the ions are stopped in a gas volume (Bragg type) is used. For more information about the heavy ion detector see [55].

6.2.7 Beam analysing elements

Faraday cup: A Faraday cup measures the current of an ion beam.

Slits: Slits are used to analyse the position of the beam by narrowing and moving the slits.

7 Measuring $^{210\text{m}}\text{Bi}$ at VERA

Twelve beam-times were devoted to ^{210}Bi till April 2009 at VERA. During this thesis seven beam-times were performed. In the following they are denoted as Bi_ng6 to Bi_ng12. Due to technical problems no data were achieved during Bi_ng8 and Bi_ng9.

Metallic bismuth powder¹ and powder that was irradiated with neutrons (see chapter 5) were measured during the beam-times.

The ^{210}Po content of neutron irradiated samples is discussed later in this chapter (see 7.5).

For the measurement at VERA, bismuth samples are pressed into aluminium cathodes containing 5 to 15 mg of the sample material. The target wheel was made from aluminium. For $^{210\text{m}}\text{Bi}$ measurements a terminal voltage between 2.8 and 3.0 MV was used. O_2 stripping gave a charge-state-yield of 5-6% for the +5 charge state ($q=+5$). The charge state distribution was not measured yet. Bismuth is sputtered in the ion source and $^{209}\text{Bi}^-$ is injected into the accelerator. The selected $^{209}\text{Bi}^{5+}$ beam passes the high energy analysing magnet. To determine the transmission between low energy and high energy side, the $^{209}\text{Bi}^-$ current is measured in the offset Faraday cup immediately after the injection magnet and the $^{209}\text{Bi}^{5+}$ current in the Faraday cup FC04 positioned after the analysing magnet (see fig. 7.1). The $^{210\text{m}}\text{Bi}$ particles are detected with the TOF-system (see chapter 6.2.6). The adjustable MBS voltage in the injector magnet chamber allows to switch between mass $A=209$ and $A=210$. The isotopic ratio $^{210\text{m}}\text{Bi}/^{209}\text{Bi}$ is calculated from the ratio between the counted events ($A=210$) with the TOF-system and the $^{209}\text{Bi}^{5+}$ current measured in FC04. The number of events with $A=210$ has to be background corrected, therefore bismuth blank material was also measured together with neutron irradiated material. Two possibilities of background correction are explained in chapter 7.3.

¹Similar to the irradiated bismuth powder from Alfa Aesar GmbH & Co KG with a purity of 99.999%.

Samples measured with AMS are usually normalised to a standard material, which is measured alternating to the sample. In equation 7.1 R denotes an isotope ratio, “std” a standard material, “nom” a nominal value and “meas” the value measured with AMS.

$$R_{\text{sample}} = R_{\text{std,nom}} \cdot \frac{R_{\text{sample,meas}}}{R_{\text{std,meas}}} \quad (7.1)$$

However, in case of bismuth no standard material exists, so the absolute value of beam losses between FC04 and the TOF-system has to be determined. In chapter 7.4.2 it is shown that the determination of these beam losses is only possible with poor accuracy. Therefore, the measured $^{210\text{m}}\text{Bi}/^{209}\text{Bi}$ isotope ratio are mostly presented in arbitrary units, not normalised for beam losses. The isobar of $^{210\text{m}}\text{Bi}$ is ^{210}Po , formed by the β -decay of $^{210\text{g}}\text{Bi}$. ^{210}Po cannot be separated from $^{210\text{m}}\text{Bi}$ with AMS, so it was separated chemically (see chapter 7.5.2) or the ^{210}Po content was estimated numerically (chapter 7.5.1). For such a ^{210}Po correction the negative ion formation probability of bismuth and polonium was measured (chapter 7.4.1). The ratio between these negative ion formation probabilities results in the polonium scale factor.

7.1 Tuning procedure

The magnetic field of the injector magnet at the low energy side and of the analysing magnet at the high energy side were set to nominal values calculated by equation 6.2. This resulted in a magnetic field of the injection magnet of about 11200 G. The energy of the $^{209}\text{Bi}^-$ ions was 63 keV at the low energy side. The terminal voltage was 3.0 MV and the energy of the particles at the high energy side ($q=5+$) 18.0 MeV. This resulted in a magnetic field of 13700 G for the analysing magnet to transport $^{209}\text{Bi}^{5+}$ ions. These values are close to the limits of the magnets i.e. 12800 G for the injection magnet and 14800 G for the analysing magnet.

The $^{210\text{m}}\text{Bi}$ beam is too weak to allow current measurements with Faraday cups. Therefore, a ^{209}Bi pilot beam is used to tune the components of VERA for $^{210\text{m}}\text{Bi}$ measurements. A script called “automax” [54] is used during the tuning process.

The positions of the Faraday cups described in the following can be seen in fig. 7.1. The low

energy components of VERA are tuned to achieve an optimal $^{209}\text{Bi}^-$ current in the Faraday cup FC02 after the injection magnet. Typical values for the $^{209}\text{Bi}^-$ current are several hundred nA. In some cases $^{209}\text{Bi}^-$ currents of up to $2\ \mu\text{A}$ were measured. The $^{209}\text{Bi}^-$ beam is injected into the accelerator and the 5+ charge state is selected. The $^{209}\text{Bi}^{5+}$ beam passes the analysing magnet and its intensity is measured in the Faraday cup FC04. All low energy components, the terminal voltage and the components between the tandem and FC04 are tuned by an automax script to get an optimal $^{209}\text{Bi}^{5+}$ current in FC04. Assuming a stripping efficiency of 5-6%, currents of about 100 nA are expected at FC04. Then, the $^{209}\text{Bi}^{5+}$ beam passes the electrostatic analyser ESA04 and is measured with Faraday cup FCL5 in the $+20^\circ$ beam line after the switching magnet BM04. The ESA04 and the other components between FC04 and FCL5 are optimised to give the same $^{209}\text{Bi}^{5+}$ current in FCL5 as measured in FC04 and thus minimise beam losses.

To tune and retune the components after BM03, the beam is attenuated (to a $^{209}\text{Bi}^-$ current of the order of magnitude of pA in FC02) by closing slits positioned of the ion source. Furthermore, two additional attenuators are inserted to reduce the beam intensity by another factor of about 5000. The measured count rate in the energy detector at the end of the beam line is therefore about $1 \cdot 10^4$ counts per second.

For $^{210\text{m}}\text{Bi}/^{209}\text{Bi}$ isotope ratio measurements the MBS is used to switch between mass $A=209$ and $A=210$ (see chapter 6.2.2). Reg0 is used to transport the $^{209}\text{Bi}^{5+}$ beam into FC04. To inject mass $A=210$ into the accelerator, a lower MBS voltage is calculated for reg3. To pass also the analysing magnet, the terminal voltage is changed for $^{210\text{m}}\text{Bi}$ measurements, according to 7.2. Reg2 is used to measure the $^{209}\text{Bi}^-$ beam in the offset Faraday cup behind the injection magnet².

$$E(209) \cdot m_{209} = E(210) \cdot m_{210} = \text{const} \rightarrow E(210) = E(209) \cdot \frac{m_{209}}{m_{210}} \quad (7.2)$$

²Reg1 is not used for $^{210\text{m}}\text{Bi}$ measurements

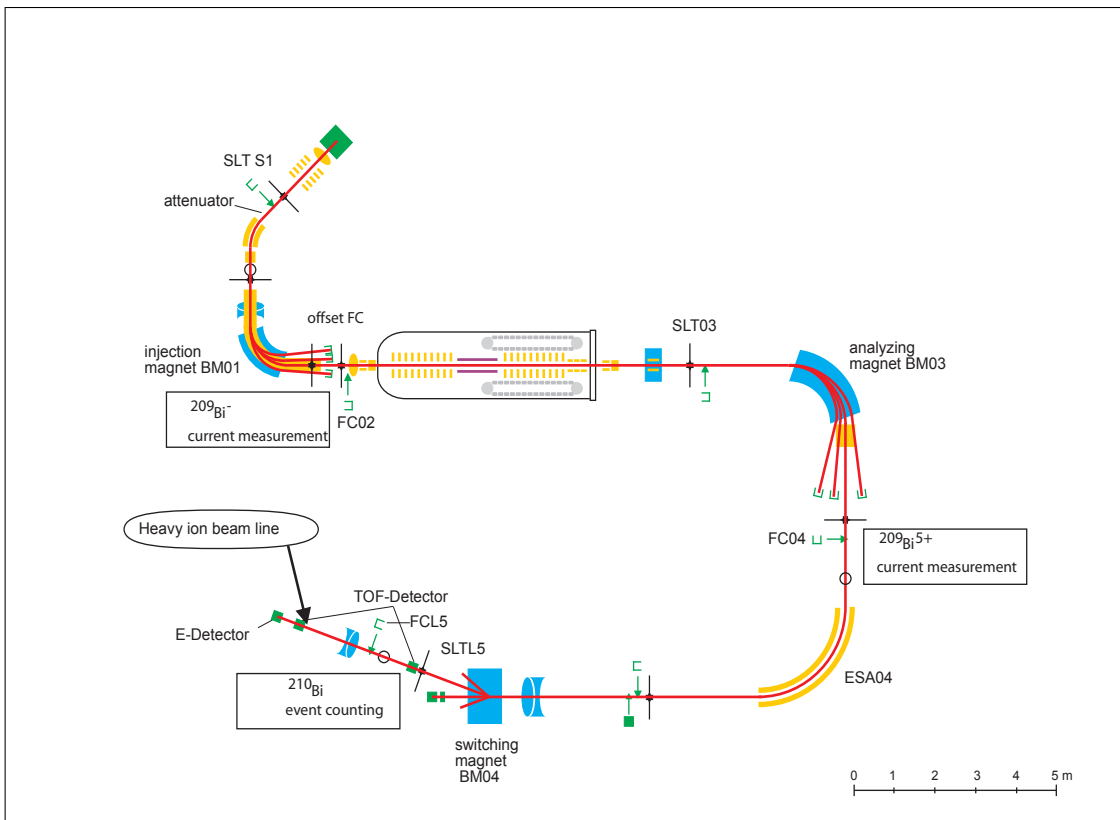


Figure 7.1: The VERA facility with relevant components for $^{210\text{m}}\text{Bi}/^{209}\text{Bi}$ isotope ratio measurements

7.2 Evaluation of a TOF-energy spectrum

The TOF-signal and the energy signal from the Bragg detector can be used to create a TOF-energy plot. A TOF-energy plot of a bismuth sample irradiated five hours with thermal neutrons is shown in figure 7.2. The ^{210}Po fraction, formed by the β -decay of $^{210\text{g}}\text{Bi}$ was separated chemically in this sample prior to the AMS measurement (see chapter 7.5).

Particles with the same $\frac{mE}{q^2}$ value have the same trajectory in the magnets. In combination with the selection of electrostatic deflection elements only the m/q term remains (see chapter 6). Particles with a different mass and charge state compared to $A=210$ but with the same m/q ratio follow the same trajectory as ^{210}Bi . ^{126}Te in the 3+ charge state, for example, has the same m/q ratio as ^{210}Bi in the 5+ charge state. As samples measured in other beam-times at VERA contained ^{126}Te , some relics of ^{126}Te were detected in the ionisation chamber. Table 7.1 lists stable isotopes with the same $\frac{m}{q}$ value as ^{210}Bi in the 5+ charge state. Noble gases are listed in parenthesis as they will not form negative ions.

charge state (q)	mass number (A)	stable isobar
1	42	^{42}Ca
2	84	^{84}Sr , (^{84}Kr)
3	126	^{126}Te , (^{126}Xe)
4	168	^{168}Yb , ^{168}Er
5	210	^{210}Po

Table 7.1: Isotopes with the same m/q as ^{210}Bi in $q=5+$.

The particle mass is related to the time-of-flight signal. ^{210}Bi needs a longer time-of-flight than ^{209}Bi . In fig. 7.2 it can be seen that the number of events due to ^{209}Bi is much higher than ^{210}Bi events. The center of the signals at mass $A=209$ and $A=210$ are so close to each other that ^{210}Bi counting is affected by ^{209}Bi events. This problem is discussed in chapter 7.3.

7.3 Bismuth blanks

^{209}Bi particles, injected into the accelerator as $^{209}\text{BiH}^-$, were detected in the TOF system. In the TOF-energy plot the center of events with mass of $A=209$ is at 685 ns (according to equation 7.3) and the center of events with mass of $A=210$ at 687 ns, very close to the “209 center” (fig.

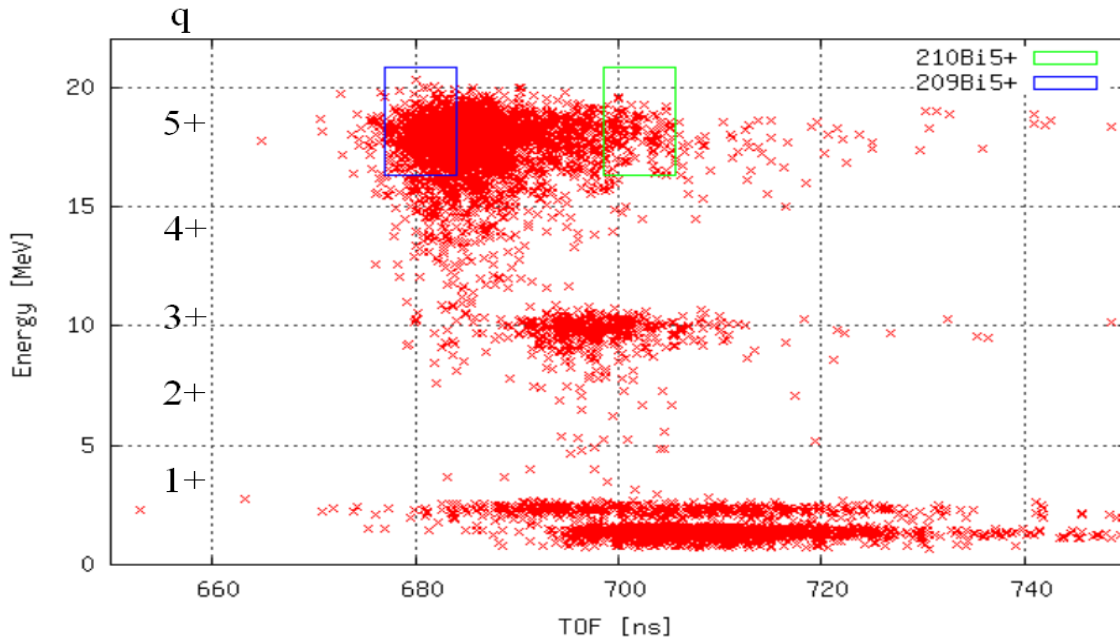


Figure 7.2: A typical TOF spectra of a neutron irradiated bismuth sample, the energy is plotted versus the time of flight. The blue marked area defines events with mass $A=209$ ($q=5+$) and the green marked area events with $A=210$ and $q=5+$.

7.2). In equation 7.3 x is the distance between start and stop detector (2.8 m), m the mass and E_{kin} the energy of the particles.

$$t = x \cdot \sqrt{m/(2E_{kin})} \quad (7.3)$$

The time resolution (FWHM) of the time-of-flight setup is at best 300-400 ps [55]³. Due to the high number of “209 events” (events that are assigned to mass $A=209$) the recording of $^{210\text{m}}\text{Bi}$ events is influenced by “209 events”. Therefore, a background correction has to be made by measuring samples that contain only a negligible amount of particles with mass $A=210$. These samples are called blanks.

In the following, “210 bin” and “209 bin” denote the selected area in a TOF-energy plot, for mass $A=210$ and $A=209$ in the 5+ charge state. “210 events” and “209 events” are the number of counts in this areas.

A histogram of a bismuth blank sample is shown in fig. 7.3, where the influence of ^{209}Bi on the $^{210\text{m}}\text{Bi}$ detection can be seen.

³A typical value is about 0.8 ns.

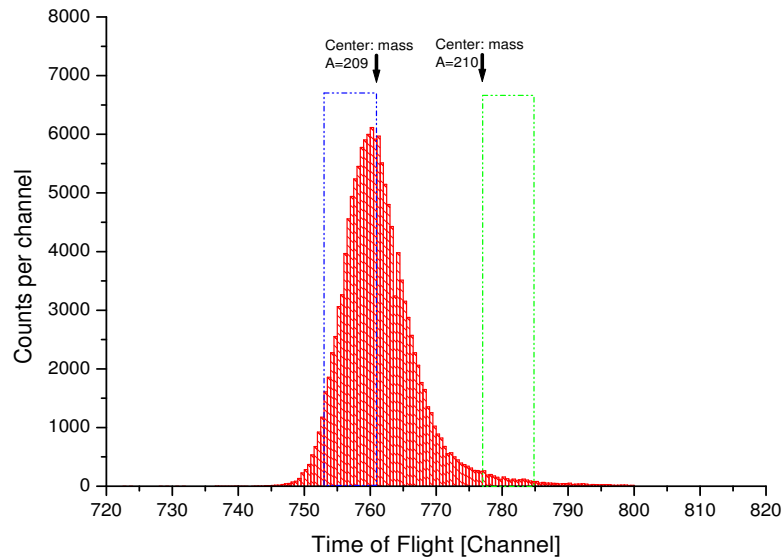


Figure 7.3: A TOF histogram of all blanks measured during a run series. The background produced by “209 events” in the “210 bin” (green marked area) can be seen.

As the number of “209 events” in the “210 bin” correlates with the number of “209 events” in the “209 bin”, it is possible to determine the correlation factor (linear fit of events in “bin 210” versus the events in “bin 209” , see fig. 7.4).

Another possibility for blank correction is to fit the shape of a histogram summed up for all blanks during a run series. The shape of the histogram, like in figure 7.3, is not a perfect Gaussian distribution, as it has a long tail right of the center.

With an exponential fit through the “210 bin” a background correction is possible (fig. 7.5).

The number of counts in the “210 bin” caused by “209 events” (N_{cor}) can be determined by calculating the defined integral of the exponential fit (equation 7.4). The integral limits (ChI, ChII) are the same as the bin settings. y_0 , x_0 , A and t are fit parameters.

$$N_{cor} = \int y_0 + A \cdot e^{-(x-x_0)/t} = y_0 x - At \cdot e^{(x_0-x)/t} \Big|_{ChI}^{ChII} \quad (7.4)$$

The counts (N_{cor}) have to be set in a relation to the number of “209 events” in the “209 bin” for background correction.

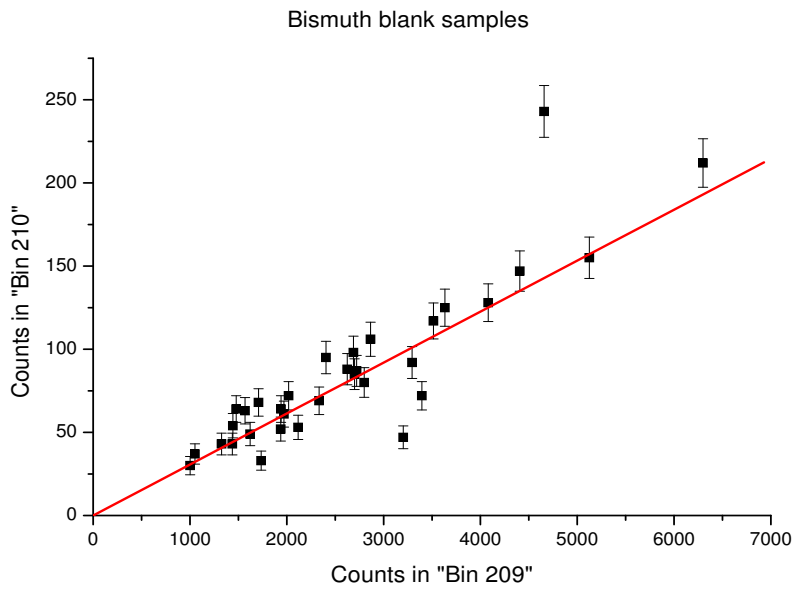


Figure 7.4: Events with $A=210$ related to events with $A=209$ by linear fitting. The error bars represent statistical uncertainties.

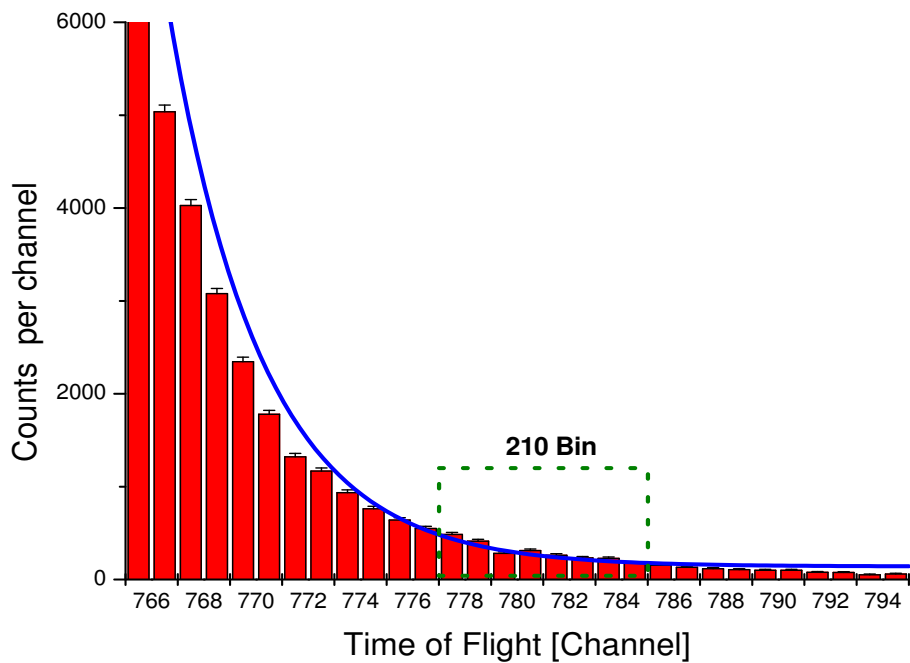


Figure 7.5: Exponential fit through the tail of the nearly Gaussian distributed histogram (see fig. 7.3).

7.4 Efficiency determination

The total efficiency of a $^{210\text{m}}\text{Bi}$ measurement with AMS consists of the charge-state-yield as mentioned above, the negative ion formation probability and the so-called high-energy-transmission.

7.4.1 Negative ion formation probability

The negative ion formation probability describes the fraction of nuclei that form negative ions in the source. To determine the negative ion formation probability a sample with known mass is sputtered and the current is measured continuously in a Faraday cup.

The fraction of particles that form negative ions (N_s) can be calculated from equation 7.5. In this equation I_j is an average current measured during a time period T_j and e is the elementary charge ($=1.602 \cdot 10^{-19}$ C). The measurement continues for M periods. The current is measured in a Faraday cup at the low energy-side.

$$N_s = \frac{\sum_j^M I_j \cdot T_j}{e} \quad (7.5)$$

The ratio of the particles that form negative ions in the source (N_s) to all particles in the sample (N_0) is the negative ion formation probability ($\epsilon_{negIon} = N_s/N_0$).

To correct for the ^{210}Po contribution in the measured isotope ratio $(^{210}\text{Po}+^{210}\text{Bi})/^{209}\text{Bi}$, the ratio between the negative ion formation probability of bismuth and polonium has to be determined, because a difference in the efficiency results in different absolute values for the isotopic ratio. This ratio is denoted as polonium scaling factor (ζ) and is defined by equation 7.6. The negative ion formation probability of bismuth was determined by $^{209}\text{Bi}^-$ current measurements. It is assumed that the difference of the negative ion formation probability of ^{209}Bi compared to $^{210\text{m}}\text{Bi}$ is negligible.

$$\zeta = \frac{\epsilon_{negIon}(^{210}\text{Po})}{\epsilon_{negIon}(^{209}\text{Bi})} \quad (7.6)$$

As the ^{210}Po beam is too weak to allow current measurements, the negative ion formation probability of ^{210}Po has to be determined by particle detection in the TOF detector. ^{210}Po sputter samples were produced from the chemically pretreatment (see chapter 7.5.2) as ^{210}Po

precipitates on silver. A certain amount of silver was utilised as sputter sample. The activity of the sample was measured via LSC by Gabriele Wallner. From the measured activity the number of ^{210}Po nuclei in the sample was calculated.

To compare the negative ion formation probability of ^{210}Po and ^{209}Bi the losses between FC04 and the ionisation chamber at the end of the heavy ion beam line have to be known (see next chapter).

7.4.2 “High-energy-transmission”

The high-energy-transmission includes the particle transmission from FC04 where the $^{209}\text{Bi}^{5+}$ current is measured to the ionisation chamber where $^{210\text{m}}\text{Bi}$ is detected, and also the fraction of particles within the area of interest in the “210 bin”. This includes also the efficiency of start and stop detector in the TOF system. Due to scattering effects less than 50% of the particles that pass the start detector are detected in the Bragg detector. Another part of the high-energy-transmission is caused by the influence of events with $A=209$ on the area in the TOF-energy plot where $A=210$ is expected. For this reason a bin was set and only approximately 40% of the detected events were selected for further evaluation.

The high-energy-transmission decreases by narrowing slits L5-1 and L4 (see fig. 7.1). This was done in some beam-times to further reduce background originating from ^{209}Bi .

The high-energy-transmission was determined by measuring the sum of the cross-section of $^{209}\text{Bi}(n, \gamma)^{210\text{g}}\text{Bi}$ and $^{209}\text{Bi}(n, \gamma)^{210\text{m}}\text{Bi}$. As shown in chapter 1.1, this neutron capture cross-section is rather well known. According to [5], the cross-section of $^{209}\text{Bi}(n, \gamma)^{210(\text{g+m})}\text{Bi}$ is 33.8 mbarn for thermal neutrons.

The high-energy-transmission (ϵ_{HE}) is then calculated by equation 7.7, where ^{210}Bi denotes $^{210(\text{g+m})}\text{Bi}$.

$$\epsilon_{HE} = \frac{N_{^{210}\text{Bi}}}{N_{^{209}\text{Bi}}} \cdot \frac{1}{\Phi \cdot \sigma(E_n)} \quad (7.7)$$

To measure $^{210(\text{g+m})}\text{Bi}$ it is necessary to perform neutron irradiations (at the Atominstitut) right before the AMS measurement, because $^{210\text{g}}\text{Bi}$ decays to ^{210}Po rather quickly with a half-life of 5.013 days. ^{210}Po has a higher negative ion formation probability. It is not possible to measure

directly after the neutron irradiation for practical reasons⁴. Therefore, the originally $^{210}\text{Bi}/^{209}\text{Bi}$ isotope ratio (i.e. after the irradiation) have to be recalculated by equation 7.8. In equation 7.8 the exponential decay of ^{210}gBi and the simultaneous growth of ^{210}Po , scaled by the polonium scale factor ζ , is considered for the expected isotope ratio. The intersection of this equation with $t=0$ gives the high-energy-transmission. Decay of ^{210}Po and of ^{210}gBi during neutron irradiation is negligible in equation 7.8 (discussed in more details in chapter 8.2.2).

$$\frac{210}{209}\Big|_{meas} = \underbrace{\frac{210}{209}\Big|_{calc}}_{=\sigma_{(g+m)}\cdot\Phi} \cdot \left[e^{-\lambda_{210gBi}t} + \zeta(1 - e^{-\lambda_{210gBi}t}) \right] \quad (7.8)$$

7.5 Polonium separation

Measuring the $^{209}\text{Bi}(n, \gamma)^{210m}\text{Bi}$ cross-section requires a sample without polonium, because the isobar ^{210}Po cannot be separated from ^{210m}Bi or ^{210g}Bi by AMS. As shown in chapter 1, ^{210g}Bi decays to ^{210}Po via β -decay with an half-life of 5.013 days. The half-life of ^{210}Po is 138.38 days. Due to the higher negative ion formation probability of polonium (as discussed in chapter 8.2.3), compared to bismuth, the ^{210}Po fraction in the sample influences the ^{210m}Bi AMS measurements for more than two years after neutron irradiation.

7.5.1 Polonium correction

Thus, one way is to wait for several years after neutron irradiation before performing AMS measurements. This would ensure that all ^{210}Po has decayed to ^{206}Pb (see fig. 1.1). If the polonium scale factor is not known the waiting time between neutron irradiation and AMS measurement is hard to define. In a first AMS measurement C. Stan-Sion et al. [4] for example, decided to carry out the measurements 1.9, 2.5 and 3.5 years after the irradiation.

If the polonium scaling factor and the $^{209}\text{Bi}(n, \gamma)^{210g}\text{Bi}$ cross-section are known, it is possible to correct the $^{210}\text{X}/^{209}\text{Bi}$ isotope ratio of bismuth samples where ^{210}Po still influences the

⁴The irradiated sample material has to be transported from the Atominstitut to the VERA facility (distance=8 km)

measurement (equation 7.9).

$$\left. \frac{^{210}\text{X}}{^{209}\text{Bi}} \right|_{\text{meas}} = \Phi \cdot (\sigma_m + \sigma_g) = \underbrace{\frac{^{210\text{m}}\text{Bi}}{^{209}\text{Bi}}}_{\text{"const"}} + \zeta \cdot \frac{^{210}\text{Po}}{^{209}\text{Bi}} \quad (7.9)$$

^{210}X denotes the sum of $^{210\text{m}}\text{Bi}$, $^{210\text{g}}\text{Bi}$ and ^{210}Po . The measured $^{210}\text{X}/^{209}\text{Bi}$ ratio is split into a bismuth and a polonium fraction. σ_m is the cross-section of $^{209}\text{Bi}(n, \gamma)^{210\text{m}}\text{Bi}$ and σ_g is the cross-section of $^{209}\text{Bi}(n, \gamma)^{210\text{g}}\text{Bi}$. In equation 7.9 it is assumed that all $^{210\text{g}}\text{Bi}$ decayed to ^{210}Po at the time of the AMS measurement. The $^{210\text{m}}\text{Bi}/^{209}\text{Bi}$ term is almost a constant due to the long half-life of $^{210\text{m}}\text{Bi}$ ($3.04 \cdot 10^6$ y). The ^{210}Po fraction, however, decays with a half-life of 138.38 days. Due to the higher negative ion formation probability of polonium (discussed in chapter 8.2.3), the polonium scale factor ζ has to be considered. The ^{210}Po fraction (ξ), of events with $A=210$ in the detector, can be calculated from equation 7.10.

$$\xi = \frac{\zeta \cdot \sigma_g \cdot \Phi \cdot e^{-\lambda_{210\text{Po}} \cdot t_w}}{\Phi \cdot (\sigma_m + \zeta \cdot \sigma_g \cdot e^{-\lambda_{210\text{Po}} \cdot t_w})} \quad (7.10)$$

7.5.2 Chemical pretreatment

Another way to handle the polonium interference is to separate it chemically. This procedure was accomplished by Gabriele Wallner.

To separate the ^{210}Po fraction from bismuth, samples irradiated with neutrons were dissolved in HNO_3 and the solution was evaporated to dryness; nitrous gases vapourised and bismuth nitrates remained. The precipitate was dissolved in 1 ml concentrated HCl and evaporated to dryness. This procedure was performed twice and bismuth chlorides remained. This precipitate was dissolved in 4 ml HCl mixed with 56 ml H_2O . Then a silver disk was added. The solution was stirred at 80-90 °C and the polonium precipitated at the silver disk. The silver disk was changed after two hours and the stirring process was repeated for another two hours.

7.6 Reference samples

For bismuth samples irradiated less than 300 days before the AMS measurements, the ^{210}Po fraction of particles with mass $A=210$ is at least 30%. With an estimated polonium scale factor

ζ of 15^5 , 80% of the detected events in the ionisation chamber at mass $A=210$ are originating from ^{210}Po (see fig. 7.6). Such samples, where ^{210}Po was not separated chemically, were always measured during a bismuth beam-time. These samples simplified identification of the area of interest and the center where events with $A=210$ were expected in the TOF-energy plot (fig. 7.6).

Due to different tuning setups, the transmission changed between beam-times and so neutron irradiated samples with a high ^{210}Po fraction were used as reference samples as well.

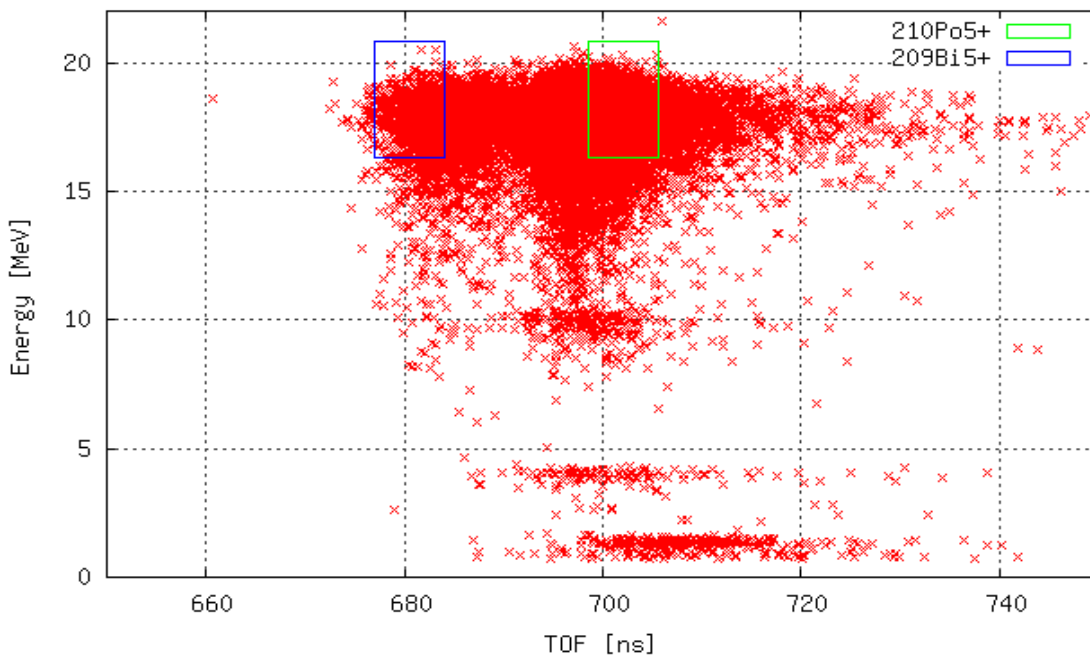


Figure 7.6: TOF spectrum of a bismuth sample, 236 days after the neutron irradiation ($T_{irr}=310\text{min}$). 30% of the total number of ^{210}Po have not decayed to ^{206}Pb . Considering a polonium scale factor of $\zeta=15$, 80% of the detected events at mass $A=210$ (green area) are ^{210}Po .

⁵In chapter 8.2.3 a polonium scale factor of 15 ± 3 is calculated.

8 Results

8.1 Cross-section of $^{209}\text{Bi}(n,\gamma)^{210\text{g}}\text{Bi}$ at thermal energies

Table 8.1 shows the results of the cross-section measurements of $^{209}\text{Bi}(n,\gamma)^{210\text{g}}\text{Bi}$ at thermal energies. As discussed in chapter 5 the epithermal fraction of the neutron spectrum at the irradiation position at the Atominstitut is about 1-2%.

The equations used to calculate the neutron capture cross-section are described in chapter 4.1. A_M is the activity of the bismuth samples, measured with LSC. The uncertainty of the LSC measurement is assumed to be 3% [56]. With the waiting time T_w (time between neutron irradiation and LSC measurement) the activity at the end of irradiation ($A_{t=0}$) can be calculated. The data of table 8.1 result in a mean value of **(16.9 ± 1.0) mbarn**.

Date of LSC Meas.	Sample	A_M [Bq/g]	T_w [d]	$A_{t=0}$ [Bq/g]	$^{210}\text{Bi}/^{209}\text{Bi}$ $\cdot(10^{-11})$	$\Phi \cdot (10^{15})$ [n cm ⁻²]	cross section [mbarn]
10.6.08	Bi-14	16500 ± 495	75.3	24070	14.4 ± 0.4	8.20 ± 0.40	17.6 ± 1.0
22.10.08	Bi-14	8290 ± 249	209.3	23640	14.2 ± 0.4	8.20 ± 0.40	17.3 ± 1.0
22.10.08	Bi-16	7530 ± 226	209.3	21490	12.9 ± 0.4	7.60 ± 0.30	16.9 ± 0.8
22.10.08	Bi-18	2260 ± 68	124.6	4210	2.52 ± 0.08	1.47 ± 0.07	17.1 ± 1.0
22.10.08	Bi-19	2160 ± 65	124.6	4030	2.41 ± 0.07	1.56 ± 0.08	15.5 ± 0.9

Table 8.1: Measured cross-section of $^{209}\text{Bi}(n,\gamma)^{210\text{g}}\text{Bi}$. The $^{210\text{g}}\text{Bi}/^{209}\text{Bi}$ isotope ratio is calculated from the specific sample activity A_M , measured by Gabriele Wallner with LSC.

8.2 Efficiency

8.2.1 Negative ion formation probability

The negative ion formation probability of ^{209}Bi was measured during beam-times Bi_ng9, Bi_ng10 and Bi_ng11. The amount of the sputtered material was about 1 mg, except for

sample Bi_S1 (7.20 mg). Table 8.2 presents all samples that were sputtered. The first three sputter samples were pure ^{209}Bi . The further samples were mixed with different amounts of silver. Obviously the silver fraction in the bismuth samples had no effects on the negative ion formation probability of ^{209}Bi . This is important to know, as samples mixed with silver as well as pure bismuth samples were measured in this thesis.

The calculation of the number of all particles in a sample (N_0) and the number of particles that form negative ions (N_s) is described in chapter 7.4.

The typical time development of the current from a bismuth sample containing silver is shown in fig. 8.1. The current is measured in the offset Faraday cup after the injection magnet. The data from the sputter samples result in a negative ion formation probability of about $1 \cdot 10^{-3}$. (see tab. 8.2).

Fig. 8.1 for a 1 mg sample has to be compared to the time development of a bismuth blank (pure ^{209}Bi powder) with a mass of about 10 mg as shown in fig. 8.2. The current of this sample at the beginning of the sputter process is four times higher compared to the value of samples with 1 mg. Therefore, it is not guaranteed that the efficiency measured for 1 mg samples is as high as for 10 mg, typically masses used for cross-section measurements. This might be the reason for the higher negative ion formation probability of Bi_S1 (7.2 mg). However, further investigations have to be made to pave that statement.

Name	Bi [mg]	Ag [mg]	N_0 $\cdot 10^{18}$	N_s $\cdot 10^{15}$	$\epsilon_{neg.Ion}$ $\cdot 10^{-3}$	T_M [h]
Bi_S1	7.20	0	20.75	43.23	2.1	9.9
Bi_S3	1.40	0	4.03	3.36	0.8	5.7
Bi_S4	0.77	0	2.22	2.23	1.0	3.0
Bi_S7	0.63	0.61	1.82	2.05	1.1	4.8
Bi_S9	0.68	0.28	1.96	2.01	1.0	3.4
Bi_S11	0.64	0.70	1.84	1.97	1.1	3.6
Bi_S12	0.43	0.76	1.24	1.15	0.9	4.8

Table 8.2: Bismuth samples of different mass and silver mixture were sputtered to measure the negative ion formation probability of bismuth at VERA. T_M is the time the sample was sputtered.

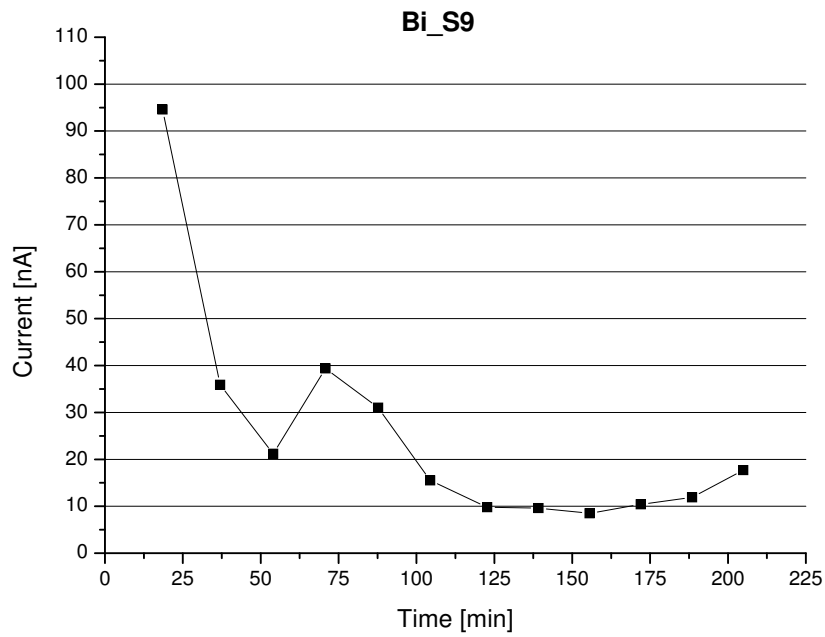


Figure 8.1: Mean current values of bismuth sample Bi_S9 (0.68 mg ^{209}Bi and 0.28 mg silver).

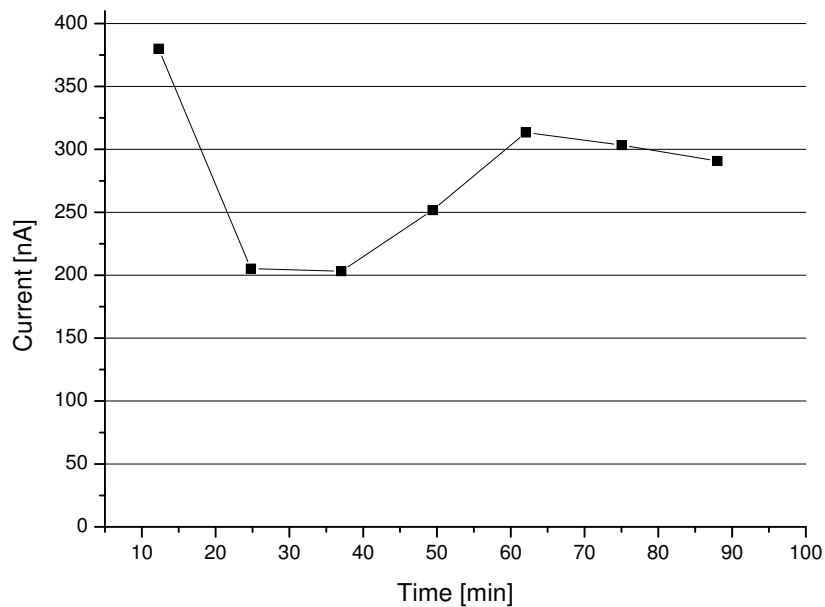


Figure 8.2: Mean current values of a bismuth blank (pure ^{209}Bi) with a mass of about 10 mg. At $t=35$ min the ion source setup was changed which resulted in a higher current.

8 Results

^{210}Po samples were also sputtered during beam-time Bi_ng10. Sample Po_1 and Po_2 were measured with the same tuning setup. Po_3 was measured with a different setup after a new target wheel was mounted.

Table 8.3 shows the results of ^{210}Po sputtering. The activity is calculated for the time of sputtering. As mentioned in chapter 7.4, the beam losses at the high-energy-side have to be considered to compare the negative ion formation probability of bismuth and polonium. The poor accuracy of the high-energy-transmission will be discussed in the following chapters. Therefore, only the overall efficiency (ϵ) for polonium is listed in table 8.3. The overall efficiency is the efficiency along the whole beam path, i.e. from the source to the Bragg chamber.

^{210}Po sputter samples contained only silver and ^{210}Po . Background in the TOF-energy plot from ^{209}Bi was therefore negligible. Thus an area (bin) can be chosen to cover nearly all ^{210}Po events in the TOF-energy plot. The difference between the events counted in this bin (denoted as "total bin" in table 8.3) and in "210 bin" used for $^{210\text{m}}\text{Bi}$ detection in other measurements gives the number of cut-off events.

The overall efficiency (ϵ) in table 8.3 refers to the "total bin". Further, it has to be mentioned that the slit openings of SLT03 (see fig. 7.1) were changed for measuring Po_3 (i.e. a different measurement setup was used). Therefore, the overall efficiency of Po_3 is higher. About 55% of the detected events with mass of $A=210$ are cut off by using a narrow "210 bin" (in order to minimise background from ^{209}Bi).

Name	Activity [Bq]	SLT03	$N_0 \cdot 10^8$	N_s 210Bin	N_s total Bin	Bin cut off [%]	$\epsilon \cdot 10^{-4}$
Po_1	8.3	5 mm	1.44	992	2452	59.5	0.17
Po_2	11.8	5 mm	2.04	2407	5146	53.2	0.25
Po_3	14.9	11 mm	2.58	21683	49170	55.9	1.91

Table 8.3: Results of ^{210}Po sputter samples. Po_3 was measured with a different setup.

8.2.2 Beam losses at the high-energy-side

To determine the high-energy-transmission two bismuth samples were irradiated for 73 minutes with a neutron flux of $3.1 \cdot 10^{11}$ and $3.3 \cdot 10^{11} \text{ n cm}^{-2} \text{ s}^{-1}$ at the Atominstitut. After the neutron irradiation, the samples were immediately brought to VERA. A new target wheel with two cathodes from each of the two samples was mounted. The AMS measurement of beam-time

Bi_ng10 started 4.5 hours after the sample irradiation was stopped.

In figure 8.3 and 8.4 the time-development of the measured $(^{210(g+m)}\text{Bi}+^{210}\text{Po})/^{209}\text{Bi}$ isotope ratio of both samples is shown. As polonium has a higher negative ion formation probability compared to bismuth, the events with $A=210$ detected in the TOF-system increased with the decay of ^{210g}Bi to ^{210}Po . A fit, shown in equation 7.8, was used to extrapolate the $^{210(g+m)}\text{Bi}/^{209}\text{Bi}$ isotope ratio at the time when the neutron irradiation was stopped ($t=0$ in those figures). Table

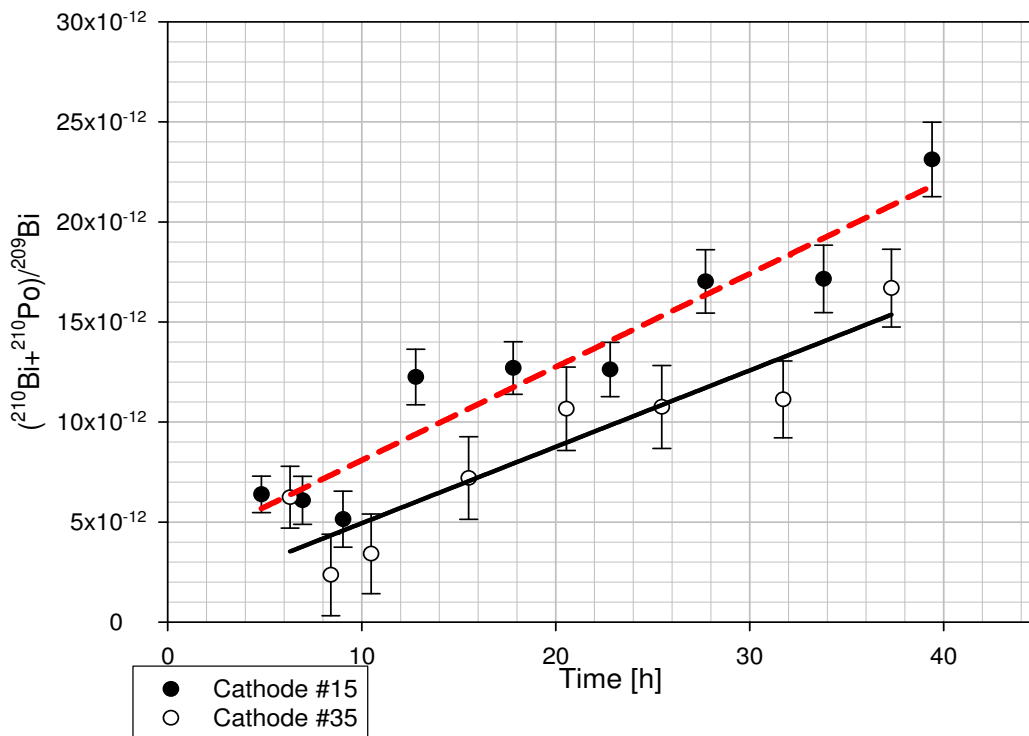


Figure 8.3: Freshly irradiated Bi sample Bi_TabA (2nd run series of Bi_ng10). The $(^{210}\text{Bi}+^{210}\text{Po})/^{209}\text{Bi}$ isotope ratio increases with the progressive decay of ^{210g}Bi to ^{210}Po due to the higher negative ion formation probability of ^{210}Po .

8.4 shows the $^{210(g+m)}\text{Bi}/^{209}\text{Bi}$ isotope ratio for $t=0$ and the resulting high-energy-transmission (ϵ_{HE}) according to equation 8.1. At $t=0$ only a negligible amount of ^{210}Po exists. According to equation 5.8 only 0.5% of ^{210g}Bi decays to ^{210}Po during a two hour neutron irradiation. This is an acceptable value because systematic uncertainties are much higher for bismuth measurements.

$$\epsilon_{HE} = \frac{210}{209} \cdot \frac{1}{\Phi \cdot \sigma_{(g+m)}} \quad (8.1)$$

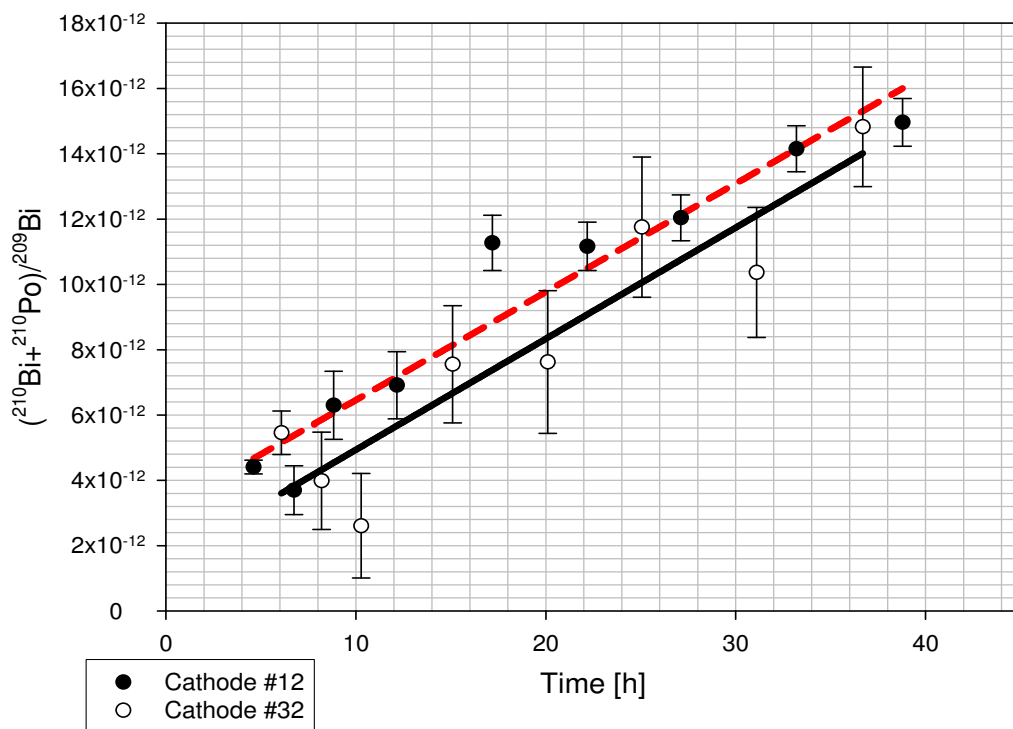


Figure 8.4: Freshly irradiated Bi Sample Bi_22 (2^{nd} run series of Bi_ng10). The $(^{210}\text{Bi}+^{210}\text{Po})/^{209}\text{Bi}$ isotope ratio increases with the decay of ^{210}gBi to ^{210}Po due to the higher negative ion formation probability of ^{210}Po .

The cross-section ($\sigma_{(g+m)}$) of $^{209}\text{Bi}(n, \gamma)^{210(g+m)}\text{Bi}$ was assumed to be 33.8 mbarn according to [5]. The neutron fluence (Φ) of the samples are listed in table 5.5.

Sample	Cat	$\frac{^{210}}{^{209}} _{t=0}$	ϵ_{HE} [%]
Bi_22	12	$3.1 \cdot 10^{-12}$	6.9
Bi_22	32	$1.5 \cdot 10^{-12}$	3.4
Bi_TabA	15	$3.4 \cdot 10^{-12}$	7.1
Bi_TabA	35	$1.1 \cdot 10^{-12}$	2.3

Table 8.4: Results of the high-energy-transmission measurements with freshly irradiated bismuth samples

The results shown in table 8.4 indicate a high systematic uncertainty. The high-energy-transmission calculated for cathode 12 (Bi_22) agrees with cathode 15 (Bi_TabA) and cathode 32 (Bi_22) agrees with cathode 35 (Bi_TabA). But there is a difference by a factor of two between cathode 12 and cathode 32 and also between cathode 15 and cathode 35. The sample in cathode 12 and 15 contained pure bismuth without silver, while the samples in cathode 32 and 35 contained a bismuth silver mixture. However, the negative ion formation probability (see chapter 8.2.1) showed that the silver fraction in a bismuth sample is not crucial for the efficiency. Due to the high scatter of these results, the high-energy-transmission during this beam-time could only be determined with large error (5 ± 2)%.

Due to the high systematic uncertainty of the high-energy-transmission measured during beam-time Bi_ng10, the procedure was repeated in April 2009 during beam-time Bi_ng12. Bismuth samples Bi_TabB and Bi_TabC were irradiated with thermal neutrons. Both samples were pressed to pellets. The samples could be measured with AMS at VERA 4.5 hours after the neutron irradiation was stopped.

The time development of the $(^{210(g+m)}\text{Bi} + ^{210}\text{Po})/^{209}\text{Bi}$ isotope ratio is shown by an example of Bi_TabB in fig. 8.5. Different sample cathodes are shown in different colours. Bi_TabC is very similar. In this figure the deviation between cathodes is smaller compared to beam-time Bi_ng10. Therefore, equation 7.8 is fitted through all data points obtained from a sample material. The calculated $^{210(g+m)}\text{Bi}/^{209}\text{Bi}$ isotope ratio for the time the neutron irradiation was stopped, and the calculated beam losses at the high-energy-side ϵ_{HE} (see equation 8.1) are

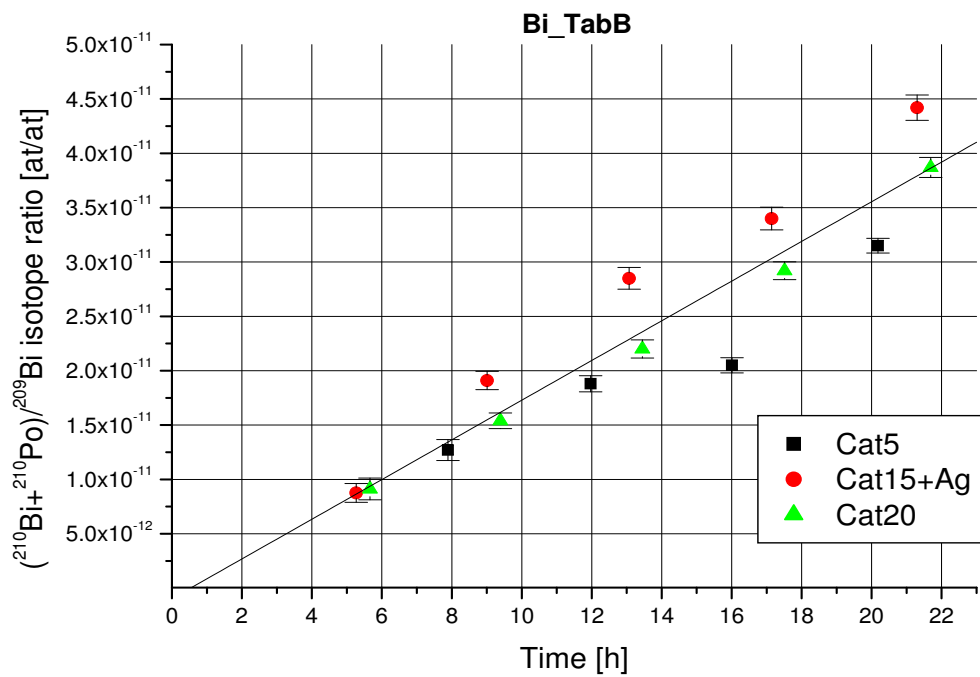


Figure 8.5: Freshly irradiated Bi Sample Bi_TabB during Bi_ng12. The $(^{210}\text{Bi}+^{210}\text{Po})/^{209}\text{Bi}$ isotope ratio increases with the decay of ^{210}gBi to ^{210}Po due to the higher negative ion formation probability of ^{210}Po . The error bars show only the statistically uncertainty.

listed in table 8.5. As the high-energy-transmission calculated with Bi_TabB is a negative value the procedure obviously failed and another evaluation has to be used.

Sample	Cat	$\frac{^{210}}{^{209}} _{t=0}$	ϵ_{HE} [%]
Bi_TabB	5,15,20	$-9.6 \cdot 10^{-13}$	neg. Value
Bi_TabC	10,25,30	$5.1 \cdot 10^{-12}$	6.4

Table 8.5: Results of the high-energy-transmission measurements with freshly irradiated samples

The area of interest in the TOF-energy plot was expanded to contain about two times more events with mass A=210. This area will be called “wide 210 bin” in the following. The time development of the isotope ratio $(^{210(g+m)}\text{Bi}+^{210}\text{Po})/^{209}\text{Bi}$ for “wide 210 bin” is shown in fig. 8.6 and 8.7. With equation 7.8 a $^{210(g+m)}\text{Bi}/^{209}\text{Bi}$ isotope ratio for t=0 and

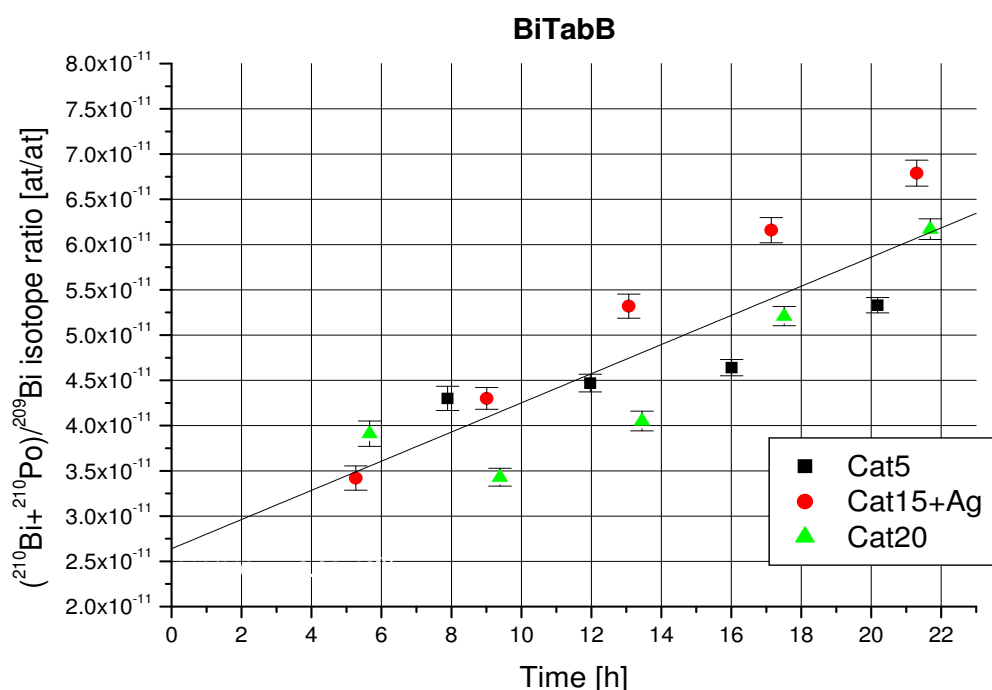


Figure 8.6: Freshly irradiated Bi Sample Bi_TabB during Bi_ng12. To evaluate the events with A=210 a larger bin was selected in the TOF-energy plot. The $(^{210}\text{Bi}+^{210}\text{Po})/^{209}\text{Bi}$ ratio increases with the decay of ^{210g}Bi to ^{210}Po due to the higher negative ion formation probability of ^{210}Po . The error bars show only the statistically uncertainty.

a high-energy-transmission can be calculated. These values are listed in table 8.6. When

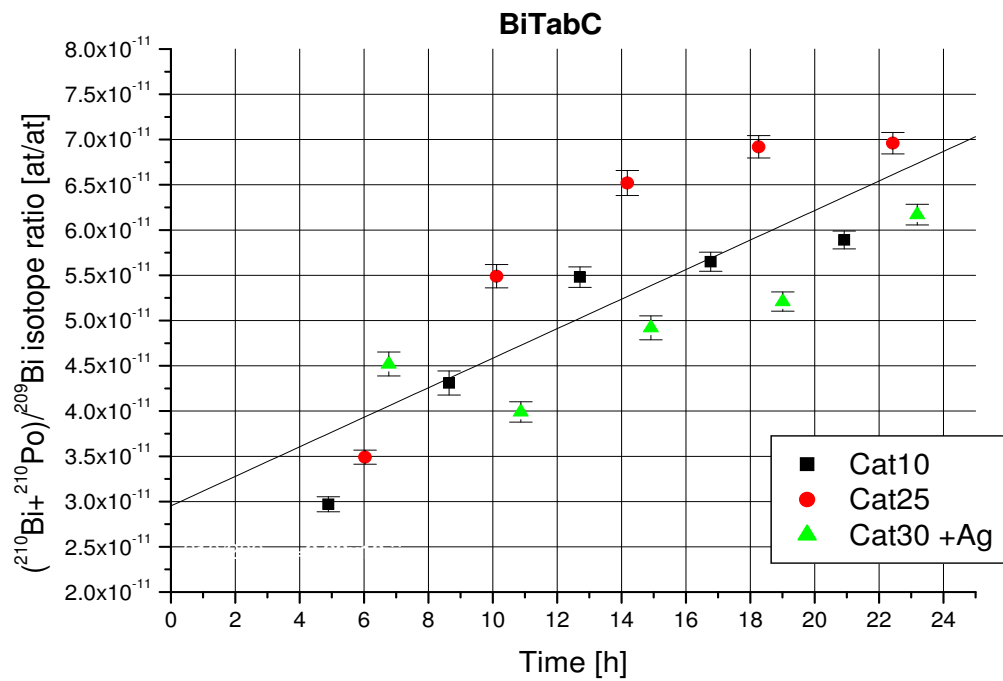


Figure 8.7: Freshly irradiated Bi Sample Bi_TabC during Bi_ng12. To evaluate the events with $A=210$ a larger bin was selected in the TOF-energy plot. The $(^{210}\text{Bi} + ^{210}\text{Po})/^{209}\text{Bi}$ ratio increases with the decay of ^{210}gBi to ^{210}Po due to the higher negative ion formation probability of ^{210}Po . The error bars show only the statistically uncertainty.

calculating the fit parameters for each cathode separately the resulting isotopic ratio differ by about 35%. Thus, a systematic uncertainty of $\pm 17\%$ was assumed. Resulting in a high-energy-transmission during beam-time Bi_ng12 of $(34\pm 6)\%$, calculated with “wide 210 bin”.

Sample	Cat	$\frac{^{210}}{^{209}} _{t=0}$	ϵ_{HE} [%]
Bi_TabB	5,15,20	$2.6 \cdot 10^{-11}$	32
Bi_TabC	10,25,30	$2.9 \cdot 10^{-11}$	37

Table 8.6: Results of the high-energy-transmission measurements with fresh irradiated samples. The uncertainties of ϵ_{HE} are discussed in the text.

Wide bins were also used for re-evaluating the high-energy-transmission of bismuth sample Bi_22 and Bi_TabA (measured during Bi_ng10). However, the results gave the same behaviour as the results calculated with narrow bins.

For future bismuth measurements at VERA the high-energy-transmission has to be calculated with “wide 210 bin”. The problem with “wide 210 bin” is that background caused by ^{209}Bi increases.

But even with “wide 210 bin” the reproducibility is very poor, see the scatter of the individual data points in figure 8.6 or 8.7. The rather similar value of 32% and 37% seems to be more due to averaging and might by chance suggest a constant value. It appears that the AMS measurement of ^{210}Bi together with ^{210}Po cause this problem and therefore other possibilities to quantify the beam losses should be used (see chapter 9).

8.2.3 Polonium scale factor

With the value for the high-energy-transmission of $(34\pm 6)\%$, an estimation for the polonium scale factor (ζ) is possible (see chapter 7.4.1). During beam-time Bi_ng12 two samples with a high ^{210}Po fraction were measured (Bi_14 and Bi_16). Assuming that only a negligible amount of events at $A=210$ are produced by $^{210\text{m}}\text{Bi}$, the measured $^{210}\text{X}/^{209}\text{Bi}$ isotope ratio is approximately the $^{210}\text{Po}/^{209}\text{Bi}$ isotope ratio (an estimation for this assumption is shown in equation 8.4). ^{210}X denotes the sum of all isobars with $A=210$ that are detected in the Bragg chamber.

According to equation 8.2 the $^{210}\text{Po}/^{209}\text{Bi}$ isotope ratio is equal to the neutron fluence of

8 Results

the sample (Φ) multiplied by the cross-section of $^{209}\text{Bi}(n, \gamma)^{210\text{g}}\text{Bi}$ for thermal energies ($\sigma_{g,th}$) considering the exponential decay between neutron irradiation and AMS measurement (t_w).

$$\frac{^{210}\text{Po}}{^{209}\text{Bi}} = \Phi \cdot \sigma_{g,th} \cdot e^{-\lambda_{210\text{Po}} \cdot t_w} \quad (8.2)$$

Further, the high-energy-transmission (ϵ_{HE}) has to be considered to calculate the polonium scale factor (ζ) in equation 8.3. $^{210}\text{X}/^{209}\text{Bi}|_{meas}$ is the measured $^{210}\text{X}/^{209}\text{Bi}$ isotope ratio with AMS using the same “wide 210 bin” as for the transmission determination as for sample Bi_TabB and Bi_TabC.

$$\frac{\frac{^{210}\text{X}}{^{209}\text{Bi}}|_{meas}}{\frac{^{210}\text{Po}}{^{209}\text{Bi}}} \cdot \frac{1}{\epsilon_{HE}} = \zeta \quad (8.3)$$

Following equation 8.3 the polonium scale factor can be determined by means of the bismuth samples Bi_14 and Bi_16 as shown in table 8.7. The high-energy-transmission for this tuning setup was $(34 \pm 6)\%$.

This results in a mean value of ζ of 15 ± 3 . Polonium makes 15 times more likely negative ions in the ion source compared to bismuth. The uncertainties are given by the fluence, the

Sample name	$\frac{^{210}\text{X}}{^{209}\text{Bi}} _{meas} [\cdot 10^{-10}]$	$\frac{^{210}\text{Po}}{^{209}\text{Bi}} [\cdot 10^{-10}]$	ζ
Bi_14	0.90 ± 0.11	0.20 ± 0.02	13 ± 3
Bi_16	1.06 ± 0.07	0.19 ± 0.01	17 ± 3

Table 8.7: The polonium scale factor ζ calculated by means of samples Bi_14 and Bi_16 measured during beam-time Bi_ng12.

AMS measurement, by the cross-section value of $^{209}\text{Bi}(n, \gamma)^{210\text{g}}\text{Bi}$ (see chapter 8.1) and are dominated by the high-energy-transmission.

The fraction of $^{210\text{m}}\text{Bi}$ in the ^{210}X events of sample Bi_14 and Bi_16 can be estimated. Two samples (measured during Bi_ng10), which stem from the same irradiated material were compared. In one case ^{210}Po was efficiently removed by chemical extraction (denoted as *GW*) (see chapter 7.5.2), in the other case the metallic bismuth powder was directly pressed into a

sample holder (U_t). According to equation 8.4 the ^{210}Po fraction can be calculated.

$$\frac{^{210}\text{Po}}{^{209}\text{Bi}} = \frac{^{210}\text{X}}{^{209}\text{Bi}} \Big|_{U_t} - \frac{^{210\text{m}}\text{Bi}}{^{209}\text{Bi}} \Big|_{GW} \quad (8.4)$$

This results in a $^{210\text{m}}\text{Bi}$ fraction up to 7%. For the estimation of the polonium scale factor this fraction was taken into account.

8.3 Blanks

8.3.1 Linear blank correction

The background correction using a linear correlation between events with mass of $A=209$ in “209 bin” and events with $A=210$ in “210 bin” is described in chapter 7.3. The counts in “bin 209” are plotted against the counts in “bin 210”. A straight line passing the origin is fitted through these data points. This results in the linear blank correction factor k (fig. 8.8).

Figure 8.8 shows the blank correction fit for the 2nd run series of Bi_ng10 and figure 8.9 for the 3rd series of the same beam-time.

In figure 8.9 four data points are off the linear fit curve. Possible reasons for this behaviour, could be a wrong set of correction values for a sudden shifting of the TOF signal¹ or a bad current measurement. Both options were checked but led to no conclusion. The fact that these data points belong to three different samples excludes the possibility of a contamination with neutron irradiated bismuth. Further, the possibility that the measurement delivered bad data during a certain period of time can be excluded because these four runs were not measured consecutively. As defined by equation 8.5 the correction factors k of each run series are listed in table 8.8. $N(210)$ is the number of events in the “210 bin” and $N(209)$ the number of events in the “209 bin”.

$$N(210) = N(209) \cdot k \quad (8.5)$$

The background of events with $A=210$ can be corrected according to equation 8.6.

$$N(210)_{corr} = N(210) - N(209) \cdot k \quad (8.6)$$

Beam-time or Run Series	Correction- factor k
Bi_ng10 2nd Series	0.031
Bi_ng10 3rd Series	0.057

Table 8.8: Blank correction factors k according to equation 8.5

¹The TOF signal shifted during Bi_ng10. This had to be corrected by an offset value.

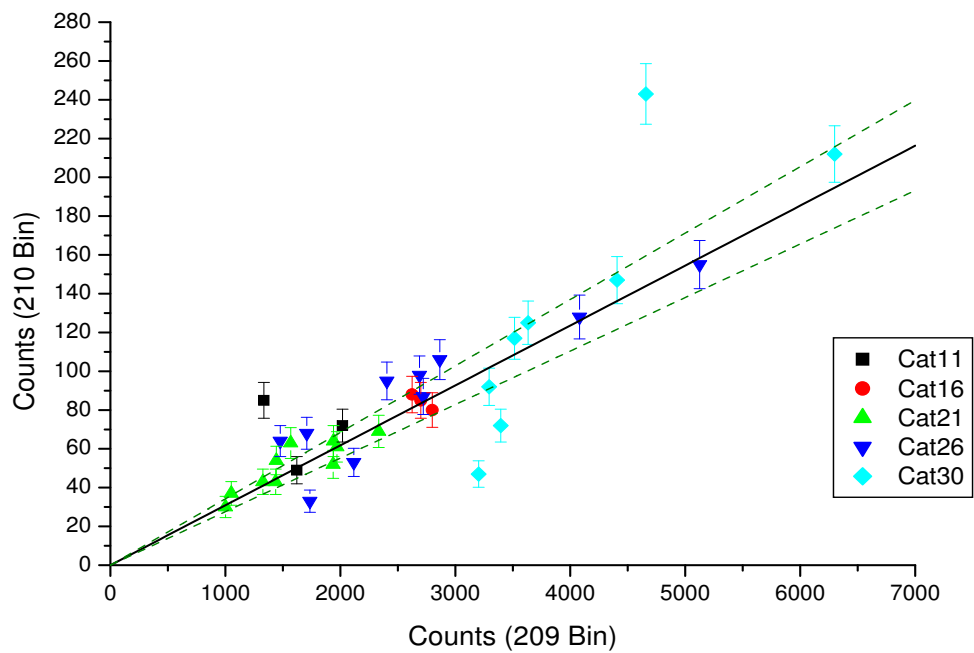


Figure 8.8: Linear blank correction for Bi_ng10, 2nd run series (blank samples are pure bismuth powder without any pretreatment). Different symbols (colours) denote different sample cathodes.

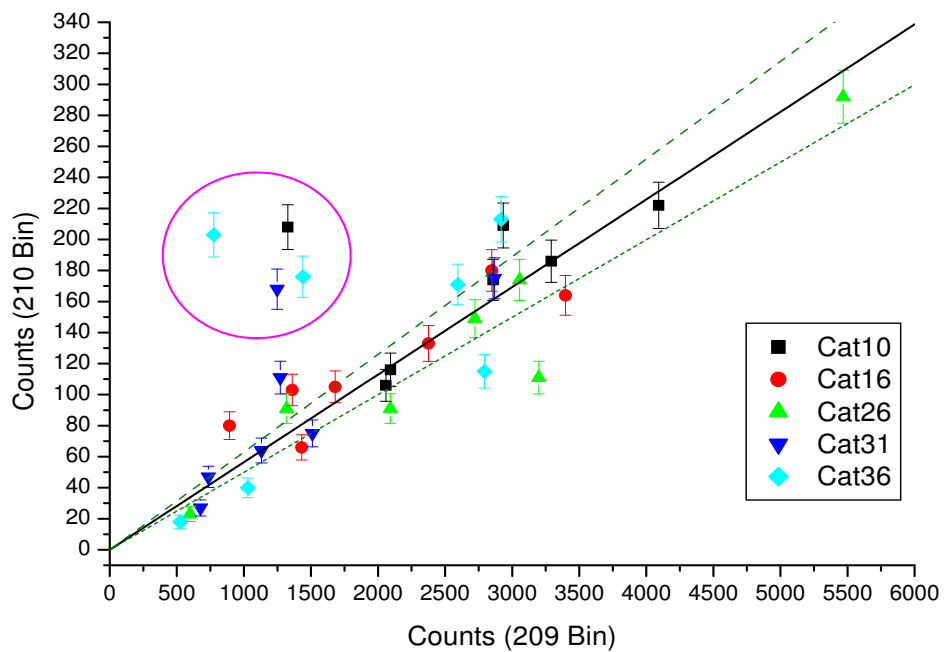


Figure 8.9: Linear blank correction for Bi_ng10 3rd run series (blank samples are pure bismuth powder without any pretreatment). Different symbols (colours) denote different sample cathodes. Data points in pink circle are discussed in the text.

Figure 8.10 shows the $^{210}\text{Bi}/^{209}\text{Bi}$ ratio of both, blank corrected bismuth and not corrected $^{210}\text{Bi}/^{209}\text{Bi}$ ratios. These samples were measured during the 2nd run series of Bi_ng10. The weighted mean value of all blank samples is $(2.9\pm 5.5)\cdot 10^{-14}$ (measured ratio).

For the absolute detection limit, which was defined as two times the standard deviation of the measured blank samples, the high-energy-transmission (measured during Bi_ng10) has to be considered ($(5\pm 2)\%$, chapter 8.2.2). Therefore, the detection limit of $^{210\text{m}}\text{Bi}/^{209}\text{Bi}$ measurements was $(1-4)\cdot 10^{-12}$ for the 2nd run series of Bi_ng10 at VERA. As the slit openings were changed for the third run series, the high-energy-transmission also changed. This resulted in a higher background (i.e. a higher correction factor) and a mean value of all blank samples of $(2.8\pm 1.2)\cdot 10^{-13}$ (measured ratio). A value for the high-energy-transmission of this measurement setup (i.e. 3rd run series of Bi_ng10) could not be determined.

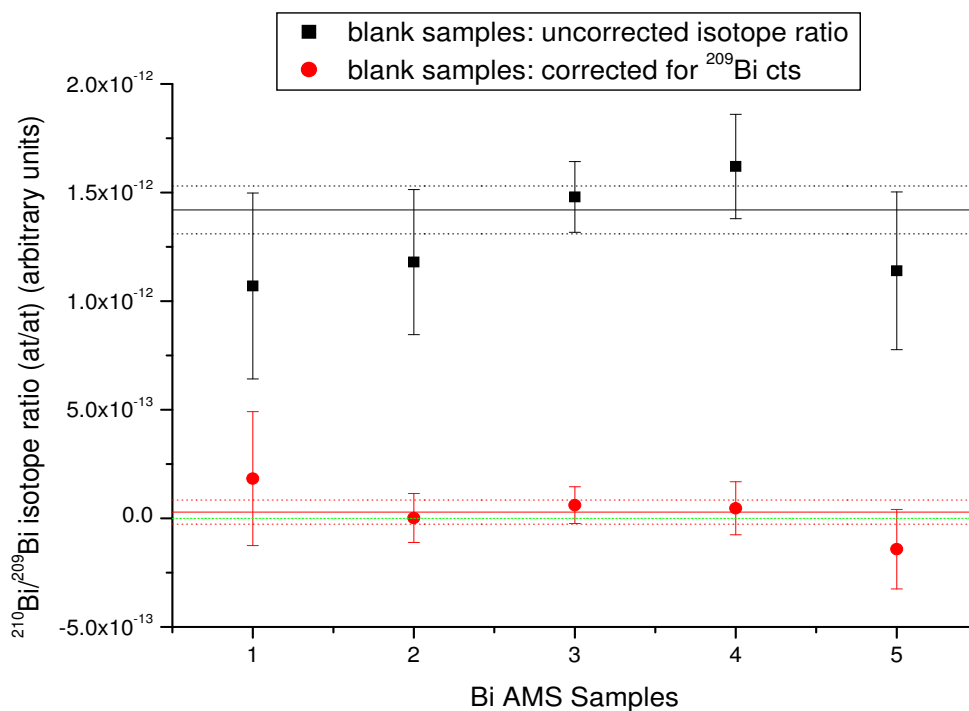


Figure 8.10: Blank samples measured during Bi_ng10 (2nd run series). Black data points denote raw ratios and red data points background-corrected ratios. The mean value of all background corrected ratios is $(2.9\pm 5.5)\cdot 10^{-14}$ not scaled with the high-energy-transmission.

8.3.2 Gaussian blank correction

Another possibility of background correction is to fit the shape of the histogram (see chapter 7.3). An exponential fit in the region of “bin 210” agrees with the blank histogram of the 2nd run series of Bi_ng10 (see figure 8.11). According to equation 8.7 the parameters of these fit are listed in table 8.9.

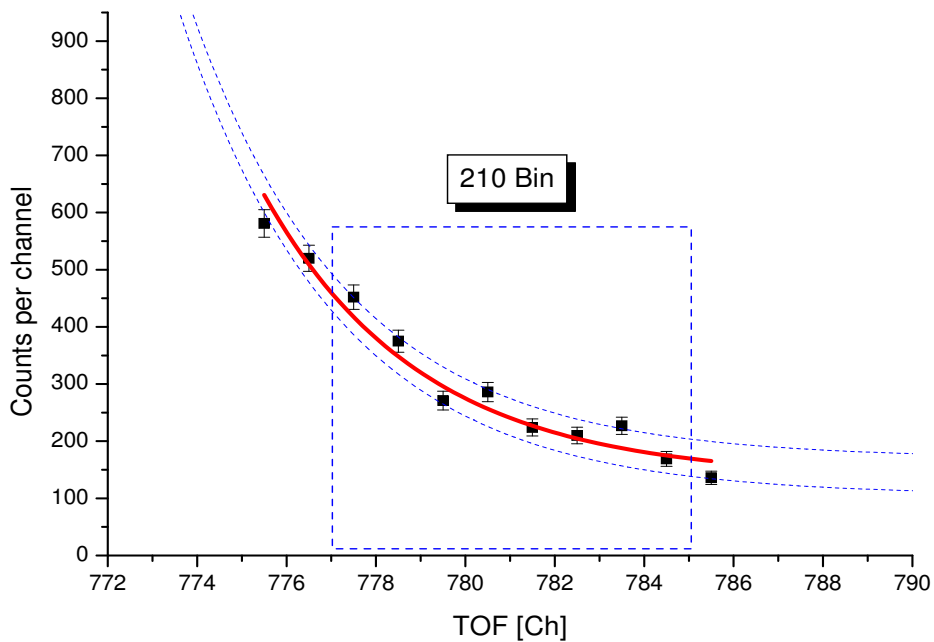


Figure 8.11: Exponential fit through the “210 bin” - measured blank histograms were summed (Bi_ng10 ,2nd run series).

$$y = y_0 + A \cdot e^{-(x-x_0)/t} \quad (8.7)$$

The number of background events ($\sum_i N(210)_i$) in the “210 bin” follows equation 8.8 and results in a total number of 3260 counts for this run series. The number of events in “bin 210” can now be corrected by $N_j(210)$ according to equation 8.9.

$$\sum_i N(210)_i = \int_{777}^{785} (y_0 + A \cdot e^{-(x-x_0)/t}) \quad (8.8)$$

Parameter	Value
y_0	118
A	882
x_0	775
t	5.12

Table 8.9: Parameters for exponential fit through the “210 bin” region

$$N_j(210) = \frac{\sum_i N(210)_i}{\sum_i N(209)_i} \cdot N(209)_j \quad (8.9)$$

In this equation $\sum_i N(210)_i$ is the number of events in “bin 210” (counts summed over all blanks) and $\sum_i N(209)_i$ the sum of all events in “bin 209”. $N(209)_j$ is the number of events in the “209 bin” of an individual run. This background correction results in a weighted (raw) mean value for bismuth samples of $(0.4 \pm 3.7) \cdot 10^{-14}$ (2nd run series of Bi_ng10). This is shown in fig. 8.12. This value agrees with the result applying the linear blank correction (chapter 8.3.1). The problem when using an exponential fit to correct the $^{210\text{m}}\text{Bi}/^{209}\text{Bi}$ ratios is that a slight change of the number of data points used for generating the fit results in a significant change of the fit parameters and the number of background events.

Therefore, the linear fit should be used, because the linear blank correction is more stable and more traceable.

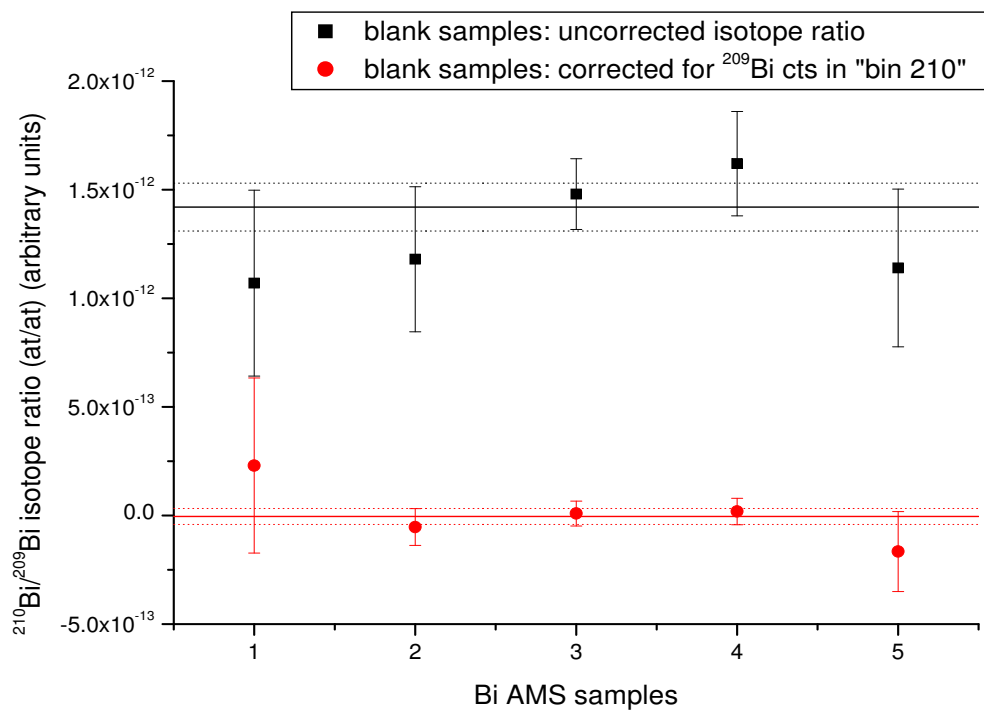


Figure 8.12: Blank sample measured during Bi_ng10 (2nd run series), background corrected with an exponential fit. Black data (squares) points denote raw ratios and red data points (circles) background corrected ratios, both in arbitrary units.

8.4 Polonium-free AMS samples

A value for the cross-section of $^{209}\text{Bi}(n, \gamma)^{210\text{m}}\text{Bi}$ from literature is used to check the variance of the measurement results during Bi_ng10 and Bi_ng12. The cross-section values by Borella et al. (2005) [13] and Stan-Sion et al. (2007) [4] were used. The results of these experiments give a mean value of (19.5 ± 1.8) mbarn for the thermal cross-section of $^{209}\text{Bi}(n, \gamma)^{210\text{m}}\text{Bi}$.

Using this cross-section and equation 8.10, the data in table 8.10 can be calculated. This table compares ^{210}Po free samples of different beam-times. Samples denoted with the prefix “GW” underwent a chemical pretreatment by Gabriele Wallner (see chapter 7.5.2) to remove the ^{210}Po fraction. For other samples a ^{210}Po correction had to be made. Therefore, a polonium scale factor (ζ) of 15 was assumed, as shown in chapter 8.2.3. The fraction of events for A=210, that are caused by ^{210}Po entering the detector is written in column “Po Cor” in table 8.10.

In table 8.10 the results and corresponding weighted mean values are listed and plotted in figure 8.13.

$$\epsilon_{HE} = \frac{^{210\text{m}}\text{Bi}}{^{209}\text{Bi}} \cdot \frac{1}{\Phi\sigma} \quad (8.10)$$

When calculating the high-energy-transmission by assuming a fixed cross-section value (taken

Beamtime run series	Sample @Cathode	$^{210}\text{Bi}/^{209}\text{Bi}$ ($\cdot 10^{-12}$)	Po Cor.	Φ [n cm^{-2}] ($\cdot 10^{15}$)	ϵ_{HE} [%]	mean Value ϵ_{HE} [%]
Ng10 (2)	GW14@7	6.0 ± 0.2		8.2 ± 0.4	3.7 ± 0.4	3.9 ± 0.3
	GW16@22	5.6 ± 0.3		7.6 ± 0.3	3.8 ± 0.4	
	GW14@27	6.7 ± 0.3		8.2 ± 0.4	4.2 ± 0.5	
Ng10 (3)	Bi3@5	15.5 ± 3.1	16 %	10 ± 1	6.7 ± 1.5	6.3 ± 0.6
	GW16@22	8.4 ± 1.6		7.6 ± 0.3	5.7 ± 1.2	
	Gw14@27	10.4 ± 1.0		8.2 ± 0.4	6.5 ± 0.9	
	Bi1@28	2.2 ± 0.4	10 %	1.6 ± 0.1	6.3 ± 1.2	
	Gw19@38	1.8 ± 0.5		1.56 ± 0.06	5.9 ± 1.8	
Ng7	GW1@5	2.1 ± 0.9		1.6 ± 0.1	6.8 ± 2.8	7.7 ± 0.7
	GW3@8	15.3 ± 0.7		10 ± 1	7.9 ± 0.9	
	Bi1@24	3.4 ± 0.5	33 %	1.6 ± 0.1	7.4 ± 1.3	
Ng6	Bi1@29	3.3 ± 0.5	58 %	1.6 ± 0.1	4.4 ± 0.8	4.4 ± 0.8

Table 8.10: Measured $^{210\text{m}}\text{Bi}/^{209}\text{Bi}$ isotope ratio for different samples and beam-times (run series). Different beam-times and run-series are independent due to the different tuning. Thus, the high-energy-transmission ϵ_{HE} is different between each tuning. ϵ_{HE} is calculated using a literature value for the cross-section of $^{209}\text{Bi}(n, \gamma)^{210\text{m}}\text{Bi}$ ([13] and [4]).

from [13] and [4]) the results do not vary as much as found in chapter 8.2.2. Figure 8.13 shows

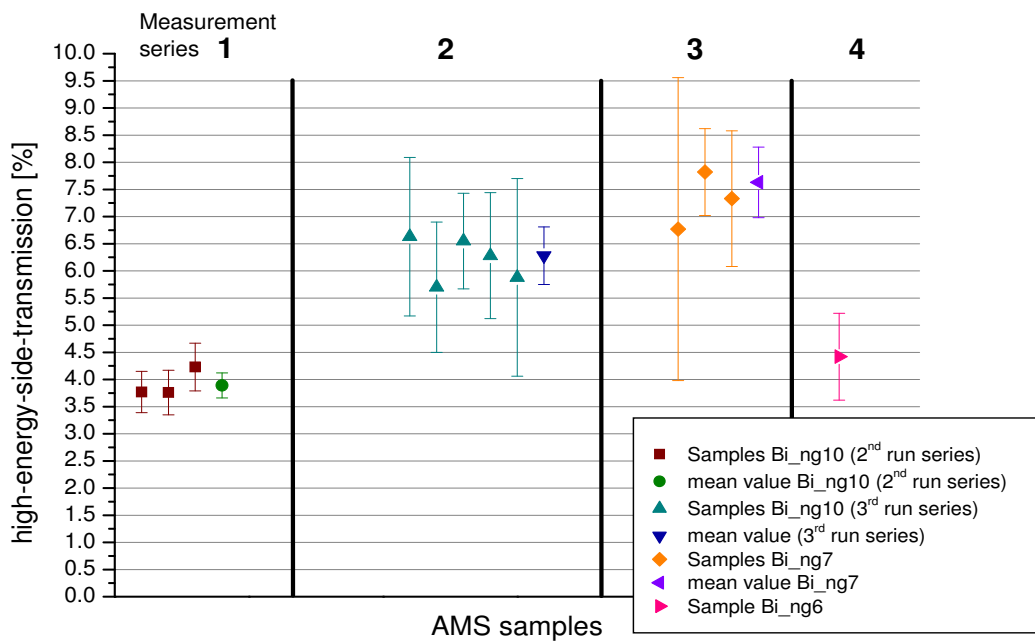


Figure 8.13: ^{210}Po -free samples measured during different beam-times (i.e. different tunings). Different tunings result in different transmission factors (i.e. different beam losses at the high-energy-side). ϵ_{HE} is calculated by using a fixed value for the cross-section of $^{209}\text{Bi}(n, \gamma)^{210\text{m}}\text{Bi}$ at thermal energies (σ), ([13] and [4]).

that it is possible to reduce the relative error to 6% for beam-time Bi_ng10 (2nd run series). The relative error increases in the 3rd run series of Bi_ng10 to 8%, but the transmission itself increased by a factor of 1.6. This is a consequence of changing the SLT03 openings from 5 mm to 11 mm. It is apparent that the uncertainty of the AMS measurement increases by using wider slit openings, because more particles with mass A=209 can pass the electrical and magnetic filters.

Data from Bi_ng7 vary in the same order of magnitude as data from Bi_ng10. The Bi_1 sample had a ²¹⁰Po fraction of 33% at that time, but the ²¹⁰Po correction worked for this relatively high ²¹⁰Po amount. These data show that ^{210m}Bi AMS measurements are feasible with a reproducibility of better than 10%. A high ²¹⁰Po content in the sample seems to cause higher uncertainties (see next chapter).

More beamtimes could not be utilised for this comparison, because either no ²¹⁰Po-free samples were measured (except for blanks) or the tuning could not be completed. In the very first beamtimes, no chemically pretreated samples were measured and the waiting time between measurement and irradiation was too short for a sufficient accurate ²¹⁰Po correction.

8.5 Reference samples

As mentioned in chapter 7.6 neutron irradiated samples that had no chemical pretreatment but a high ^{210}Po fraction in the sample were also measured during a beam-time. Their peak position for $A=210$ in the TOF histogram can be used for regular checks. As these samples deliver high count-rates, they can be taken as reference samples to check the tuning and the setup. The polonium scale factor was also determined with such samples (chapter 8.2.3). A scaling factor was determined to compare the second and third run series of beam-time Bi_ng10 (fig. 8.14). Based on the results of each reference sample, a weighted mean value was calculated for each run series. The results in table 8.11 were scaled to the neutron fluence of the respective irradiation.

These reference values (i.e. $^{210}\text{Bi}/^{209}\text{Bi} \cdot 1/\Phi$) are $(16 \pm 1) \cdot 10^{-27} \text{ cm}^2$ and $(23 \pm 2) \cdot 10^{-27} \text{ cm}^2$, respectively. They are proportional to a $(\sigma \cdot \epsilon_{HE})$ value.

This yields a scaling factor of (0.68 ± 0.08) between these run series. However, an error of about 12% is not acceptable to scale different measurement setups.

Sample@Cat	$^{210}\text{Bi}/^{209}\text{Bi}$ $\cdot 10^{-10}$	Φ $\cdot 10^{15}$	$^{210}\text{Bi}/^{209}\text{Bi} \cdot \frac{1}{\Phi}$ $\cdot 10^{-27}$
Bi_ng10 off4			
Bi14_1@3	1.3 ± 0.1	8.2 ± 0.4	16 ± 2
Bi16_1@17	1.3 ± 0.2	7.6 ± 0.3	17 ± 3
Bi14_2@23	1.1 ± 0.1	8.2 ± 0.4	14 ± 2
			16 ± 1
Bi_ng10 off3			
Bi14_3@3	1.7 ± 0.1	8.2 ± 0.4	21 ± 1
Bi16_2@17	2.0 ± 0.2	7.6 ± 0.3	26 ± 3
Bi14_3@23	2.3 ± 0.1	8.2 ± 0.4	28 ± 2
			23 ± 2

Table 8.11: Measurement results of untreated AMS samples without considering the high-energy-transmission. The values in the 4th column are proportional to a cross-section value.

Samples with a high ^{210}Po content vary up to 30% between individual runs. This supports the assumption that ^{210}Po (or the ^{210}Po - ^{210}Bi mixture) is a reason for the poor reproducibility .

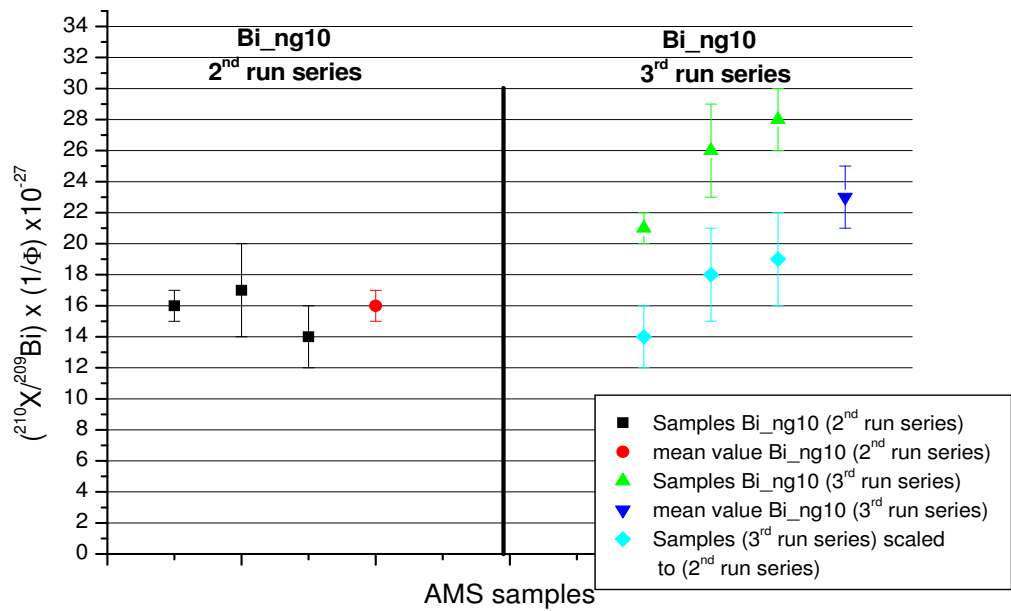


Figure 8.14: Accelerator setup of 2nd run series of Bi_ng10 compared to the 3rd run series.

8.6 AMS measurements for kT=25 keV-samples

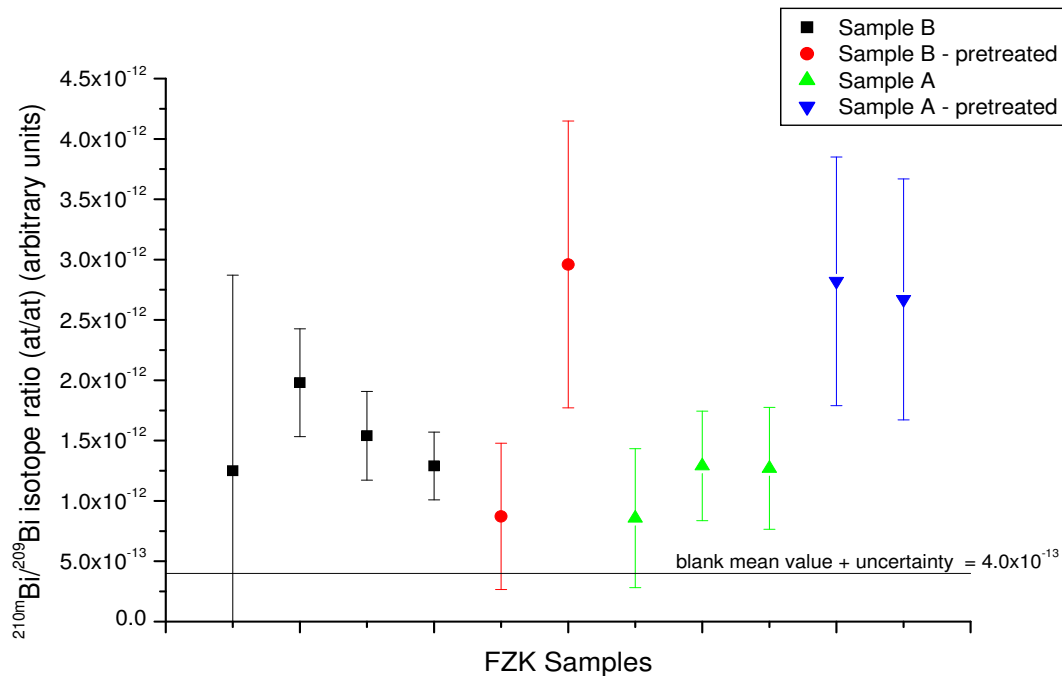


Figure 8.15: The $^{210\text{m}}\text{Bi}/^{209}\text{Bi}$ isotope ratio for samples irradiated with neutrons of kT=25 keV (Maxwellian energy distribution) compared to the mean value of blank samples (plus uncertainty) of this measurement series. The values are not scaled to beam losses at the high-energy-side.

An important task for this thesis was to explore, if $^{209}\text{Bi}(n, \gamma)^{210\text{m}}\text{Bi}$ cross-section measurements with AMS at VERA are possible for neutrons with a quasi-Maxwellian energy distribution of 25 keV.

Therefore, these measured isotope ratios of $^{210\text{m}}\text{Bi}/^{209}\text{Bi}$ are compared with the mean value of the blank samples (plus its uncertainty). In figure 8.15 this value is $4.0 \cdot 10^{-13}$ (for the third run series of Bi_ng10, discussed in chapter 8.3.1). Values in this figure are not normalised with the high energy transmission. It can be seen that all samples are significantly above the blank samples.

Both, samples with a chemical pretreatment to remove ^{210}Po were measured and samples without chemical pretreatment, where the ^{210}Po fraction was corrected according to 7.9. Table 8.12 shows both, the measured isotope ratio and the corrected isotope ratio. Figure 8.15 on

the other hand plots the isotope ratio without correction according to 7.9. The corresponding fluence of these samples are listed in chapter 5.2.

Sample@Cat	$^{210m}\text{Bi}/^{209}\text{Bi}$ ($\cdot 10^{-12}$)	^{210}Po Cor.	$^{210m}\text{Bi}/^{209}\text{Bi}$ Cor ($\cdot 10^{-12}$)
FZKA@6	1.3 ± 0.5	53 %	0.6 ± 0.2
FZKA@30	1.3 ± 0.5	53 %	0.6 ± 0.2
FZKA3@2	0.9 ± 0.6	53 %	0.4 ± 0.3
FZKA_GW@4	2.8 ± 1.0	0	
FZKA_GW@24	2.7 ± 1.0	0	
FZKB_GW@14	0.9 ± 0.6	0	
FZKB_GW@19	3.0 ± 1.2	0	
FZKB@11	2.0 ± 0.4	59 %	0.8 ± 0.2
FZKB@34	1.5 ± 0.4	59 %	0.6 ± 0.2
FZKB@39	1.3 ± 0.3	59 %	0.5 ± 0.1
FZKB@1	1.3 ± 1.6	59 %	0.5 ± 0.7

Table 8.12: $^{210m}\text{Bi}/^{209}\text{Bi}$ isotope ratio for samples irradiated with neutrons ($kT=25$ keV) at Forschungszentrum Karlsruhe. Samples denoted with “GW” where chemically treated before the AMS measurement. For the other samples the ^{210}Po fraction was corrected using a polonium scale factor of 15.

Surprisingly samples with chemical “removal” of ^{210}Po give a higher isotope ratio. This was not expected as ^{210}Po has a higher negative ion formation probability compared to bismuth. A possible contamination during the chemical treatment might be the reason.

Applying a polonium correction for the samples without pretreatment, as shown in table 8.12, the isotope ratio of $^{210m}\text{Bi}/^{209}\text{Bi}$ is still significantly above the value of blank samples.

These results show that cross-section measurements for $^{209}\text{Bi}(n, \gamma)^{210m}\text{Bi}$ in the resonance region are possible with AMS at VERA but accuracy and reproducibility have to be improved.

9 Summary and outlook

For this thesis 24 bismuth samples were irradiated with thermal neutrons ($kT \approx 25$ meV) at the Atominstitut Vienna (see chapter 5). The neutron fluence was determined with fluence monitors, made of gold or zirconium. The uncertainty of the fluence determination of $\pm 5\%$ for the first neutron irradiations could be reduced by using two or more fluence monitors for each bismuth sample to $\pm 3\%$. As the neutron flux depends strongly on the position, the accuracy has been improved further by irradiating bismuth pellets. The preferred fluence monitor material would be gold, as the accuracy of the neutron-capture cross-section of ^{197}Au is better known than of ^{94}Zr . Due to the high activity of gold monitors, the measurements of the fluence monitors, were carried out directly at the Atominstitut.

The thermal cross-section value of $^{209}\text{Bi}(n,\gamma)^{210\text{g}}\text{Bi}$ was determined via activity measurement and gave a value of (16.9 ± 1.0) mbarn. This value agrees with the measurement of Letourneau et al. (18.4 ± 0.9) mbarn [17] and is somewhat smaller than the cross-section measured by Borella et al. (19.3 ± 0.8) mbarn [13] - see chapter 1.1.

Furthermore, the negative ion formation probability of ^{209}Bi and of ^{210}Po was measured. To confirm the measured value of $1 \cdot 10^{-3}$ for the negative ion formation probability of ^{209}Bi (see chapter 8.2.1), the sputter test should be repeated with bismuth samples of about 10-15 mg - the typical amount of bismuth AMS samples. Beam losses between the position where $^{209}\text{Bi}^{5+}$ currents were measured and where $^{210\text{m}}\text{Bi}$ events were counted are hard to determine. Therefore, it was not possible to check the negative ion formation probability with an independent measurement, e.g. the measured allover efficiency of polonium. By measuring bismuth samples that contained a high ^{210}Po fraction and using the measured cross-section value for the $^{209}\text{Bi}(n,\gamma)^{210\text{g}}\text{Bi}$ reaction, it was estimated that polonium yields negative ions by caesium sputtering by about a factor of 15 more effectively than bismuth (see chapter 8.2.3). This work describes the first $^{210(\text{g+m})}\text{Bi}$ measurements at VERA. The detection limit for the

9 Summary and outlook

$^{210\text{m}}\text{Bi}/^{209}\text{Bi}$ isotope ratio at VERA was determined as $(1-4)\cdot 10^{-12}$ (see chapter 7.3). This is a vast improvement over the detection limit obtained by the team of the Maier-Leibnitz laboratory at Munich ($5\cdot 10^{-9}$ [4]).

Bismuth samples irradiated at Forschungszentrum Karlsruhe with a quasi-Maxwellian energy distribution of 25 keV were also analysed with AMS at VERA. The measured isotope ratios are clearly above the detection limit of VERA (see chapter 8.6). Therefore, it is possible to measure the cross-section of $^{209}\text{Bi}(n,\gamma)^{210\text{m}}\text{Bi}$ in the resonance region in principle, but the results vary up to a factor of three. Clearly, the reproducibility of the measured $^{210\text{m}}\text{Bi}/^{209}\text{Bi}$ isotope ratio has to be improved. It has to be stressed that this are the first $^{210\text{m}}\text{Bi}$ AMS measurements for the resonance region.

Reproducibility is the challenge for coming $^{210\text{m}}\text{Bi}$ AMS measurements. It turned out that the scatter of measured $^{210\text{m}}\text{Bi}/^{209}\text{Bi}$ isotope ratios for ^{210}Po -free samples is much smaller compared to samples containing ^{210}Po . It seems that either ^{210}Po or the mixture of ^{210}Po and ^{210}Bi causes poor reproducibility. It is possible to separate ^{210}Po (the isobar of $^{210\text{m}}\text{Bi}$) chemically prior to the AMS measurement (see chapter 7.5.2). As the first neutron irradiation of bismuth samples took place three years ago, it is also possible to measure chemically untreated bismuth samples with AMS and to correct for the still existing ^{210}Po fraction (see chapter 7.5.1).

The determination of the transmission between $^{209}\text{Bi}^{5+}$ current measurement and $^{210\text{m}}\text{Bi}$ event counting via the known cross-section of $^{209}\text{Bi}(n,\gamma)^{210(\text{g}+\text{m})}\text{Bi}$ showed high uncertainty, likely, due to the growing ^{210}Po content in the used samples. The method could be slightly improved by expanding the area of accepted events in the TOF-energy plot. But this affected the detection limit, as more particles with $A=209$, injected as $^{209}\text{BiH}^-$, cause a higher background. Due to the high uncertainty caused by this method, other possibilities to measure the efficiency should be explored, e.g. to measure the isobar ^{210}Pb ($t_{1/2} = 22.3$ years) relative to stable ^{208}Pb .

Bibliography

- [1] Pierre de Marcillac, Noël Coron, Gérard Dambier, Jacques Leblanc, and Jean-Pierre Moalic. Experimental detection of alpha-particles from the radioactive decay of natural bismuth. *Nature*, 422:876–878, 2003.
- [2] E. Browne. Nuclear data sheets for $A = 210$. *Nuclear Data Sheets*, 99:649–752, 2003.
- [3] E. Browne. Nuclear data sheets for $A = 206$. *Nuclear Data Sheets*, 88:29–154, 1999.
- [4] C. Stan-Sion, A. Letourneau, H. Reithmeier, V. Lazarev, M. Enachescu, and E. Nolte. AMS measurement of the neutron capture cross-section $^{209}\text{Bi}(n,\gamma)^{210\text{m}}\text{Bi}$. *Nuclear Instruments and Methods in Physics Research B*, 259:739–744, 2007.
- [5] M.B. Chadwick, P. Obložinský, M. Herman, et al. ENDF/B-VII.0: Next generation evaluated nuclear data library for nuclear science and technology. *Nuclear Data Sheets*, 107:2931–3118, December 2006.
- [6] J.I. Hoover, W.H. Jordan, C.D Moak, L. Pardue, H. Pomerance, J.D. Strong, and E.O. Wollan. Measurement of Neutron Absorption Cross Sections with a Pile Oscillator. *Physical Review*, 74:864–870, July 1948.
- [7] K. Shibata et al. Japanese evaluated nuclear data library version 3 revision-3: JENDL-3.3. *Journal of Nuclear Science and Technology*, 39:1125–1136, 2002.
- [8] S.P. Harris, C.O. Muehlhause, and G.E. Thomas. Low energy neutron resonance scattering and absorption. *Physical Review*, 80:342, 1950.
- [9] D.J. Littler and E.E. Lockett. The pile neutron absorption cross sections of bismuth. *Proc. Phys. Soc. (London)*, A66:700, 1953.

- [10] G.W. Horsley. The preparation of bismuth for use in a liquid-metal fuelled reactor. *Journal of Nuclear Energy*, 6:41–52, 1957.
- [11] R. B. Tattersall, H. Rose, S. K. Pattenden, and D. Jowitt. Pile oscillator measurements of resonance absorption integrals. *Journal of Nuclear Energy. Part A. Reactor Science*, A12:32, 1960.
- [12] A. Letourneau, A. Berthoumieux, O. Deruelle, M. Fadil, G. Fioni, H. Fuaust, P. Mutti, G. Simpson, and P. Schillebeeckx. Thermal neutron capture branching ratio of ^{209}Bi using a gamma-ray technique. In J. Kvasil, P. Cejnar, and M. Krlicka, editors, *11th Intern. Symp. on Capture Gamma-ray Spectroscopy and Related Topics*, pages 734–737, 2002.
- [13] A. Borella, A. Moens, P. Schillebeeckx, R. Van Bijlen, G. L. Molnár, T. Belgya, Zs. Révay, and L. Szentmiklósi. Determination of the $^{209}\text{Bi}(n,\gamma)$ capture cross section at a cold neutron beam. *J. Radioanal. Nucl. Chem.*, 265:267–271, 2005.
- [14] Leo Seren, Herbert N. Friedlander, and Solomon H. Turkel. Thermal neutron activation cross sections. *Phys. Rev.*, 72(10):888–901, Nov 1947.
- [15] F. C. W. Colmer and D. J. Littler. Pile Neutron Absorption Cross Sections of some of the Elements. *Proc. Phys. Soc. (London)*, A63, 1950.
- [16] Makoto Takiue and Hiroaki Ishikawa. Thermal neutron reaction cross section measurements for fourteen nuclides with a liquid scintillation spectrometer. *Nuclear Instruments and Methods in Physics Research*, 148:157–161, 1978.
- [17] A. Letourneau, G. Fioni, F. Marie, D. Ridikas, and P. Mutti. Measurement of the ^{210}Po production induced by thermal neutron capture on ^{209}Bi . *Ann. Nucl. Energy*, 33:377–384, 2006.
- [18] C. Domingo-Pardo et al. New measurement of neutron capture resonances in ^{209}Bi . *Physical Review C*, 74:025807, 2006.
- [19] P. Mutti et al. S-process implications of ^{207}Pb and ^{209}Bi neutron capture cross sections. In N. Prantzos and S. Harissopulos, editors, *Nuclei in the Cosmos*, pages 204–207, 1998.

-
- [20] H. Beer, F. Voss, and R. Winters. On the calculation of Maxwellian-averaged capture cross sections. *The Astrophysical Journal Supplement Series*, 80:403, 1992.
- [21] K. Saito, M. Igashira, J. Kawakami, T. Ohsaki, Toru Obara, and Hiroshi Sekimoto. Measurement of keV-neutron capture cross sections and capture gamma-ray spectra. *Journal of Nuclear Science and Technology*, 41:406–412, 2004.
- [22] S. Bisterzo, F. Käppeler, R. Gallino, M. Heil, C. Domingo-Pardo, C. Vockenhuber, and A. Wallner. Measurement of the $^{209}\text{Bi}(n,\gamma)^{210\text{g}}\text{Bi}$ cross section and updated s-process analysis of the Pb/Bi region. In O. Bersillon, F. Gunsing, E. Bauge, R. Jacqmin, and S. Leray, editors, *International Conference on Nuclear Data for Science and Technology*, page 352, 2007.
- [23] U. Ratzel, C. Arlandini, F. Käppeler, A. Couture, M. Wiescher, R. Reifarth, R. Gallino, A. Mengoni, and C. Travaglio. Nucleosynthesis at the termination point of the s process. *Phys. Rev. C*, 70:065803, 2004.
- [24] E. M. Burbidge, G.R Burbidge, W. A. Fowler, and F. Hoyle. Synthesis of the Elements in Stars. *Reviews of Modern Physics*, 29:547–650, 1957.
- [25] George Wallerstein et al. Synthesis of the elements in stars: forty years of progress. *Review of Modern Physics*, 69:995–1084, 1997.
- [26] E. Anders and N. Grevesse. Abundances of the elements: Meteoritic and Solar. *Geochimica et Cosmochimica Acta*, 53:197–214, 1989.
- [27] H. Oberhummer. *Kerne und Sterne. Einführung in die Nukleare Astrophysik*. Barth, Leipzig, 1993.
- [28] R. Boyd. *An Introduction to Nuclear Astrophysics*. The University of Chicago Press, Chicago, 2008.
- [29] NEA. Handbook of lead-bismuth eutectic alloy and lead properties, materials compatibility, thermal-hydraulics and technologies. Technical report, OECD/NEA Nuclear Science Committee, 2007.

- [30] W. Gudowski. Transmutation of Isotopes — Ecological and Energy Production Aspects. *Acta Physica Polonica B*, 31:107, 2000.
- [31] N.E. Todreas, P.E. MacDonald, J. Buongiorno, and E.P. Loewen. Medium-power lead alloy reactors: Missions for this reactor technology. *Nuclear Technology*, 147:305, 2004.
- [32] Y. Kadi. Spallation target R&D for the EU Accelerator-Driven Sub-critical System Project. Technical report, European Organization for Nuclear Research, CERN, November 2004.
- [33] H. Abderrahim et al. Myrrha, A Multipurpose Accelerator Driven System for R&D. State-of-the-art at mid-2003. In *International Workshop on P&T and ADS development (ADOPT 2003)*, 2003.
- [34] K. van der Meer et al. Spallation yields of neutrons produced in thick lead/bismuth targets by protons at incident energies of 420 and 590 MeV. *Nuclear Instruments and Methods in Physics Research B*, 217:202–220, 2004.
- [35] H. Abderrahim, P. Kupschus, E. Malambu, Ph. Benoit, K. Van Tichelen, B. Arien, F. Vermeersch, P. Dhondt, Y. Jongen, S. Ternier, and D. Vandeplassche. Myrrha: A multipurpose accelerator driven system for research & development. *Nuclear Instruments and Methods in Physics Research A*, 463:487–494, 2001.
- [36] G.S Bauer. Physics and technology of spallation neutron sources. *Nuclear Instruments and Methods in Physics Research A*, 463:505–543, 2001.
- [37] C. Vockenhuber, M. Bichler, A. Wallner, W. Kutschera, I. Dillmann, and F. Käppeler. Measurement of the thermal neutron capture cross section and the resonance integral of radioactive ^{182}Hf . *Phys. Rev. C*, 77:044608–1, 2008.
- [38] S. Mughabghab. *Atlas of Neutron Resonances: Resonance Parameters and Thermal Cross Sections Z=1-100*. Elsevier, Amsterdam, 2006.
- [39] S. Mughabghab, M. Divadeenam, and N. Holden. Neutron cross sections from neutron resonance parameters and thermal cross sections. webpage <http://isotopes.lbl.gov/ngdata/sig.htm>, 1982.

- [40] R.L. Auble. Nuclear data sheets for $A = 198$. *Nuclear Data Sheets*, 40:301–383, November 1983.
- [41] T. W Burrows. Nuclear data sheets for $A = 95$. *Nuclear Data Sheets*, 68:635–746, 1993.
- [42] A. Artna-Cohen. Nuclear data sheets for $A = 97$. *Nuclear Data Sheets*, 70:85–172, 1993.
- [43] Baglin Coral M. Nuclear data sheets for $A = 93$. *Nuclear Data Sheets*, 70:1–84, September 1993.
- [44] F. De Corte and A. Simonits. Recommended nuclear data for use in the k0 standardization of neutron activation analysis. *Atomic Data and Nuclear Data Tables*, 85:47–67, 2003.
- [45] Anton Wallner. *Study of the $^{27}\text{Al}(n,2n)^{26}\text{Al}$ Reaction via Accelerator Mass Spectrometry*. PhD thesis, Universität Wien, 2000.
- [46] W. Ratynski and F. Käppeler. Neutron capture cross section of Au197: A standard for stellar nucleosynthesis. *Phys. Rev. C*, 37:595–604, 1988.
- [47] S. Bisterzo. private communication, 2007.
- [48] W. Kutschera. Accelerator mass spectrometry: A versatile tool for research. *Nuclear Instruments and Methods in Physics Research B*, 50:252–261, 1990.
- [49] W. Kutschera et al. Vera: A new AMS facility in Vienna. *Nuclear Instruments and Methods in Physics Research B*, 123:47–50, 1997.
- [50] P. Steier, R. Golser, V. Liechtenstein, W. Kutschera, A. Priller, C. Vockenhuber, and A. Wallner. Opportunities and limits of AMS with 3-MV tandem accelerators. *Nuclear Instruments and Methods in Physics Research B*, 240:445–451, 2005.
- [51] Peter Steier, Robin Golser, Walter Kutschera, Alfred Priller, Christof Vockenhuber, and Stephan Winkler. VERA, an AMS facility for “all” isotopes. *Nuclear Instruments and Methods in Physics Research B*, 223-224:67–71, 2004.
- [52] A Wallner, M. Bichler, I. Dillmann, R. Golser, F. Käppeler, W. Kutschera, M. Paul, A. Priller, P. Steier, and C. Vockenhuber. AMS measurements of ^{41}Ca and ^{55}Fe at VERA - two radionuclides of astrophysical interest. *Nuclear Instruments and Methods in Physics Research B*, 259:677–682, 2007.

- [53] P. Milota, I. Reiche, A. Duval, O. Forstner, H. Guicharnaud, W. Kutschera, S. Merchel, A. Priller, M. Schreiner, P. Steier, E. Thobois, A. Wallner, B. Wünschek, and R. Golser. PIXE measurements of renaissance silverpoint drawings at VERA. *Nuclear Instruments and Methods in Physics Research B*, 266:2279–2285, 2008.
- [54] Peter Steier. *Exploring the limits of VERA: A universal facility for accelerator mass spectrometry*. PhD thesis, Universität Wien, 2000.
- [55] Christof Vockenhuber, Irshad Ahmad, Robin Golser, Walter Kutschera, Vitaly Liechtenstein, Alfred Priller, Peter Steier, and Stephan Winkler. Accelerator mass spectrometry of heavy long-lived radionuclides. *Int. J. Mass Spectrom.*, 223-224:713–732, 2003.
- [56] G. Wallner. private communication, 2009.

Danksagung

Zum Abschluss möchte ich Prof. Robin Golser und Prof. Walter Kutschera dafür danken, dass sie mir die Möglichkeit gegeben haben diese interessante Diplomarbeit bei VERA, am Institut für Kern- und Isotopenforschung zu schreiben.

Dr. Anton Wallner danke ich für die geduldige Betreuung und dafür, dass er sich immer Zeit nahm meine Fragen zu beantworten.

Im weiteren danke ich:

Allen VERA Mitarbeitern für die Unterstützung bei den unterschiedlichsten Problemen.

Prof. Gabriele Wallner für die chemische Vorbehandlung der Wismut Proben.

Prof. Max Bichler und Dr. Georg Steinhauser für die vielen Neutronenbestrahlungen am Atominstytut Wien.

Petra und Irmi für das Korrekturlesen.

Meiner Familie für ihre einzigartige Unterstützung in jeglicher Hinsicht.

Besonders danken möchte ich meiner Freundin Barbara für ihre Geduld und Hilfe bei dieser Arbeit.

Curriculum vitae

Name: Peter Kueß

Date of birth: September 8th, 1982

Place of birth: Klagenfurt

Nationality: Austria

1993-1997: Bundesrealgymnasium, Klagenfurt

1997-2002: HTBLVA Villach f. EDV und Organisation

October 2002 - September 2003: Alternative civilian service: Rotes Kreuz Klagenfurt

since October 2003: Diploma study of *physics* at the University of Vienna

since October 2007: Diploma thesis at VERA, Isotopic Research, Faculty of Physics, University of Vienna (supervisor: Robin Golser, Anton Wallner):

“Exploring AMS for the measurement of the (n,γ) cross-section on ²⁰⁹Bi at energies relevant for nuclear astrophysics and nuclear technology”

Lebenslauf

Name: Peter Kueß

Geburtsdatum: 8. September 1982

Geburtsort: Klagenfurt

Nationalität: Austria

1993-1997: Bundesrealgymnasium, Klagenfurt

1997-2002: HTBLVA Villach f. EDV und Organisation

Oktober 2002 - September 2003: Zivildienst: Rotes Kreuz Klagenfurt

seit Oktober 2003: Studium Physik Diplom an der Universität Wien

seit Oktober 2007: Diplomarbeit bei VERA, Isotopenforschung, Fakultät für Physik, Universität Wien (Betreuer: Robin Golser, Anton Wallner):

“Exploring AMS for the measurement of the (n,γ) cross-section on ^{209}Bi at energies relevant for nuclear astrophysics and nuclear technology”